UNIVERSIDAD COMPLUTENSE DE MADRID
FACULTAD DE CIENCIAS FÍSICAS

TESIS DOCTORAL

Plastic deformation of tungsten under fusion-plasma exposure conditions
Plastische vervorming van wolfraam onder blootstelling aan een fusie-plasma-omgeving

MEMORIA PARA OPTAR AL GRADO DE DOCTOR

PRESENTADA POR

Andrii Dubinko

Directores

Jean Marie Noterdaeme
Dmitry Terenteyev
Mercedes Hernández Mayoral

Madrid, 2019

Plastic Deformation of Tungsten under Fusion-Plasma Exposure Conditions

Plastische vervorming van wolfraam onder blootstelling aan een fusie-plasma-omgeving

Deformación Plástica de Wolframio bajo Condiciones de Exposición a Plasma de Fusión

Andrii Dubinko

Directores / promoters: Prof. J-M. Noterdaeme, PhD, Dr. D. Terenteyev, PhD, Dr. M. Hernández Mayoral, PhD

Doctoral thesis submitted in order to obtain the academic degrees of Doctor of Engineering Physics (Ghent University) and Doctor Erasmus Mundus en Ciencia e Ingeniería de la Fusión (Universidad Complutense de Madrid)

Department of Applied Physics

Head of Department: Prof. C. Leys, PhD

Faculty of Engineering and Architecture

UNIVERSITEIT GENT

Facultad de Ciencias Físicas

Dean: Prof. María Luisa Lucía Mulas, PhD

Universidad Complutense de Madrid

UNIVERSIDAD COMPLUTENSE MADRID

This research was performed at the research centre:

Dit onderzoek werd uitgevoerd aan het onderzoekscentrum:

Esta investigación se realizó en el centro de investigación:

SCK·CEN
Nuclear Materials Science Institute
Boeretang 200
2400, Mol
Belgium

In collaboration with:

In samenwerking met:

En colaboración con:

CIEMAT
Departamento de Tecnologia
División de Materiales de Interés Energético
Avda. Complutense 40
28040, Madrid
Spain

Universiteit Gent
Faculteit Ingenieurswetenschappen en Architectuur
Toegepaste Fysica
St. Pietersnieuwstraat 41, B4
9000, Ghent
Belgium

Universidad Complutense de Madrid
Facultad de Ciencias Físicas
Plaza Ciencias 1
28040, Madrid
Spain

Doctoral guidance committee:

Dr. Dmitry Terentyev

SCK·CEN

Dr. Mercedes Hernández Mayoral

CIEMAT

Prof. Dr. ir. Jean-Marie Noterdaeme

Ghent University

Prof. Dr. ir. Guido Van Oost

Ghent University

Prof. Dr. José Gonzalez Calbet

Complutense University of Madrid

Table of Contents

List of Acronyms

B

BF	Bright Field (image)

C

CBED	Convergent Beam Electron Diffraction

D

DBTT	Ductile-to-Brittle Transition Temperature
DEMO	Demonstration Power Station
DF	Dark Field (image)
DF_RX	Double Forged Recrystallized
DP	Diffraction Pattern

E

EBSD	Electron Backscatter Diffraction
EDM	Electric Discharge Machine
EELS	Electron Energy Loss Spectroscopy

H

HHF	High Heat Flux

I

ITER	International Thermonuclear Experimental Reactor

J

JET	Joint European Torus

K

K-M	Kossel-Möllenstedt (fringes)

M

MHM	Micro-hardness Measurements

N

NI	Nanoindentation
NRA	Nuclear Reaction Analysis

P

PFC	Plasma Facing Components
PFM	Plasma Facing Materials

S

SCW	Single Crystal W (tungsten)
SEM	Scanning Electron Microscopy
SOL	Scrape-off Layer

T

TBM	Tritium Breeding Blanket
TDS	Thermal Desorption Spectroscopy
TEM	Transmission Electron microscopy

U

UTS	Ultimate Tensile Strength

V

VLM	Visible Light Microscopy
VPS	Vacuum Plasma Sprayed

List of Figures

List of Tables

Acknowledgements

This was a very international PhD project and it would not have been possible without help from my colleagues and friends from different countries and institutions.

First of all, I would like to thank my doctoral guidance committee for giving me the opportunity to perform this project and my promoters at Gent University and FUSION-DC Doctoral College, Prof. Guido Van Oost and Prof. Jean-Marie Noterdaeme, for dealing with administrative matters and their general help and support. I would also like to thank Kathleen Van Oost, Eveline Indemans and Muriel Vervaeke for prompt communication and effective handling of administrative procedures.

I would like to express my deepest gratitude to Dr. Dmitry Terentyev, my mentor at SCK-CEN, for invaluable help and support from day one, fruitful scientific discussions, motivation, encouragement and a lot of patience. I would like to thank Dr. Wouter Van Renterghem for sharing his knowledge and expertise on TEM techniques. I'm grateful to a fellow PhD student Anastasiia Bakaeva for lots of collaboration in SEM, NI and TDS measurements and general help. Among other people at SCK-CEN I am thankful to Boris Minov and Milan Konstantinovic for showing me around LHMA and sharing their knowledge on various topics. Many thanks to Danny Penneman for the help with chemical solutions, to Chao Yin for EBSD measurements, to Roel Vanuytven and Jan Knaeps for mechanical tests. Thanks to Giovanni Bonny, Nicolas Castin, Alexander Bakaev and Petr Grigorev for being great office mates and to Aleksandr Zinovev for the help surviving the rainy Belgium weather.

At CIEMAT I would like to thank my mentor Dr. Mercedes Hernández Mayoral whose help in mastering TEM and general guidance and support I greatly appreciate.

I would like to thank Thomas Morgan and Kiril Bystrov at FOM Institute DIFFER for plasma exposures of the samples, this work would not have been possible without this collaboration. Many thanks to Luxherta Buzi at FZJ for collaboration on SC material studies. At UCL I would like to thank Audrey Favache and Sophie Ryelandt for NI tests and Linsey Lapeire at UGent for EBSD measurements. Also, my gratitude goes to Prof. Evgeny Zhurkin from SPbPU for help with work on publications and conference presentations.

Finally, I want to thank all the wonderful people that made my time in Belgium so much more enjoyable, comfortable and home-like.

This work was supported by the European Commission and carried out within the framework of the Erasmus Mundus International Doctoral College in Fusion Science and Engineering (FUSION-DC).

Mol, October 2018

Andrii Dubinko

List of Publications

Publications on this topic:

1. **A. Dubinko**, D. Terentyev, A. Bakaeva, et al. "Sub-surface microstructure of single and polycrystalline tungsten after high flux plasma exposure studied by TEM", Applied Surface Science, Volume 393, Pages 330–339
2. **A. Dubinko**, A. Bakaeva, M. Hernández-Mayoral, et al. "Microstructural modifications in tungsten induced by high flux plasma exposure: TEM examination", Physica Scripta, Volume 2016, Number T167
3. **A. Dubinko**, D. Terentyev, A. Bakaeva, et al. "Effect of high flux plasma exposure on the micro-structural and -mechanical properties of ITER specification tungsten", Nuclear Instruments and Methods in Physics Research Section B: Beam Interactions with Materials and Atoms, Volume 393, Pages 155-159
4. **A. Dubinko**, D. Terentyev, et al. "Evolution of plastic deformation in heavily deformed and recrystallized tungsten of ITER specification studied by TEM", International Journal of Refractory Metals and Hard Materials, Volume 66, Pages 105–115
5. D. Terentyev, G. De Temmerman, B. Minov, Y. Zayachuk, K. Lambrinou, T.W. Morgan, **A. Dubinko**, K. Bystrov and G. Van Oost. "Synergy of plastic deformation and gas retention in tungsten", Nuclear Fusion, Volume 55, Number 1, 013007
6. D. Terentyev, G. De Temmerman, T.W. Morgan, Y. Zayachuk, K. Lambrinou, B. Minov, **A. Dubinko**, K. Bystrov and G. Van Oost. "Effect of plastic deformation on deuterium retention and release in tungsten", Journal of Applied Physics 117, 083302 (2015)
7. D. Terentyev, X. Xiao, **A. Dubinko**, et al. "Dislocation-mediated strain hardening in tungsten: Thermo-mechanical plasticity theory and experimental validation", Journal of the Mechanics and Physics of Solids, Volume 85, December 2015, Pages 1-15
8. A. Bakaeva, D. Terentyev, **A. Dubinko**. "Impact of plastic deformation on plasma induced damage and deuterium retention in tungsten", MRS Advances, Volume 2, Issue 55, 2017, pp. 3347-3352.
9. A. Zinovev, D. Terentyev, **A. Dubinko**, L. Delannay. "Constitutive law for thermally-activated plasticity of recrystallized tungsten" Journal of Nuclear Materials, Volume 496, 1 December 2017, Pages 325–332

Publications on other topics:

1. D. Terentyev, **A. Dubinko**, V. Dubinko, et al. “Interaction of discrete breathers with primary lattice defects in bcc Fe”, Modelling and Simulation in Materials Science and Engineering, Volume 23, Number 8

Executive summary

Using Nuclear Fusion to produce price-competitive electricity is an important element in the European Research and Development Agenda. The next big step is to create 'first plasma' in ITER – the key facility for development of commercial fusion power. While this fusion test-bed is under construction, a number of technical and scientific challenges remain problems that must be solved to enable the efficient and safe operation of ITER.

Ensuring proper functioning of the divertor is one of those challenges. The field lines of a diverted plasma deflect particles, in particular impurities, in the scrape-off layer (the region from the vessel region up to the magnetic separatrix, which is the boundary of the confined plasma region) towards the divertor, where they are to be neutralized and removed through a pumping system. The divertor exhausts the heat produced by the fusion reactions and enables the removal of helium and other impurities by a pumping system, hence it is a vital component of the whole system.

In the ITER divertor, particle flux densities and energies, as well as surface temperature will vary by several orders of magnitude along the divertor surface, with values in the range 10^{20}-10^{24} $m^{-2}s^{-1}$, 0.1-100 eV and 370-1370 K, respectively. Exposed to such conditions, plasma facing material undergoes erosion and cracking. Because it has many important positive properties, Tungsten is selected as the main candidate for this plasma-facing application in ITER. However, tungsten exhibits essentially limited ductility in a low temperature range (i.e. below 1/6 T_m, T_m is melting point), thus resulting in low fracture toughness and inter-granular failure. This poses certain dangers to the structural integrity of the entire system during operation. The cracking of tungsten under operational conditions originates from the simultaneous application of stresses and modification of microstructure induced by the neutrons, mechanical loads and penetration of plasma components.

By now, it is well established that microstructure and mechanical properties of tungsten play a primary role in its performance as plasma facing material. Delivering the material with the best balanced properties in terms of high strength, good ductility, low susceptibility to the plasma induced cracking and low retention is the purpose of the current R&D programme, which is dedicated to the design of innovative tungsten-based materials. On the one hand, heavy plastic deformation is seen to make a positive impact on the ductility, but on the other hand, the amount of initial defects such as dislocations and grain boundaries has a clear impact on the retention, as the defects trap plasma components. Because of this, it is important to understand and single out the impact of different types of microstructural defects, plastic deformation, and retention in commercial tungsten grades relevant to the ITER specification and

requirements. In this work, commercial products fabricated by Plansee AG are investigated.

This investigation comprises studies of plastic deformation under tensile deformation at temperatures between 300-and 600°C, the critical range for low temperature embrittlement of a water cooled divertor. Microstructural characterization of the material in as-produced, as-annealed/recrystallized and as plasma exposed conditions was performed by means of transmission electron microscopy. Deuterium high flux plasma exposure, replicating ITER divertor conditions, was carried out using the Pilot PSI device at Dutch Institute for Fundamental Energy Research (DIFFER).

This study showed that the plastic deformation mechanisms in the as-produced and as-recrystallized ITER specification tungsten exhibit certain differences. The comparison of the evolution of plastic deformation in as-received and recrystallized samples reveals a significant deviation in the mechanisms mediating the deformation. In recrystallized tungsten, this deformation is controlled by the dislocation multiplication and pile-ups formed next to the high angle grain boundaries, which eventually cause crack initiation and propagation. In the case of as-fabricated forged tungsten with elongated grains and texture, the main deformation mechanism is the dislocation-grain boundary interaction and grain boundary slip. The ability of grain interfaces to slip plays the major role in the ductility of as-produced tungsten. Whereas, the ductility of the recrystallized tungsten is determined by the absorption/dissolution of dislocation pile-ups formed next to high-angle grain boundaries. Despite this difference, several stages of the plastic deformation process were clearly produced in both types of the material as was judged from the evolution of the dislocation density and morphology of dislocation structures, as well as the intensive grain refinement observed at the late stage of the deformation.

Systematic TEM analysis of the surface and sub-surface region of the different tungsten materials exposed to the high flux plasma, which mimics ITER divertor exposure conditions, revealed the occurrence of plastic deformation whose intensity depends on the depth of the inspected region. Plasma exposure induced heavily and strongly localized plastic deformation, which occurred irrespective of the initial microstructure, even in single crystal samples. However, the particular increase of the dislocation density and other regularly observed features depend on the initial microstructure. The TEM-inspected microstructure of the exposed material reverts to the one observed in bulk at a depth of about 12-20 μm. The observed heavy plastic deformation in the sub-surface region apparently has a strong impact on the sub-surface retention of plasma components. This, as well as the internal stresses seen, could be responsible for eventual crack initiation. The sequence of physical processes which occur under the action of the high flux plasma attack are described and discussed on the evidential basis of the performed TEM observations, as well as describing the experimental

measurements done on the studied samples. The final conclusion of this work is that the trapping of high flux plasma components on dislocation network, and the further production of local plastic deformations are mutually-related processes which occur simultaneously during the exposure.

Nederlandse samenvatting

Het gebruik van kernfusie om prijsconcurrentiële elektriciteit te produceren is een belangrijk element in de Europese Onderzoeks- en Ontwikkelingsagenda. De volgende grote stap is het creëren van het eerste plasma in ITER - de belangrijkste faciliteit voor de ontwikkeling van commerciële fusiecentrales. Terwijl deze fusie testreactor in aanbouw is, blijven er een aantal technische en wetenschappelijke uitdagingen, problemen die moeten worden opgelost om de efficiënte en veilige werking van ITER mogelijk te maken.

Het verzekeren van een goede werking van de divertor is een van die uitdagingen. De veldlijnen van een afgeleid plasma leiden de deeltjes om, in het bijzonder onzuiverheden, in de afscheidingslaag (het gebied in het vacuümvat tot aan de magnetische separatrix, die de grens van het afgesloten plasmagebied vormt) naar de divertor, waar ze worden geneutraliseerd en verwijderd via een pompsysteem. De divertor vormt de uitlaat voor de warmte die door de fusie reacties wordt veroorzaakt en maakt het mogelijk om He en andere onzuiverheden te verwijderen door een pompsysteem, waardoor het een vitaal onderdeel vormt van het gehele systeem.

In de ITER-divertor zullen deeltjesfluxdichtheden en -energieën, evenals de oppervlaktetemperatuur, variëren met verschillende grootteordes over het divertoroppervlak, met waarden in het bereik 10^{20}-10^{24} $m^{-2}s^{-1}$, 0.1-100 eV en 370-1370 K respectievelijk. Blootgesteld aan dergelijke omstandigheden, ondergaat het plasma-blootgestelde materiaal erosie en barsten. Omdat het veel belangrijke positieve eigenschappen heeft, is Wolfraam geselecteerd als de belangrijkste kandidaat voor deze plasma-toepassing in ITER. Wolfraam vertoont echter in hoofdzaak beperkte ductiliteit in een laag temperatuurbereik (d.w.z. onder 1/6 T_m, met T_m het smeltpunt), wat resulteert in een lage breuktaaiheid en een intergranulair falen. Dit zorgt voor bepaalde gevaren voor de structurele integriteit van het gehele systeem tijdens de uitbating. Het barsten van wolfraam onder operationele omstandigheden komt voort uit de gelijktijdige toepassing van spanningen en de verandering van de microstructuur geïnduceerd door neutronen, mechanische belasting en penetratie van plasma deeltjes.

Tegenwoordig is het goed geweten dat de microstructuur en mechanische eigenschappen van wolfraam een belangrijke rol spelen in zijn prestatie als plasma gericht materiaal. Het leveren van het materiaal met de meest evenwichtige eigenschappen aangaande hoge sterkte, goede ductiliteit, lage gevoeligheid voor de plasma-geïnduceerde barsten en een lage retentie, is het doel van het huidige R & D-programma, dat zich toelegt op het ontwerpen van innovatieve wolfraam gebaseerde materialen. Enerzijds wordt de zware plastische vervorming gezien als een positieve invloed op de ductiliteit, maar anderzijds heeft de hoeveelheid initiële defecten, zoals dislocaties en korrelgrenzen een duidelijke invloed op de retentie, aangezien de

defecten de plasma deeltjes vangen. Hierdoor is het belangrijk om de impact van de verschillende types defecten in de microstructuur, zoals plastische vervorming en retentie in commercieel wolfraam die voldoen aan de ITER-specificaties te isoleren en begrijpen. In dit werk worden commerciële producten vervaardigd door Plansee AG onderzocht.

Dit onderzoek omvat studies van plastische vervorming onder trek bij temperaturen tussen 300°C en 600°C, het kritieke bereik voor de lage temperatuursverbrossing van een watergekoelde divertor. Microstructurele karakterisering van het materiaal in initiële, gerekristalliseerd en aan plasma blootgesteld Wolfraam werd uitgevoerd door middel van transmissie-elektronenmicroscopie. Deuterium hoge flux plasma blootstelling, welke de ITER divertor omstandigheden simuleert, werd uitgevoerd met behulp van het Pilot PSI apparaat bij het Nederlands Instituut voor Fusieonderzoek (DIFFER).

Uit deze studie bleek dat de plastische vervormingsmechanismen in het initiële en gerekristalliseerde ITER-specificatie wolfraam bepaalde verschillen vertoonden. Uit de vergelijking van de evolutie van de plastische vervorming van proefstukken van initiële en gerekristalliseerd wolfraam blijkt een significant verschil betreffende de vervormingsmechanismen. In gerekristalliseerd wolfraam wordt de vervorming veroorzaakt door dislocatievermenigvuldiging en ophopingen die gevormd worden langs de grote-hoek korrelgrenzen, die uiteindelijk breukinitiatie en propagatie veroorzaken. In het geval van het initieel gesmede wolfraam met langwerpige korrels en textuur is het belangrijkste vervormingsmechanisme de dislocatie-korrelgrens interactie en de korrelgrensslip. De mogelijkheid van korrelgrenzen om te glijden speelt een belangrijke rol in de ductiliteit van initieel wolfraam. De ductiliteit van het gerekristalliseerde wolfraam, daarentegen, wordt bepaald door de absorptie en ontbinding van dislocatie ophopingen gevormd naast grote-hoek korrelgrenzen. Ondanks dit verschil werden verschillende fasen van het plastische vervormingsproces duidelijk geobserveerd in beide types materialen, zoals werd afgeleid uit de evolutie van de dislocatie-dichtheid en haar morfologie. De evolutie van de gemeten dislocatiedichtheid toont een afwijking van de klassieke Mecking-Kocks wet aan. Dit wordt toegeschreven aan de korrelverfijning en de vorming van cellulaire structuren bij grote vervormingen, die dienen als kernen van nieuwe kleine-hoek korrelgrenzen.

De systematische TEM analyse van het oppervlak- en sub oppervlak van de verschillende wolfraammaterialen die blootgesteld werden aan het hoge flux plasma, die de omstandigheden van de ITER divertor nabootsen, toonde het ontstaan van plastische vervorming aan. De plasma blootstelling veroorzaakte zware en sterk gelokaliseerde plastische vervorming, die zich voordeed ongeacht de initiële microstructuur, zelfs in pure kristallen. Echter, de specifieke toename van de dislocatie-dichtheid en andere regelmatige waargenomen defecten hangt af van de initiële microstructuur. De TEM-geïnspecteerde microstructuur van het blootgestelde

materiaal is gelijk aan die van het bulk vanaf een diepte van ongeveer 12-20 μm. De waargenomen zware plastische vervorming in het sub oppervlak heeft blijkbaar een sterke invloed op de onderoppervlakte-retentie van plasma-deeltjes. Dit, evenals de interne spanningen kunnen aanleiding geven tot barsten. De sequentie van fysische processen die optreden onder de actie van de hoge-flux plasma-aanval worden beschreven op basis van de van de uitgevoerde TEM observaties en experimentele metingen die op de bestudeerde monsters zijn uitgevoerd. De uiteindelijke conclusie van dit werk is dat het opvangen van hoge-flux plasma deeltjes op het dislocatienetwerk en de verdere productie van lokale plastische vervormingen wederzijds gerelateerde processen zijn die tegelijkertijd tijdens de blootstelling optreden.

Resumen ejecutivo

El concepto del uso de la Fusión Nuclear para producir electricidad a precios competitivos está incluido en la agenda Europea de Investigación y Desarrollo. El próximo gran paso es crear "primer plasma" en ITER – la instalación clave para el desarrollo de potencia de fusión comercial. Mientras este banco de pruebas se encuentra en construcción, aún permanecen un cierto número de desafíos científicos y técnicos, así como problemas que deben ser resueltos para hacer posible el funcionamiento eficiente y seguro de ITER.

Uno de estos desafíos es asegurar el funcionamiento apropiado del Divertor. El Divertor se utiliza para deflectar las partículas del plasma desde la región de la vasija hacia el núcleo del plasma, denominada capa de "scrape-off", para neutralizar las partículas y eliminarlas mediante un sistema de bombeo. El Divertor extrae el calor producido por las reacciones de fusión y permite la eliminación del helio y otras impurezas mediante el sistema de bombeo, por lo tanto, es un componente fundamental de todo el sistema.

En el Divertor del ITER, las densidades de flujo de partículas y energías, así como la temperatura de la superficie, variarán en varios órdenes de magnitud a lo largo de la superficie del Divertor, con valores en el rango 1020-1024 m-2s-1, 0.1-100 eV y 370-1370 K, respectivamente. Expuestos a tales condiciones, los materiales en contacto con el plasma sufren erosión y agrietamiento. Debido a sus múltiples e importantes propiedades favorables, el wolframio se ha seleccionado como el principal candidato para revestimiento frente al plasma en ITER. Sin embargo, el wolframio presenta una ductilidad limitada en el rango de bajas temperaturas (es decir, por debajo de 1/6 Tm, siendo Tm el punto de fusión) dando lugar a una baja tenacidad de fractura y fallo intergranular. Esto plantea ciertos peligros para la integridad estructural de todo el sistema durante el funcionamiento. El agrietamiento del wolframio en condiciones de operación procede de la aplicación simultánea de tensiones y de la modificación de la microestructura inducida por los neutrones, cargas mecánicas y penetración de los componentes del plasma.

Actualmente, está bien establecido que la microestructura y las propiedades mecánicas del wolframio juegan un papel fundamental como material frente al plasma. El objetivo del programa de I+D en curso, dedicado al diseño de materiales innovadores basados en el wolframio, es proporcionar un material con propiedades mejores y equilibradas en lo que se refiere a resistencia, buena ductilidad, baja susceptibilidad al agrietamiento inducido por el plasma y baja retención de elementos. Por una parte, la alta deformación plástica se considera que tiene un impacto positivo sobre la ductilidad, pero, por otra parte, la cantidad inicial de defectos como las dislocaciones o los bordes de grano tiene un efecto claro sobre la retención, porque los defectos

atrapan a los componentes del plasma. Debido a esto, es importante comprender y aislar la influencia de los diferentes tipos de defectos microestructurales, de la deformación plástica y de la retención de elementos en diferentes grados de wolframio comercial relevantes para las especificaciones y requisitos de ITER. En este trabajo, se investigan productos comerciales fabricados por Plansee AG.

Esta investigación incluye estudios de deformación plástica en ensayos de tracción a temperaturas entre 300 y 600ºC, que es el rango crítico para fragilización a baja temperatura del divertor enfriado por agua. Se ha realizado la caracterización microestructural del material en estado de recepción, recocido y recristalizado y en condiciones de exposición al plasma mediante microscopía electrónica de transmisión (TEM en sus siglas en inglés). La exposición a alto flujo de plasma de deuterio, reproduciendo las condiciones del divertor de ITER, se llevó a cabo utilizando el equipo piloto PSI en el Dutch Institute of Fusion Research (DIFFER).

Como resultado de este estudio se ha revelado que los mecanismos de deformación plástica en el wolframio de la especificación de ITER en estado de recepción y recristalizado presentan ciertas diferencias. La comparación de la evolución de la deformación plástica apunta al hecho de que una desviación significativa de los mecanismos que intervienen en la deformación se hace patente después de la recristalización. En el wolframio recristalizado, esta deformación está controlada por la multiplicación de dislocaciones y apilamientos formados cerca de las fronteras de grano de alto ángulo, lo cual, eventualmente causa iniciación y propagación de la grieta.

En el caso de wolframio en estado de recepción y forjado, con granos alargados y textura, el principal mecanismo de deformación es la interacción dislocación-frontera de grano y deslizamiento de frontera de grano. La capacidad de las intercaras del grano para deslizamiento juega el papel principal en la ductilidad del wolframio en estado de recepción. Mientras que la ductilidad del wolframio recristalizado está determinado por la absorción/disolución de los apilamientos de dislocaciones formados cerca de las fronteras de grano de alto ángulo. A pesar de esta diferencia, hay diferentes estadios de los procesos de deformación que se producen claramente en los dos tipos de material como se ha juzgado a partir de la evolución de la densidad de dislocaciones y su morfología. La evolución de la densidad de dislocaciones medida demuestra una desviación de la ley clásica de Mecking-Kocks. Este hecho se atribuye al refinamiento del grano y al hecho de que para grandes deformaciones, se produce una formación de estructuras celulares que sirven como núcleo de nuevas intercaras de fronteras de grano de bajo ángulo.

Los análisis sistemáticos de la superficie y de la región sub-superficial, inmediatamente por debajo de la superficie, en diferentes materiales basados en wolframio y expuestos al alto flujo del plasma, que simula las condiciones de exposición del divertor de ITER,

revelan la existencia de deformación plástica. La exposición al plasma induce deformación plástica alta y fuertemente localizada, lo cual tiene lugar independientemente de la microestructura inicial, incluso en muestras monocristalinas. Sin embargo, el particular aumento de la densidad de dislocaciones y otras características observadas regularmente sí dependen de la microestructura inicial. El estado inicial de la microestructura juega un papel significativo sobre el impacto de la exposición al plasma en una capa de 10-15 μm desde la superficie. La microestructura examinada por TEM de los materiales expuestos revierte a la observada propiamente en el material a partir de una profundidad de alrededor de 10-20 μm. La fuerte deformación plástica observada en la región sub-superficial tiene aparentemente, un gran impacto sobre la retención sub-superficial de los componentes del plasma. Esto, así como las tensiones internas observadas, pueden provocar la iniciación del agrietamiento. La secuencia de procesos físicos que ocurren bajo la acción del alto flujo de plasma se describen y discuten sobre la base evidencial obtenida con las observaciones de TEM. Además, se describen las medidas experimentales hechas en las muestras estudiadas. La conclusión final de este trabajo es que el atrapamiento de los componentes del plasma de alto flujo en la red de dislocaciones así como la consiguiente producción de deformaciones plásticas localizadas son procesos mutuamente relacionados que ocurren simultáneamente durante la exposición al plasma.

1. Introduction.

The growing global demand for energy makes the future role of nuclear fusion very significant. Fusion, the reaction that is powering our Sun, occurs between light atoms, such as Hydrogen, and its isotopes, and this coalescence into heavier atoms releases a large amount of energy.

Controlled fusion has already been achieved and currently the most powerful device is JET (Joint European Torus), located in UK. However, the ultimate goal of fusion research is to achieve the conditions and construct a device where the extraction of fusion energy would be durable, stable and commercially justified. One of the key issues to be addressed in the development of a commercial fusion power plant is the selection of materials able to withstand a highly radioactive environment and durable enough to enable profitable exploitation of the device. In particular, the in-vessel materials must survive the severe environment imposed by hot plasma, large heat loads coming in cycles, irradiation with high energy neutrons and, for components exposed to plasma, permeation.

Tungsten and tungsten alloys are being considered as leading candidate materials for functional, structural and armour components in future fusion energy devices. The most attractive properties of tungsten for the design of magnetic and inertial fusion energy reactors are its high melting point, high thermal conductivity, low sputtering yield and low long-term disposal radioactive footprint. Therefore, tungsten is considered to be the material of choice for plasma-facing component in the divertor of ITER and DEMO.

In the ITER divertor, particle flux densities and energies, as well as surface temperature will vary by several orders of magnitude along the divertor surface, with values in the range 10^{20}-10^{24} $m^{-2}s^{-1}$, 0.1-100 eV and 373-1373 K respectively. Exposed to such conditions, tungsten undergoes erosion and cracking. Indeed, due to its high melting point, tungsten exhibits essentially limited ductility in a low temperature range (i.e. below 1/6 T_m, T_m is a melting point). This results in low fracture toughness and inter-granular failure that impose risks to divertor structural integrity during use because of the thermo-mechanical loads. This cracking of tungsten under operational conditions originates from the simultaneous application of stresses and modification of microstructure induced by the neutrons, mechanical loads and penetration of plasma components.

The microstructural response of tungsten to irradiation, heat loads and plasma exposure can be studied directly by means of transmission electron microscopy (TEM), which has an important added value in combination with other fine-scale techniques.

While being very powerful with respect to direct defect identification, this method suffers from one drawback - observation of the material microstructure can only be conducted in a thin area of the sample, limited to 100-200 nm, in the case of tungsten. This implies that characterization of the relatively thick area (from micro-meter to millimeters, as envisaged in the ITER divertor) requires significant efforts in terms of sampling different surface layers and addressing a variety of exposure conditions. Moreover, the in-situ TEM study of the material plasma-exposure, mimicking ITER relevant conditions, is technically impossible (requirement for large magnetic chamber and active coolant to extract the high flux particle heat).

In this work we will attempt to investigate and answer some of the questions arising from the currently available experimental data obtained by different types of experimental techniques, such as thermal desorption spectroscopy (TDS), nuclear reaction analysis (NRA), scanning electron microscopy (SEM) applied to investigate the impact of the high flux plasma exposure on tungsten in the ITER divertor conditions. We perform systematic TEM investigation of the different regions of the material to clarify a number of unresolved questions particularly related to the microstructural evolution in tungsten in the as-received, as-annealed and as-deformed conditions under the high flux plasma exposure. It is planned to quantify TEM-visible defects, such as dislocation lines, networks, tangles, grain boundaries, etc. by their number density, characteristic dimensions and heterogeneity, such that to facilitate the discussion about mechanisms responsible for the trapping of plasma components and surface cracking under prolonged high flux exposure conditions.

1.1 Nuclear Fusion Concept.

Growing demand for energy is one of the major challenges facing our society. Non-renewable sources (like coal, oil, gas) are presently still sufficiently widely available to keep up with the increasing rates of energy consumption, but the greenhouse effect caused by burning fossil fuels contributes significantly to global warming [1-3]. Renewable energies, such as wind and solar are emerging but also have strong limitations such as their intermittency and lack of "on demand" availability. Nuclear fission power is climate friendly and efficient, but produces highly radioactive waste, requiring long term storage and reprocessing [4, 5].

Nuclear fusion promises to be an attractive complimentary source of energy for future demands. It is more efficient than fission (the amount of energy released per gram of fuel is greater), does not produce long-term radioactive waste and offers an attractive concept for the fuel supply.

Indeed, fusion based on coalescence of hydrogen atoms seems to be an almost infinite source of fuel. The energy gain is obtained by fusing two light nuclei into a more stable heavier one. The difference is released in the kinetic energy of the reaction products in agreement with $E = \Delta m c^2$, where Δm is the change in the rest mass of particles.

In this way, for example, synthesis of one ^{4}He nucleus from two deuterium nuclei releases about six times more energy per nucleon than the fission of one ^{235}U nucleus. Note that both nuclear reactions are much more efficient than any chemical reaction, e.g. burning of coal, because of the enormous value of the nucleus binding energy – which is of the order of MeV, compared to eV releasing in typical chemical reactions.

Several types of fusion reactions, typically involving isotopes of hydrogen and ^{3}He, are well known. For the prototype of a commercial fusion reactor, the synthesis of deuterium and tritium is proposed, because among most of the known fusion reactions it has the highest cross-section and requires the lowest temperature to ignite:

$$ {}^{2}_{1}\mathrm{D} + {}^{3}_{1}\mathrm{T} \rightarrow {}^{4}_{2}\mathrm{He}\ (3.5\mathrm{MeV}) + \mathrm{n}^{0}\ (14.1\mathrm{MeV}) \qquad (1.1) $$

The kinetic energy of the neutrons produced in such reactions can then be used to heat the working body (i.e. coolant like water, gas, liquid metal), which through the heat exchanger and steam generator can drive a turbine, exactly as in currently operating conventional power plants, including nuclear ones.

Ensuring a closed fuel cycle and self-sufficiency is extremely important for a long-term and large-scale commercial power plant. As noted above deuterium and tritium are the key fuel elements. Deuterium can be easily extracted from water, but tritium is not available on Earth in sufficient amounts due to its short half-life (12.3 years). Thus, it needs to be obtained directly during the operation of the reactor. The following reaction involving Li (available on Earth in sufficient amount in soil and rocks) is thus proposed:

$$n^0 + {}^6_3\mathrm{Li} \rightarrow {}^3_1\mathrm{T} + {}^4_2\mathrm{He} + 4.78\mathrm{MeV} \quad (1.2)$$

By interacting with the neutrons produced according to the reaction 1.1, the breeding of tritium can become sustainable to enable the closed cycle. That is why part of the first wall behind the shield is called the tritium breeding blanket (TBM) and it is basically the fuel cell of the Fusion Reactor, see schematics in Fig.1.1.

Fusing light atoms requires overcoming the Coulomb barrier, so special conditions have to be fulfilled for the fusion reaction to occur. The positively charged nuclei require an energy corresponding to temperatures of about 100 million degrees, hence the fuel is turned into plasma state. On one hand, the density (temperature) of the plasma must be high enough to ensure sufficient collision frequency (i.e. fusion events), but at the same time must be below the threshold for the Bremsstrahlung radiation emission, which occurs as a result of the interaction of nuclei with electrons. Thus, the optimal conditions for the plasma density must be ensured, and this is most conveniently realized by confinement of the plasma.

The current world-wide efforts are focused on the principle of magnetic confinement. In this approach, the electrically/magnetically conductive hot plasma is confined in a vacuum chamber by the external magnetic field so that the contact of the plasma particles and vacuum vessel is minimized. From 1990 to 2000 a series of studies within

the European fusion programme examined the safety, environmental and economic potential of fusion power (see review in [6]).

Following the earlier analysis of the technological complexity, balance of plant and power exhaust, there are two well-known types of toroidal magnetic confinement devices called tokamaks and stellarators [7], which were selected for the large scale implementation. The main difference between the two is the configuration of the conducting coils. In tokamaks the doughnut shape of the plasma is produced by external toroidal magnets encircling the torus. The plasma is confined due to combination of a toroidal magnetic field and the magnetic field induced by a plasma current, which in turn is induced by changing current in a central solenoid. In a stellarator, the toroidal and poloidal fields needed for confinement are produced by the complex configuration of external magnets, which allow continuous operation of the device, unlike the pulsed operation of a tokamak.

Scientific feasibility of both types of confinements has been demonstrated by the example of both JET [8] and Wendelstein [9] devices. The next step towards the commercial fusion power plant is the construction of ITER (see reviews in [10-12] for the material issues and references therein for other aspects), a tokamak device, which is "one step to" DEMO - a demonstration fusion power plant [11, 13, 14]. The goal of ITER is to produce excess energy, which so far has not been achieved in existing devices and to develop and test key technologies necessary for an effective and safe future power plant. Another important goal is to test different concepts of TBMs, which are needed to enable tritium self-sufficiency for DEMO. Finally, ITER experience is absolutely necessary for the development of the plasma confinement and diagnostics, to ensure that a long pulse, required by the DEMO balance of plant, would become possible.

One of the main challenges to implementation of both ITER and the future DEMO machine is the selection and development (if nature does not offer the material with desired properties) of materials that are able to withstand the fusion environment. Indeed, plasma facing components (PFC) and TBMs will be subjected to high fluxes of energetic particles coming from the burning plasma as well as high thermal, mechanical and electromagnetic loads. In the normal operation mode of ITER, the steady state heat load on the first wall is estimated to be about 0.5 MW/m^2 and up to 10MW/m^2 for the divertor, which is considerably higher than the maximum heat flux experienced by materials in existing fission reactors [15].

To demonstrate the main components and roles played by materials in the fusion reactor, a schematic representation is given in Fig. 1.1, as proposed by Baluc et al.[16]. The plasma is surrounded by the so-called first wall, which consists of metallic tiles (beryllium in ITER, and tungsten in DEMO). Beyond the tiles, acting as armor, the PFCs are located. TBMs are located on the walls, while the divertor is located at the bottom of the reactor. Functional materials are used to diagnose the plasma parameters, such that the confinement parameters could be adjusted on-the-fly. All components will experience thermo-mechanical loads and progressive degradation due to neutron irradiation.

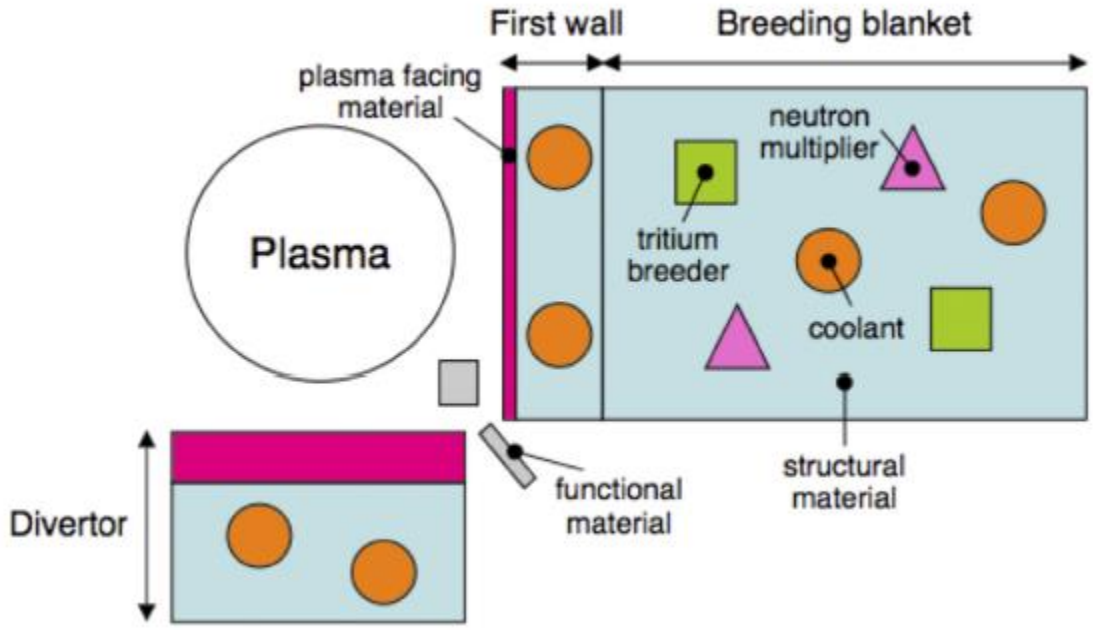

Fig. 1.1. Basics components of the fusion reactor, as schematically proposed by Baluc et. al. [16]

Reliable armor, structural and functional materials are thus critical for the successful operation of the fusion reactor. Integrated in the plasma facing and breeding blanket components, they ensure an effective and safe performance of the reactor. Of the several in-vessel components, the divertor plays a special role.

A poloidal divertor will be installed in the bottom part of the vacuum chamber of the ITER tokamak. Its main function is to extract the power coming from the heat flux in scrape-off layer (SOL) and the plasma radiation, and at the same time to maintain plasma purity by removing the ash and impurities (results of sputtering of the first wall). It must be able to tolerate high heat loads as the main interfacing component between the plasma and material surfaces, while at the same time providing neutron shielding for the vacuum vessel and superconducting magnets. Finally, it will also house the diagnostic systems needed to foster the divertor physics studies and to improve the machine protection level. In both reactors ITER and DEMO, tungsten is selected as the plasma facing material for the divertor component.

1.2 Tungsten as material for divertor.

Tungsten is one of the main materials for the plasma facing components in ITER and DEMO, namely the blanket with the first wall of DEMO and the divertor system in

ITER. The blanket system consists of modules with the first wall and neutron shield mounted on a supporting structure and has three main functions:

- to remove the majority of the fusion power generated by the plasma (during normal ITER operation, the heat fluxes on the first wall will be <1 MW/m² and <5-20 MW/m² in the divertor area). The blanket absorbs the neutrons produced during the reaction and converts their energy into heat, which is removed by the cooling system. The heat from the cooling system will then be transformed into electrical power in a conventional way;
- to reduce the radiation damage in the vacuum vessel structure and superconducting coils;
- to contribute to the passive stabilization of the plasma.

The magnetic geometry of a diverted plasma is used to deflect the plasma particles from the SOL region towards the divertor, where they are neutralized and removed through a pumping system. The divertor also exhausts part of the heat produced by the fusion reactions and removes He and other impurities by a pumping system. This configuration also reduces the amount of impurities going from the first wall to the plasma. The divertor used in ITER consists of 54 cassettes, which are all composed of different PFCs mounted on the cassette body.

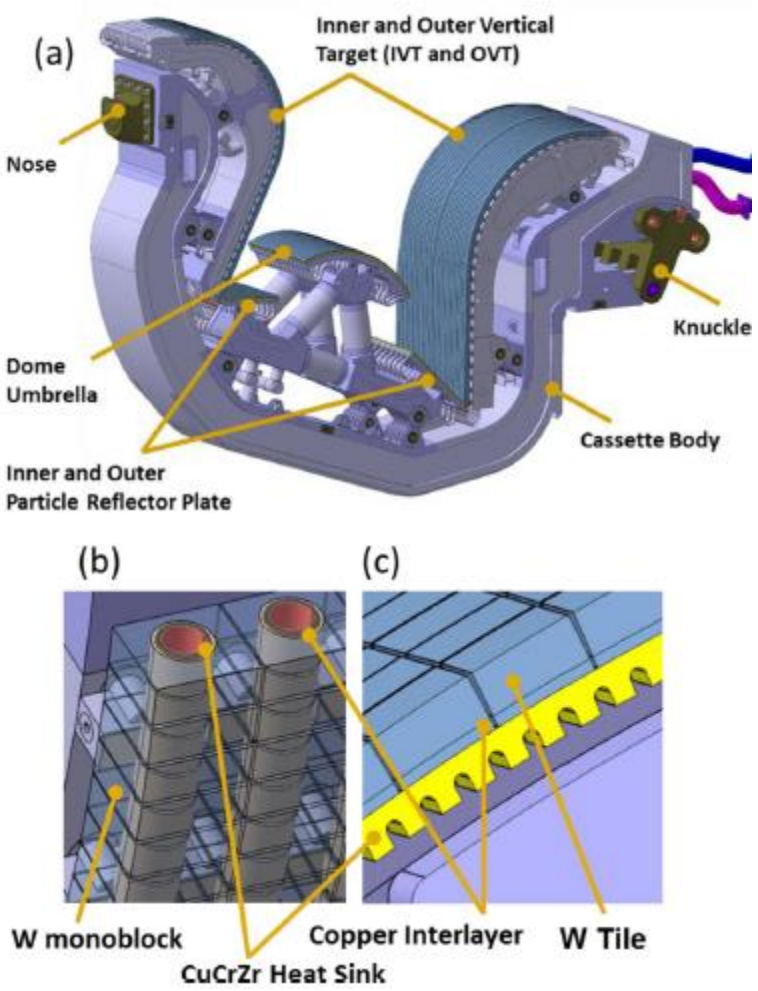

Fig. 1.2. Cross-section of the ITER divertor cassette showing the plasma facing materials and components from [17]. (a) the view of divertor cassette and three main plasma targets (inner, outer and dome). (b) the tungsten mono-block geometry; (c) flat-tile brazed to heat sink material.

Due to the direct contact with the plasma, particle fluxes impinging on the divertor surface are much higher than those on the first wall. The scattering of the particles at the surface of the first wall material results in the heat generation. The resulting heat fluxes on the divertor plasma-facing components are expected to be in the range of 5-20 MW/m^2. Thus, the PFCs must be particularly studied to ensure their resistance to the extreme heat loads. The development of the PFCs represents a major engineering challenge since they also act as shield to protect from neutron irradiation. While neutron irradiation has much deeper penetration range than plasma ion, still a considerable fraction of neutrons will be slowed down in the divertor PFC component. Hence, the correct choice of armour materials for ITER PFCs is one of the important design challenges.

The operational conditions of the plasma facing materials (PFM) are very complex. During normal operation they are subjected to high neutron fluxes, high cyclic heat fluxes, which cause thermal fatigue, and simultaneously to high ion fluxes, which produce erosion. During operation, the PFMs may suffer severe thermal shocks caused by plasma disruptions and by vertical displacement events. One of the most important criteria in the choice of a PFM is its lifetime, which is determined by the rate of degradation of its performance under operation. Therefore the PFMs must have certain physical properties, such as high melting point and low vapor pressure, high mechanical strength and a low erosion rate. They must also exhibit high thermal conductivity, high thermal shock resistance and an acceptable resistance to neutron irradiation. In general, PFMs have to fulfill these special requirements to withstand large energy and particle fluxes without losing thermo-mechanical integrity.

The following main criteria are applied to the selection of PFC material:

a. For compatibility with high flux plasma:

- low erosion rate and sputtering coefficient;

- low vapour pressure;

- low tritium inventory.

b. For structural integrity and thermal transport:

- high thermal conductivity;

- high melting point;

- high fracture toughness;

- high strength (ultimate tensile strength and yield stress);

- resistance to thermal shocks.

c. For radiological aspect and resistance to neutron irradiation:

- low activation and waste;

- low transmutation rate;

- acceptable shift in the ductile to brittle transition temperature due to dpa-damage;

- low void swelling;

- acceptable creep in the upper temperature limit of operation.

d. For commercial applicability:

- availability of material in large amounts (hundreds of tons);

- commercial production route;

- availability of joining technologies (to connect heat sink and PFM).

For the plasma facing material in the divertor, tungsten was selected on the basis of a number of compromises with other potentially attractive materials such as carbon and beryllium [17].

Among negative and positive features of the tungsten, the following ones could be listed as positive:

- high melting point, namely 3422°C;

- low erosion rate (due to high cohesive energy, namely 8.9 eV);

- high thermal conductivity, namely 173 W/(mK) at RT;

- high strength, yield stress is about 600-300 MPa in the temperature range 300-600°C;

- low neutron irradiation swelling, limited to about 1% at 1 dpa.

As for the negative features of tungsten with respect to the first wall material, the following items can be listed:

- high Z number (i.e. only a low concentration of tungsten could be allowed in the plasma to keep its stability);

- formation of volatile oxides (in case of water or air ingress);

- relatively low recrystallization temperature;

- relatively high ductile to brittle transition temperature;

- neutron irradiation embrittlement, i.e. strong increase of ductile to brittle transition temperature already at 1 dpa.

The two latter features may have a strong impact on the structural integrity of tungsten under fusion operation conditions. This is why intensive studies are dedicated to investigate aspects of the high flux plasma-interaction with tungsten, as is addressed in the next section.

1.3 Effect of neutron irradiation in tungsten

As noted above, the operational conditions of the PFM are very complex and one of the critical issue with respect to the performance of the component over the projected exploitation period is the resistance against the impact of neutron irradiation damage.

In general, the neutron damage causes two major effects: (i) collision cascades and subsequent atomic displacement [18]; and (ii) transmutation due to the capture of neutrons, resulting in the formation of He/H gases as well as Re/Os nuclei [19]. The

latter implies that as pure W experience neutron irradiation it actually becomes an alloy containing mainly Re and Os solutes.

The conventional unit used to measure the amount of atomic displacements is called displacement per atom – "dpa" and it corresponds to a fluence of neutrons sufficient to induce the displacement of each atom one time [20, 21]. This does not mean that as soon as the material reaches 1 dpa is "disintegrates". In practice, the recombination of the displaced atoms and their diffusion back to the lattice sites ensures that the ground state lattice structure can be preserved up to very large doses, measured by tens and even hundreds of dpa [22, 23]. However, the particular modification of the microstructure and its impact on the thermo-mechanical properties depends strongly on the irradiation temperature, dose and neutron spectrum.

To get an idea about the neutron fluence and transmutation level expected in ITER and DEMO consider the following data [24]:

- in ITER divertor, at the end of life dose, tungsten PFM will accumulate up to 1 dpa, 0.15% rhenium, and 1 appm of He.
- in DEMO divertor, after five full power years, tungsten PFM will accumulate up to 15 dpa, 3% rhenium, and 30 appm of He.

These figures tell us that at least in the case of ITER, He transmutation and probably Re transmutation should not represent additional degradation of the PFC-relevant properties. In the case of DEMO exploitation conditions, both rhenium and He transmutation should not be neglected.

Below, we shall provide an overview about the main microstructural defects, their evolution depending on the irradiation temperature and dose, as well as their impact on the properties of tungsten relevant for the performance in PFC.

The general effect of high energy neutron irradiation is the so-called collision cascade damage, when neutron "hits" the lattice atom thus causing the cascade-like displacement sequence [25]. The time scale of this process is of the order of pico-seconds and therefore there are no experimental means to observe the process in dynamics. The physics of the collision cascades is therefore studied by molecular dynamics (from early 70th [25, 26] till these days [27, 28]). The computational studies suggest that approximately 70% of the formed lattice defects are being isolated Frenkel pairs (i.e. vacancy and self-interstitial atom), while the rest cluster directly during the cascade phase (i.e. within tens of pico-seconds). These clusters can reach a size of ~1 nm for voids and up to few nano-meters for self-interstitial atom clusters (henceforth called dislocation loops). These defects form so-called primary damage state.

After the primary damage is generated, the cascade annealing begins up the moment when the next cascade is generated in this region. Typical time in between the

cascades, expected for ITER and DEMO conditions, is about micro-second. During this time, the isolated defects and dislocation loops may migrate, while voids may grow or dissolve depending on the ambient temperature [29, 30].

The balance of the generation, diffusion and sink (disappearance) of radiation defects defines the microstructure observed after prolonged irradiation. Given that operational temperature of tungsten in PFC is about to vary from 300 up to 1000°C, the experimental studies were performed in this range focusing on the nano-metric microstructure, thus primary using TEM techniques [31-34].

A schematic diagram reporting the irradiation conditions corresponding to the observation of Dislocation Loops and Voids is given in Fig.1.3, following notation of Hasegawa et al. [33]. Generally, voids are observed at irradiation temperature exceeding 600°C, and at a dose beyond 0.3-0.5 dpa, although the irradiation at 300°C also sometimes generates voids [35]. At temperature below 600°C the microstructure is dominated by the presence of the dislocation loops. Their formation could be observed already at as low dose as 0.1 dpa. The formation of dislocation loops primary leads to the hardening (i.e. increase of the yield stress) and embrittlement [36].

At 800°C, the formation and growth of voids is the most pronounced, and this phenomenon is called void swelling [37, 38]. The formation of voids is detrimental for both: retention of tritium and thermal conductivity.

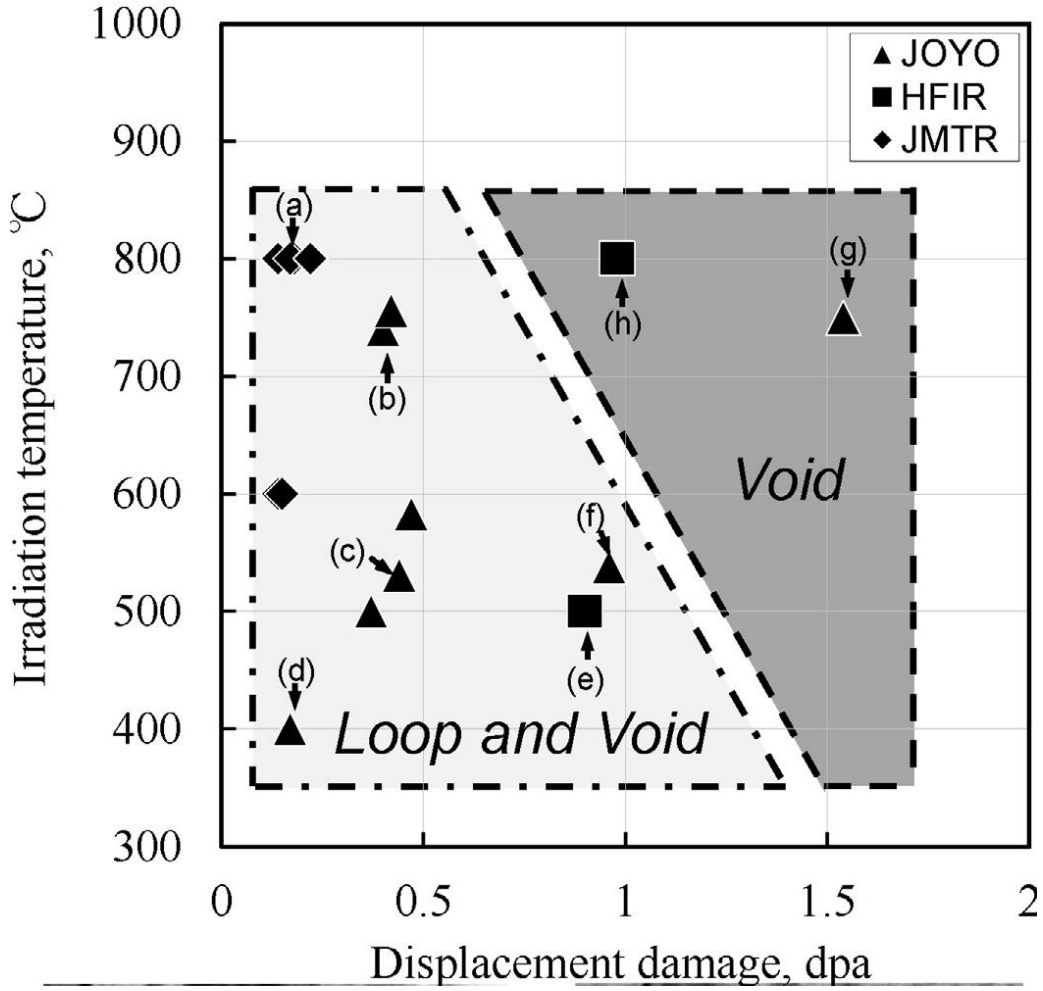

Fig.1.3. Systematic observation of the Loops and Voids, depending on the irradiation dose and irradiation temperature [33]. In original work, (a-c, f) measurements were done by TEM in under-focus conditions; d, g – in over focus conditions; e, h in the focus conditions. The corresponding TEM images can be found in the original works [33, 34, 39]. Joyo, HFIR and MTR stands for acronyms of different material's test reactors.

The transmutation of tungsten into rhenium (and later rhenium into osmium) is another important chain of microstructural modifications caused by neutron irradiation. Although the concentration of Re and Os are not spectacularly high, the availability of mobile irradiation defects (vacancies and self-interstitials) promotes radiation induced diffusion and segregation [40]. As a result, even small amount of the transmuted elements has a strong impact on the evolution of the microstructure. Schematic representation of the evolution of the TEM-visible microstructure in W and We-Re alloys under prolonged neutron irradiation is shown in Fig.1.5, after Hasegawa et al. [41]. In order to understand the overall impact of the transmutation, the irradiation was performed in W-Re alloys with initial concentration of Re up to 26 at.%. The figure shows that as the irradiation dose increases in initially pure W, first

the loops are formed, then voids and after that the presence of needle-like Re/Os precipitates cases the disappearance of the voids. At 30 dpa, the microstructure is primary populated by needle-like precipitates and some voids. Starting the irradiation with some Re in solution leads to the suppression of the loop and void formation, but causes much faster formation of the needle-like precipitates, which dominate the microstructure at 5 dpa already. Further increase of the initial Re content leads to the complete domination of the precipitates in the microstructure already from 0.15 dpa [39]. The main impact associated with the formation of Re precipitates is of course embrittlement [42], as precipitates will act as stress concentrators causing nucleation of cracks in the material under mechanical load.

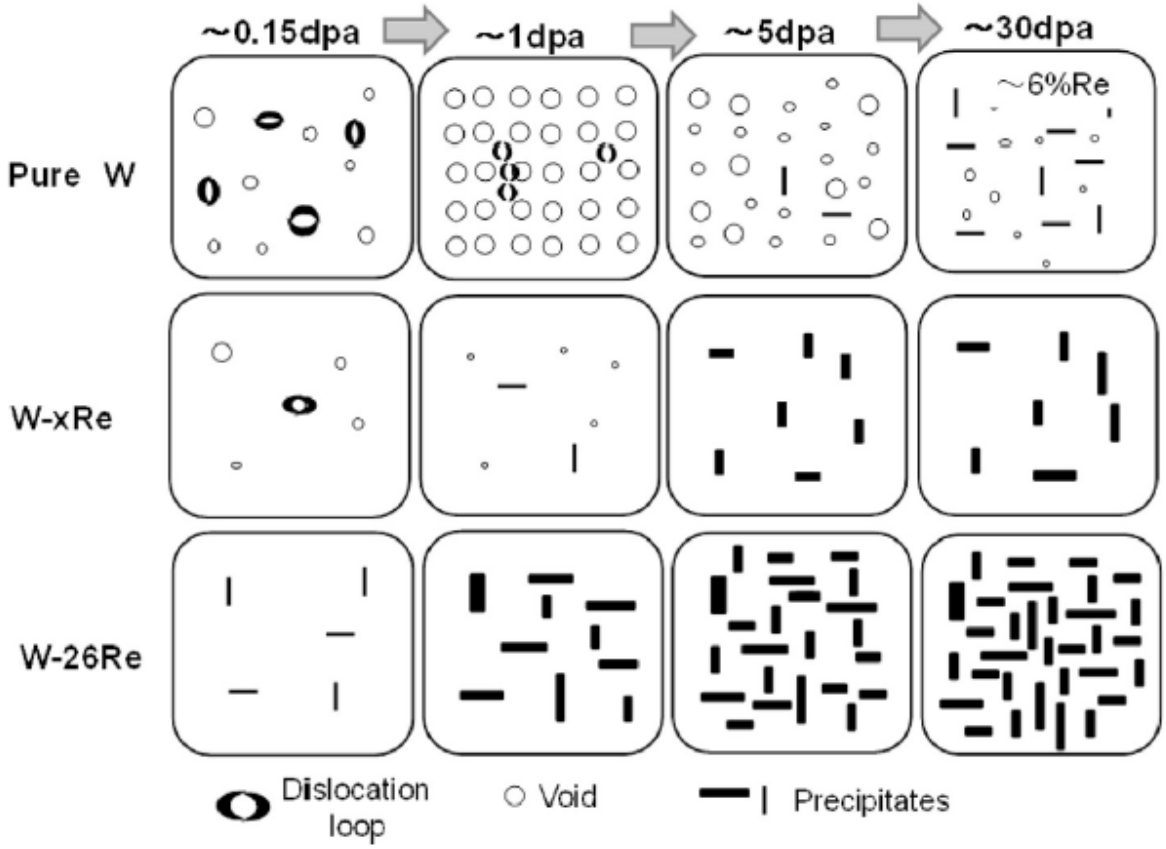

Fig.1.4. Schematic representation of the evolution of the TEM-visible microstructure in W and We-Re alloys under prolonged neutron irradiation [41].

1.4 Thermal shocks and interaction of tungsten with high flux plasma.

As was already mentioned, the PFCs of a fusion device are subjected, among other effects of fusion environment, to transient heat loads, both during the normal

operation (called Edge Localized Modes) and during the off-normal events (such as disruptions and Vertical Displacement Events). This implies that PFMs are subjected to the superposition of steady state and cyclic heat loads, with less frequent transient heat loads. It should be emphasized that the response of the material (although we focus on tungsten, different tungsten grades may experience different response, as will be discussed later) to these conditions is the factor determining the lifetime of the whole component.

Investigation of the material performance under non-stationary heat load conditions is performed by using a combination of devices generating either heat loads or plasma beams, or combinations of both.

Exposure to the ITER/DEMO relevant heat loads results in so called "thermal shock" which is expressed as surface roughening, cracking, and possibly local melting. Importantly, the exposure conditions (base temperature, surface temperature, pulse duration and energy) and initial material microstructure (texture, grain size/dislocation density, chemical composition) have a strong effect on the resulting degradation and cracking.

The mechanisms of surface modification under the transient heat loads can be generally described as follows. At the peak of the heat load (i.e. power load is at its maximum), a steep temperature gradient develops normal to the surface. The length scale of this gradient varies between some microns to several millimeters, depending on the pulse duration, so that essentially only the limited volume close to the surface is affected. This volume experiences volumetric strain (because of natural thermal expansion), giving rise to the compressive stresses in the surface plane.

Depending on the conditions, these stresses can be sufficient to generate irreversible plastic deformation, which during the cooling phase leads to the appearance of tensile stresses. The latter might be high enough to initiate crack formation which would propagate in a direction normal to the surface. In this way, heat cycles lead to a localized thermal expansion and plastic deformation, which establish internal stresses in the material resulting in the crack formation and propagation. An example of a cracking network forming on the surface, and the corresponding sub-surface structure of cracks themselves is presented in Fig. 1.3 by Pintsuk et al [43].

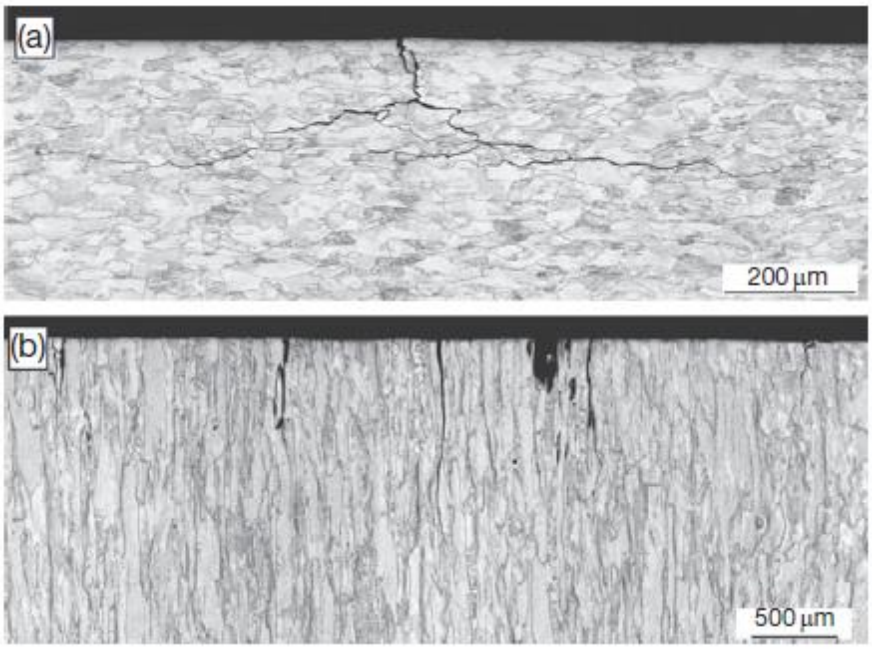

Fig. 1.5. Optical micrograph images of the cross-sections of the sample exposed to thermal shock conditions. Two geometries of the sample are demonstrated, namely the exposed specimen had grains oriented (a) parallel and (b) perpendicular to the loaded surface. Crack paths follow the grain orientation direction [43].

In order to characterize the impact of the heat flux on material, three parameters are used - the damage threshold, the cracking threshold and the melting threshold. While cracking and melting are self-explanatory, damage is characterized by the material's surface undergoing considerable modification, for example roughening or recrystallization. To visualize the impact of loading conditions on the material surface, the diagram as shown in Fig.1.4 is typically used. The X axis represents the base temperature, while Y axis is heat flux value (or power density, or another equivalent) The result of the exposure (presence or absence of microstructural changes, surface damage, cracking or melting) for a given heat flux value at the given base temperature represents a single point on the figure. The convex lines indicate the separation of the regions where the loading conditions generate different types of damage. Example of the parametric space with the defined threshold (i.e. a convex line) is given in Fig. 1.4.

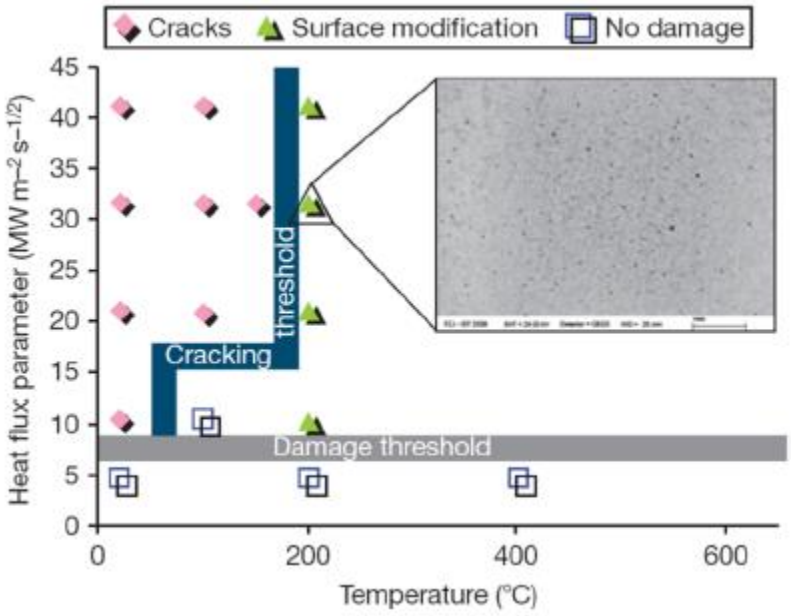

Fig. 1.6. Base temperature - heat flux parameter diagram indicating threshold for cracking and damage [43].

In addition to causing thermal shock under high heat loads, the penetration of plasma components into the sub-surface is also observed. This storage of plasma components is called retention. Under high flux plasma exposure, the particles can penetrate deeply into the material. In this case, the recycling of particles will be determined by the balance of kinetic reflection and permeation into the sub-surface region. The permeated particles will diffuse in the material, such that a fraction of them will again reach the surface, while the rest will remain in the material. The level of this retention is usually expressed as the total amount of particles per unit surface released after the exposure as the result of heat treatment. The natural reason for the storage of gaseous atoms in the metal is the availability of natural defects and impurities which generate so called trapping sites for He and H. The nature of binding between He/H and traps can be of elastic or chemical origin.

The total retention depends on surface temperature of the sample in a non-monotonic way. This is demonstrated in Fig. 1.5 [44]. As the temperature rises from about RT, the retention increases, because the diffusion from sub-surface to bulk is enhanced. At high temperature, the retention is low, because the dissolved gaseous plasma components cannot stand trapping anymore. Subsequently, there is a temperature at which the trapping (and therefore retention) is maximum. This maximum retention temperature is dependent upon the microstructure and purity of the tungsten product. The retention is often observed together with the surface modification, which is expressed in the formation of blisters (see e.g. [45, 46]). It is considered that accumulation of plasma components leads to the formation of bubbles and flakes, which eventually grow into blisters [47, 48]. Also, blistering is known to depend on the

orientation of the grain boundary with respect to the surface. In particular, the grains with <111> orientation are most susceptible to the formation of blisters [45].

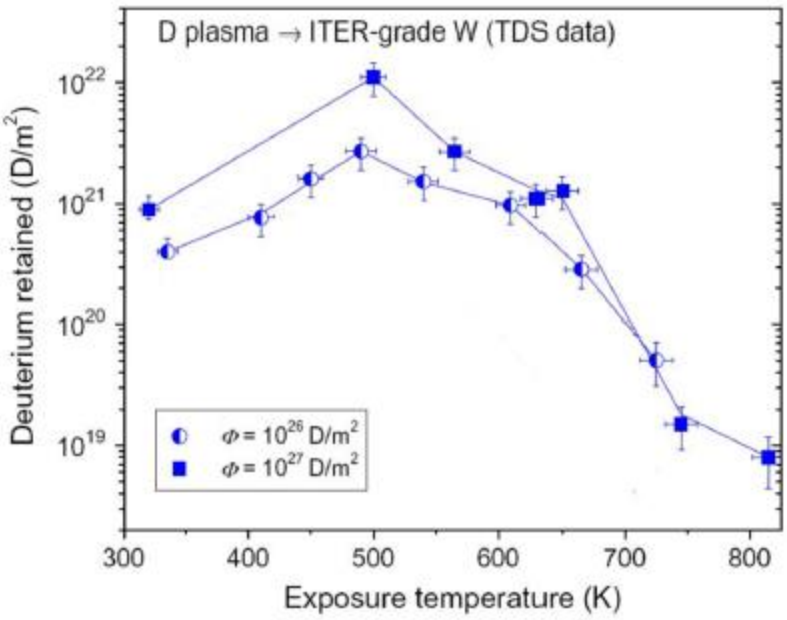

Fig. 1.7. Temperature dependence of retention in tungsten exposed to deuterium plasma [44].

In addition to tungsten microstructure and exposure temperature profile, retention depends on the total fluence and flux. Typically, the total retention grows with the exposure fluence, and in some cases is seen to saturate [49].

The difference in microstructure between tungsten grades implies a variation in the concentration and morphology of intrinsic lattice defects (i. e. defects which do not result from the plasma exposure itself, but exist in the initial state after the manufacturing), which influence the retention. A comparison of retention in different tungsten grades suggests that the retention is enhanced in tungsten coatings such as vacuum plasma sprayed (VPS) films when compared with bulk material. The most unambiguous evidence of the influence of grain boundaries on retention is provided by the comparison of retention in polycrystalline and single-crystal tungsten [50]. Fig. 1.6 depicts the depth dependence of deuterium retained in the two tungsten grades. There is a significant difference in the concentration of retained deuterium at larger depths (beyond 3 μm), most likely to be attributed to the grain boundaries, which trap deuterium and hence increase the retention, especially at high fluences, as compared to the single crystal.

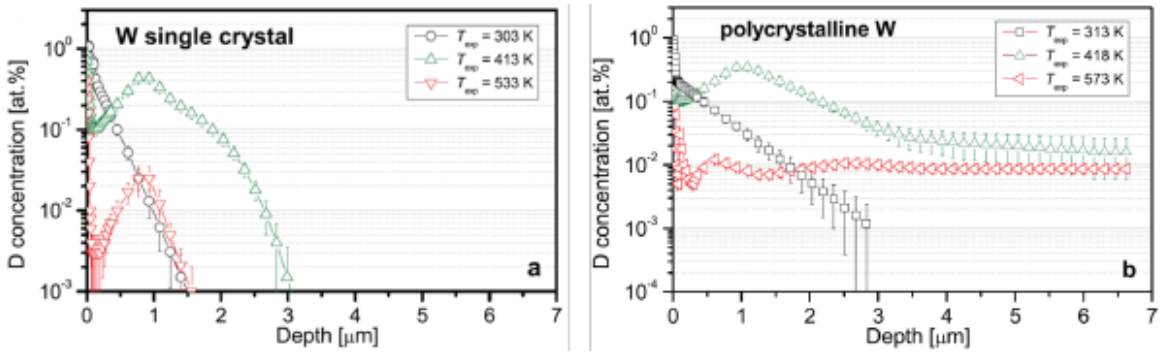

Fig. 1.8. Depth distribution in single crystal and polycrystalline tungsten exposed to deuterium ion beam [50].

The effect of annealing on retention as a result of exposure to low-flux (10^{20} $m^{-2}s^{-1}$) but high fluence ion beam was studied by Ogorodnikova et.al. [51, 52]. Since pre-annealing reduces the amount of natural defects like vacancies and dislocations, the deuterium retention naturally decreases. Annealing not only leads to reduction in total deuterium content, but also leads to modification of the kinetics of the release. The shape of the release spectrum changes such that the high-temperature release peak is eliminated as shown in Fig. 1.7.

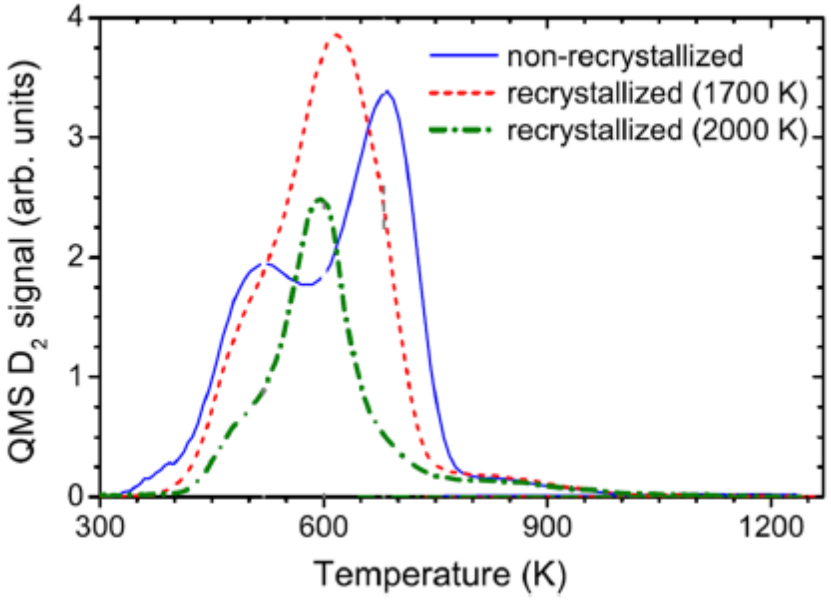

Fig. 1.9. Thermal desorption spectra of the tungsten grade, which experienced different thermal treatment (after fabrication, i.e. in the non-recrystallized state) prior to the plasma exposure. The exposure was performed by D2 ions with energy of 38 eV/D up to a fluence of 6×10^{24} D m^{-2} at 300K. The effect of the recrystallization on the deuterium retention is clearly shown [53].

As has been described above, it is clear that the microstructure and mechanical properties of tungsten play a very important role in such interaction with high flux plasma and material resistance to the high heat loads caused by plasma instability events and during normal operation.

1.5 Mechanical properties and observation of plastic deformation of tungsten by transmission electron microscopy.

The intrinsic mechanical properties of tungsten, as is the case for any other material, can be defined only for high purity single crystals. It is more complicated to describe the mechanical properties of pure polycrystalline tungsten, which is of real technological importance and of commercial relevance, in general: they strongly depend on its purity and thermo-mechanical treatment. The elastic properties of technically pure tungsten are close to purely isotropic material [54]. Single crystal elastic parameters are the following: Young's modulus E=390-410 GPa, shear modulus G=156-177 GPa, bulk modulus K =305-310 GPa, Poisson's ratio = 0.280-0.30. The ductile-to-brittle transition temperature (DBTT) of tungsten, as measured by the four-point bending test is reported to lie in a quite broad range between 450 K and 720 K, naturally depending on the particular grade of the material concerned, as specified above. Naturally, the DBTT cannot be defined as an exact number because it depends on testing conditions as well as on a number of parameters which are not unambiguously defined for a polycrystalline material, such as grain size, texture, dislocation density or impurity content and distribution. However, all reports agree that pure polycrystalline tungsten is brittle at room temperature.

On the other hand, single crystal tungsten was demonstrated to be ductile down to at least 20 K. Brittle cracking occurs due to both inter-granular and trans-granular (so called cleavage) fracture, and ductile to brittle transition occurs in fact in two phases (corresponding to different temperatures), namely: for trans-granular fracture the transition temperature is 300-310 K, while for inter-granular one it is indeed 550-600 K. Recrystallization in tungsten occurs in the temperature range of 1400-1600 K. The brittleness of polycrystalline tungsten, at low temperature, is attributed to the lack of plastic deformation capacity and therefore weakness of the grain boundaries, which leads to the initiation of cracking in both wrought and recrystallized tungsten grades.

Very few reports can be found in the open literature on the direct observation of plastic deformation in tungsten by transmission electron microscopy. A summary of the TEM observations is provided below.

Dislocation microstructure in single crystal tungsten under plastic deformation has been studied by Stephens [55] and Chiem [56]. Stephens investigated the

microstructure of single crystal tungsten (and dilute W-based alloys) in a wide temperature range from 150 K up to 590 K under compressive deformation. This type of deformation is also relevant for the exposure conditions investigated herein.

The study of Stephens [55] showed that above $0.1T_m$ (T_m – melting point), the microstructure is mainly characterized by edge dipoles behind long screw dislocation lines. This type of deformation should be attributed to the glide and cross-slip of screw dislocations which generate edge dipoles in parallel glide planes thus preventing their easy annihilation. Being not capable to cross-slip, the long edge dipoles are therefore observed. Edge type dipoles with a length to width ratio of 10:1 were common at 590 K, compared to ratios of 4:1 and 2:1 at 300 K and 150 K respectively. The presence of edge or screw dislocations and the large length to width ratio at 590 K apparently can be attributed to the difference in their mobility. Indeed, a large difference in the Peierls stress for edge and screw segments imposes different dislocation velocity overall, resulting in the formation of dipoles. In addition, the mobility of dislocations is also sensitive to the internal stress. At low temperature, the applied stress is high, which is why edge dislocations move leaving long screw segments visible.

In the study of Chiem [56] long straight screw dislocations lay parallel to the primary <111> slip direction. Already at 5% of deformation strain, the dislocation tangling and shear dislocation loops were observed. Dislocation junctions lied parallel to <010> direction and were spaced approximately 2 μm apart. These were presumably a_0<100> dislocations formed by the reaction between two $a_0/2$<111> dislocations.

Tabata et al. [57] made in-situ deformation of tungsten single crystal with <100> and <110> tensile axis orientations at room temperature. The multiplication of dislocations clearly attributed to the formation of low/immobile <100> dislocation junctions. Further increase of strain leads to the formation of dislocation networks (groups) and collective movement of those groups resulting in the formation of tangles. Importantly, isolated screw dislocations are noted to contribute to the formation of networks, while networks form tangles. Therefore, the work hardening rate is mainly determined by the movement of dislocation groups arranged in tangles. The slip primarily occurs in {121}<111> system. Cross-slip in {112} planes is also frequently observed.

Wang et al. [58] studied tungsten nano-wires, which were tested by in-situ with high resolution TEM. It is reported that under compressive deformation at room temperature, twins with the structure <111>(112), are formed at about 5% deformation. The resolved shear stress on {112} plane is estimated to be 9 GPa. Importantly, the twinning deformation was also seen to be reversible, i.e. certain release of strain was measured after unloading. Further increase of strain leads to the formation of twin boundary. Hence, under low temperature and high stress conditions, the twinning deformation mechanism is becoming possible.

The above presented review of TEM data, shows that the deformation mechanisms strongly depend on the product fabrication route and thermal treatment. Overall, depending on the product shape, tungsten is delivered in the as-worked state, especially in case of sheet material and wires, or stress-relieved with elongated grains whose interfaces are relaxed (and dislocation density is reduced typically to 10^{13} m^{-2}). The decrease of tensile strength and the increase of the reduction in fracture surface area with increasing test temperature can be related to changes in the fracture mode. Fig.1.8 shows the trend of the variation of the deformation mechanism depending on test temperature, namely: cleavage fracture, grain boundary failure, and ductile fracture [59].

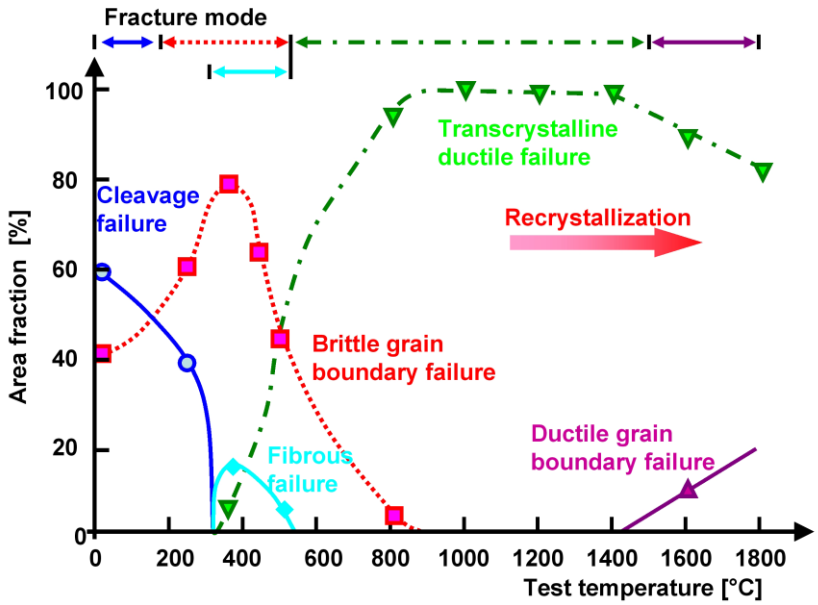

Fig. 1.10. Effect of test temperature on fracture modes of pure tungsten, stress relieved at 1000°C (6 hours) [59].

Indeed, depending on the deformation temperature it is possible to single out three different regimes of the plastic deformation: (I) activation of dislocation motion; (ii) activation of the dislocation-grain boundary absorption/transmission; (iii) grain boundary slip. In Fig.1.8, the domination of the "brittle grain boundary failure" corresponds to the onset of regime I, i.e. dislocations become active, they form pile-ups in front of grain boundaries, where the cracks initiate, coalesce and eventually results in the propagation of the macro-crack [60]. The main factors controlling the formation of pile-ups and density of the dislocations in them are the grain size, grain boundary structure (availability of low or high angle grain boundaries), presence of pores or precipitates inside the matrix [61]. Transmission of the dislocations through the grain boundary primary depends on the mis-orientation angle, the larger the angle – the higher the stress (at the end of the pile-up) needs to be reached. That is why low-

angle grain boundaries do not represent strong obstacles for the dislocations. With increasing the temperature and stress at the head of the pile-up, the leading pile-up dislocation may transform into the grain boundary dislocation (i.e. to be converted in the special type of the dislocation which moves in the grain boundary plane). In this case, a new channel for the transmission of the bulk dislocations into the grain boundary interface actives, which is usually called as "pile-up dissolution".

As soon as the test temperature increases above 600-800°C (specifically for tungsten, while for other metals it is much lower), the second deformation mechanism activates. The pile-ups are now effectively dissolved by the grain boundaries, such that plastic deformation propagates between the grains causing "trans-crystalline ductile failure" as soon as the stress-concentration region is formed. Typically, the grain boundary triple junctions, pores and precipitates segregated at grain boundaries act as initial stress concentrators [61]. Finally, above about 1000°C (again in tungsten), the intensive plastic deformation at the grain boundary interfaces takes place, which results in the necking and leads to the so-called "ductile grain boundary failure". In the present work, the mechanical deformation and high flux plasma exposure will be studied at temperature of 600°C and below. Thus, the dislocation slip is expected to be the main mechanism of the plastic deformation.

1.6 Objectives of the present thesis.

It has been shown above that microstructure and mechanical properties play a primary role in the performance of tungsten as a plasma facing material. In particular, DBTT has an intimate correlation with the critical base temperature below which the cracking occurs. Heavy plastic deformation is seen to make a positive impact on the reduction of DBTT. On the other hand, the amount of initial defects such as dislocations and grain boundaries has a clear impact on the retention, since the defects trap plasma components. Therefore, it becomes important to understand and single out the impact of different types of microstructural defects on the plastic deformation and retention in tungsten grades, produced by the commercial route relevant for ITER specification. In this work, we focus on the commercial product fabricated by Plansee AG, produced for the large-scale investigation in the frame of EUROfusion project.

The following scientific and technical objectives for the work were set:

- investigate the process of plastic deformation under tensile deformation in the ITER specification commercial Plansee AG product in the temperature range 300-600°C, which is critical for the low temperature embrittlement;

- provide microstructural characterization of initial state, as-deformed and as-annealed state of the material. Clarify main deformation mechanisms operating under tensile deformation;

- perform deuterium high flux plasma exposure, mimic ITER divertor conditions, using a set of selected samples with distinct microstructure, yet made of initially the same material (i.e. preserving chemistry); develop transmission electron microscopy procedures and sample preparation to obtain reliable and reproducible observations of the surface and sub-surface microstructure of plastically deformed and plasma exposed tungsten;

- investigate the surface, sub-surface and bulk microstructure of the plasma exposed samples. Clarify the impact of the initial microstructure on the plasma-generated microstructure;

- elucidate explanation for the observed changes in the surface properties, such as hardness increase and strong sub-surface retention under high flux plasma.

In order to reach these objectives, the methodology presented in the next section has been followed.

2. Methodology and investigated materials.

In this chapter we shall present the methodology of our experimental work and briefly describe the studied tungsten grades. Methodology description will comprise of the presentation of techniques applied to generate plastic deformation in tungsten, perform plasma exposure (with parameters relevant for ITER), investigate the microstructure at different scale-levels, namely: optical microscopy, scanning electron microscopy and transmission electron microscopy. Attention will be drawn to the procedure of sample preparation required to investigate the top surface and shallow sub-surface layers after the plasma exposure.

2.1 Investigated materials.

Average abundance of tungsten on Earth is about 1 ppm (particle per million) and there are four important tungsten minerals, namely: scheelite, huebnerite, wolframite and ferberite. So called wolframite group (wolframite proper, huebnerite and ferberite) includes minerals containing mixtures of iron tungstate and manganese tungstate $FeWO_4/MnWO_4$. Scheelite is separate from this group as it contains calcium tungstate $CaWO_4$. The five largest tungsten producers in the world are China (with 84.5% of world production), Russia (3.5%), Canada (3.1%), Bolivia (1.7%) and Austria (1.1%).

The extraction of tungsten from its ore consists of several steps. Initially, the ores are separated from their by-products by crushing and grinding. Several intermediate hydrometallurgical steps follow, namely: various actions of mixing, flotation and roasting - with the eventual result being the extraction of tungsten trioxide WO_3. Finally, trioxide is reduced at 1100 K under hydrogen atmosphere, producing the tungsten powder, which is later used for the manufacturing of bulk material by metallurgical processing or other advanced techniques (e.g. spray plasma sintering, powder injection molding, etc.).

Tungsten powder is the basis for the manufacturing of bulk material (i.e. suitable to study both surface and bulk effects). Manufacturing is performed using the techniques of powder metallurgy. The first step of the process is the densification of the powder, then sintering at temperatures in the range of 2300-2800 K in furnaces with hydrogen flow, and finally thermo-mechanical treatment. The latter is needed to induce specific microstructures (like texture, dislocations, grain boundaries) which improve strength and ductility.

In the present work two commercially produced tungsten grades were investigated. Both grades are polycrystalline tungsten of 99.97% purity (of higher) with the same specification on residual impurities that are listed in Table 2.1. Both types are produced by the Austrian company Plansee AG. One grade was supplied in the form of a cylindrical rod, the last fabrication step being hot double forging. The production route, initial microstructure and nominal mechanical properties of these materials were characterized previously in [17]. Hot forging was followed by a thermal stress relief treatment at 1270 K and annealing at 1870 K for one hour. The annealing made the shape of grains more uniform and reduced the dislocation density down to 3×10^{12} m^{-2} on average, as measured by TEM techniques (see Chapter 3). Hereafter, we shall refer to this material as Double Forged Recrystallized – DF_RX grade.

Table 2.1. Impurity content of the tungsten samples.

Impurities	Ag	Ba	C	Fe	Mn	Ni	Ti	Mo	Co	O	Si	Al	Ca	Cr
µg/g	10	5	10	30	5	5	5	100	30	20	20	15	5	20
Impurities	Na	Pb	Zn	H	As	Cd	Cu	Mg	Nb	Ta	Zr	N	S	K
µg/g	10	5	5	5	5	5	10	5	10	20	5	5	5	10

The second material was supplied as a bar with a square cross-section of 36×36 mm^2. The bar was fabricated by hammering on both sides. The grains are therefore needle-like and elongated along the bar axis. Prior to cutting the samples, the bar was annealed at 1273 K for one hour in inert environment. EBSD analysis, presented in the next section, revealed that grains with high mis-orientation angles are randomly mis-orientated and elongated with a grain size of 5-20 µm and 10-100 µm, normal and along the bar axis, respectively. The initial dislocation density is about $(4\text{-}8)\times10^{12}$ m^{-2}, depending on particular sub-grain, with an average of 4.5×10^{12} m^{-2}. We shall refer to this material as IGP tungsten grade (standing for ITER Grade Plansee).

Both grades in as-produced state are in line with the ITER specification: they comply with regulation for chemical composition, density, hardness, grain size (hereafter, grain size is referred to the diameter of the grain or dimensions of the axes, in case the of the elongated grains) and microstructure (more information on the required specification can be found in [4]). However, annealing of the DF_RX grade resulted in grain growth and presumably removal of texture (i.e. preferential crystallographic orientation of grains and sub-grains).

In order to clarify the impact of the initial microstructure and fabrication route another tungsten grade, fabricated in a different way, was also studied. It is a hot-

rolled polycrystalline tungsten sheet (also supplied by Plansee) with a purity of 99.97 wt.% annealed at 1873 K in vacuum. The rolling was applied at temperature above 800°C. This material was provided by IPP Garching, and therefore we label it as IPP grade tungsten.

Microstructural data on the reference materials is provided in Section 3.1.

In addition to the commercially available tungsten, a fourth type was studied: single crystal tungsten material. Single crystal samples (henceforth, SCW) were supplied by Mateck GmbH [18]. The purity of the material is 99.999% and the crystal orientation (110) had an accuracy of 0.1 degree. Initially, the material did not have any structural defects, as was checked by optical, scanning and electron microscopy.

2.2 Specimen preparation.

2.2.1 TEM specimen preparation techniques.

A TEM specimen must be in a solid state, conductive and transparent to the electron beam. Typical TEM specimen holders are designed to hold thin 3 mm in diameter discs-shaped pieces of material. Ideally, specimens should be:

- representative: microstructure should be representative of that found in the bulk material;
- thin: typically up to 200 nm, depending on the atomic mass of the elements in the investigated material and the energy of electron beam;
- largely flat
- undamaged by preparation;
- able to be handled; not fragile;
- stable against oxidation or other degradation;
- free from surface segregation;
- clean.

There are several techniques of producing TEM specimens with the desired characteristics. The choice depends on the material being investigated, with respect to the cons and pros of each method. All methods can be divided in two types – direct formation techniques and indirect methods of investigation or replicas. Direct formation techniques include foil preparation by thinning of bulk material, preparation from the melt, deposition from solution and deposition from vapour.

Replicas are obtained by creating thin foils from material different from the investigated one but copying its surface structure. It is achieved by depositing a thin layer of another material that is afterwards removed and studied in TEM. Such replicas can be lacquer replicas; vapor deposited/spray replicas - materials evaporated and deposited in a vacuum chamber (carbon, metals, silicon monoxide, quartz) and oxide replicas - oxidized material of the object. The disadvantage of replica method is that internal microstructure cannot be examined and that the investigated material surface is usually destroyed by removal of the replica. On the other hand, the advantage is relative ease of preparation and the absence of need to place the actual specimen in the microscope.

Direct formation technique of TEM specimen preparation includes two major steps – cutting of an initial slice from a large piece (bulk) of material and final thinning and polishing.

Cutting of an initial slice is usually done by a cut-off wheel, selected in accordance to the material to be cut or by a fine wire saw. The latter can be a diamond particles covered wire or a wire wetted with an abrasive/etchant containing liquid. Former method is easier and quicker, but the latter one can produce a narrower cut, puts less stress on the sample and has some advantages on cutting brittle materials.

The standard TEM specimen holder is designed to hold material in the form of thin disks 3 mm in diameter. For fairly ductile materials these disks can be mechanically punched using, for example, flat punches or solid punches with concave ends. If the initial slice is too thick for immediate punching, it is mechanically ground to achieve an appropriate thickness.

Final thinning and polishing of a cut slice of material can be performed in several ways – mechanical polishing, chemical polishing, electro polishing, ion beam milling, ultramicrotomy or cleavage.

The choice of a final thinning method is dictated by the properties of the material and how it responds to use the above-mentioned techniques.

The most widely used method is mechanical polishing with SiC paper of different grit sizes followed by electro-chemical final polishing to form a TEM visible area in a specimen.

2.2.2 Tungsten TEM specimen preparation.

As tungsten is brittle at a room temperature, manufacturing 3 mm TEM discs by disc punching is impossible as it results in partial or complete cracking of the specimen. Instead of punching, pieces of material are cut and glued on 3 mm TEM diaphragms.

First step of a typical specimen preparation procedure is cutting initial bulk material into smaller slices. In this work, a Struers Accutom-50 with a diamond cut-off wheel was used. The size of the cut pieces depended on the initial sample size and geometry. The most frequent cut size was 1.8 mm x 10 mm (given that the majority of initial samples were 10x10 mm).

Thinning of a slice of material to a thickness of 100-130 micron was done by manual mechanical polishing on Struers TegraPol-11 with SiC grinding paper of 220 to 4000 grit sizes. Mechanical grinding can cause surface and sub-surface damage up to 3 times the size of particles in the grinding paper. To minimize this problem at each step the thinning was done up to 3 times the size of grinding paper particle. For example the P1200 grit size paper with 15,3 micron particle size was applied to grind off at least 45 micron of surface material.

After the desirable thickness was achieved, the sample was cut into 1.8x2.4 mm pieces with a Well Diamond Wire Saws model 3242. The cut-off pieces were then glued onto standard 3 mm copper TEM diaphragms (Fig. 2.2 (b)).

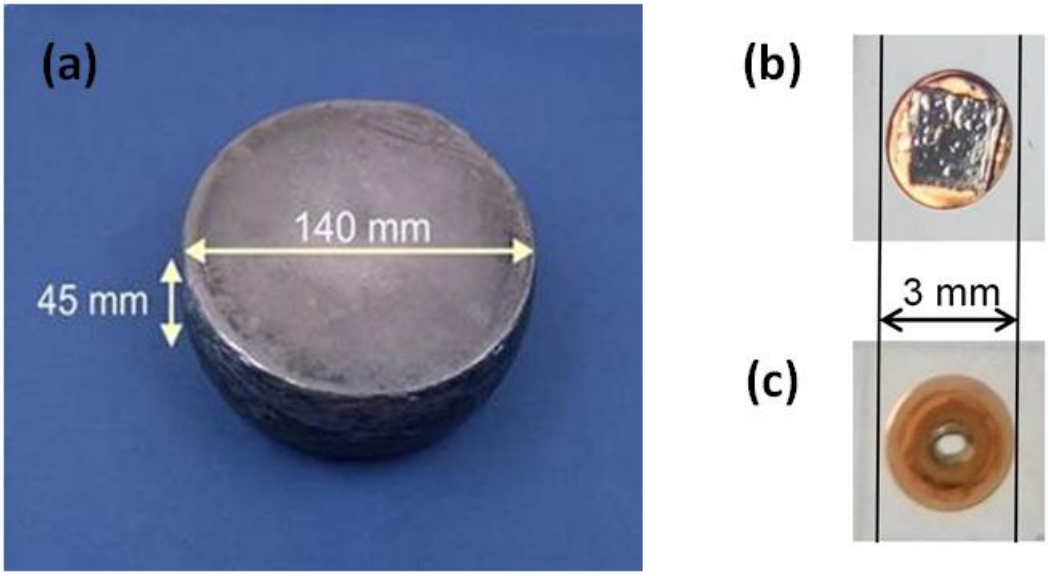

Fig. 2.2. (a) as-received bulk piece of DF_RX material. A thinned and cut piece of tungsten glued on a copper TEM diaphragm before (b) and after (c) electro-chemical polishing.

Final thinning of a specimen was done by electro-chemical technique using a Struers Tenupol-3 automatic electrolytic thinning machine. Electro-chemical polishing solution used was 0.15 wt. % NaOH in water with the voltage set at 30 V. In the conventional method polishing is applied from both sides of the specimen, thinning it to the point when a hole appears in the center of it (Fig. 2.2 (c)). So if the specimen is, for example, 100 μm thick, approximately 50 μm of material is removed from both sides. This procedure cannot be applied to plasma exposed samples though, as the plasma induced change in the specimen structure can be located in a layer much thinner than 50 μm. For this case, so called "back-side" electro-chemical polishing technique was utilized. In this method only one, unexposed, side is thinned and polished thus retaining the other, plasma exposed surface. In this work, this procedure was also used to investigate a depth profile of a specimen microstructure. To achieve this, after the initial back-side polishing and the following TEM investigation, both-sided electro-chemical polishing was consecutively applied with the corresponding TEM investigation after each polishing step. In this way it was possible to study the microstructure in different layers of the specimen, from different depths from the exposed surface.

2.3 Mechanical deformation and plasma exposure.

2.3.1 Mechanical deformation.

It is important to provide extra details about the process used to obtain deformed microstructures, given that one of the particular goals of this study was investigation of the plastic deformation mechanisms in tungsten. The process of application of plastic deformation will be described below.

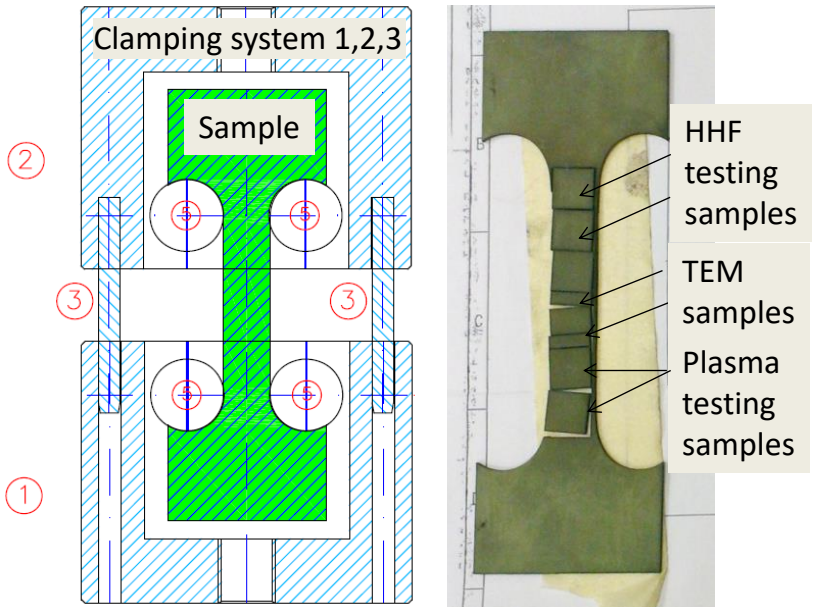

Fig. 2.3.1. Flat macro sample for tensile testing. The left-hand side shows the sample geometry and clamping system, while the right-hand side shows a picture of the loaded sample after EDM cutting to produce samples for TEM examination, high heat flux (HHF) testing and plasma exposure testing.

We have used an Instron pull bench to perform controlled plastic deformation at a well-defined temperature. It was equipped with a furnace and feedback thermocouple to ensure constant temperature during the deformation process. This deformation process was performed at 300°C and 600°C, as this typifies the lower limit for ductility of tungsten and the upper expected temperature limit for the implementation of the water-cooled divertor for DEMO, where the structural integrity of tungsten plays a crucial role.

To enable investigation of the plastically-deformed samples under plasma exposure conditions, it was important to produce large samples for the mechanical load, so that smaller ones could be cut from it for further studies. Flat macro-tensile samples were cut with electric discharge machine (EDM) from the middle of the supplied bulk material, as shown in Fig. 2.3.1. To reduce the induced stress due to EDM cutting tensile samples were re-annealed at 1000°C for 1 hour in an argon (Ar) atmosphere. The special pull-line was designed to insert 160 mm length sample with the gauge length of 120mm and working section of 11 mm. Such samples were cut from DF_RX, IGP and IPP grade tungsten. A photo of a sample placed in the furnace for testing in the Instron machine is given in Fig. 2.3.2.

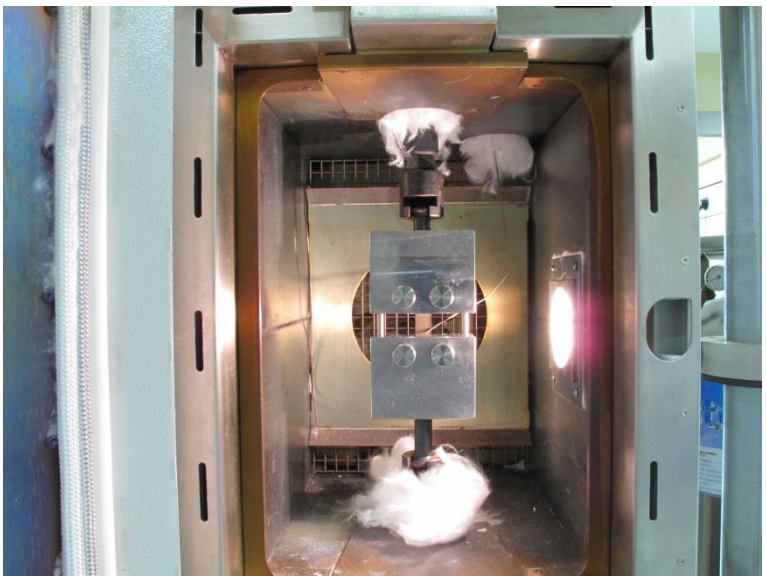

Fig. 2.3.2. A sample in the furnace of the Instron machine. The thermocouple wires are attached to the gauge section of the sample.

Tensile tests were performed at 300°C and 600°C with a deformation rate of 0.2 mm/min in an argon atmosphere and an example of the resulting true stress-strain (σ-ε) curve is given in Fig. 2.3.3. More results will be presented in Section 3. The samples for TEM investigation and plasma exposure were cut with EDM from the gauge section which experienced uniform elongation.

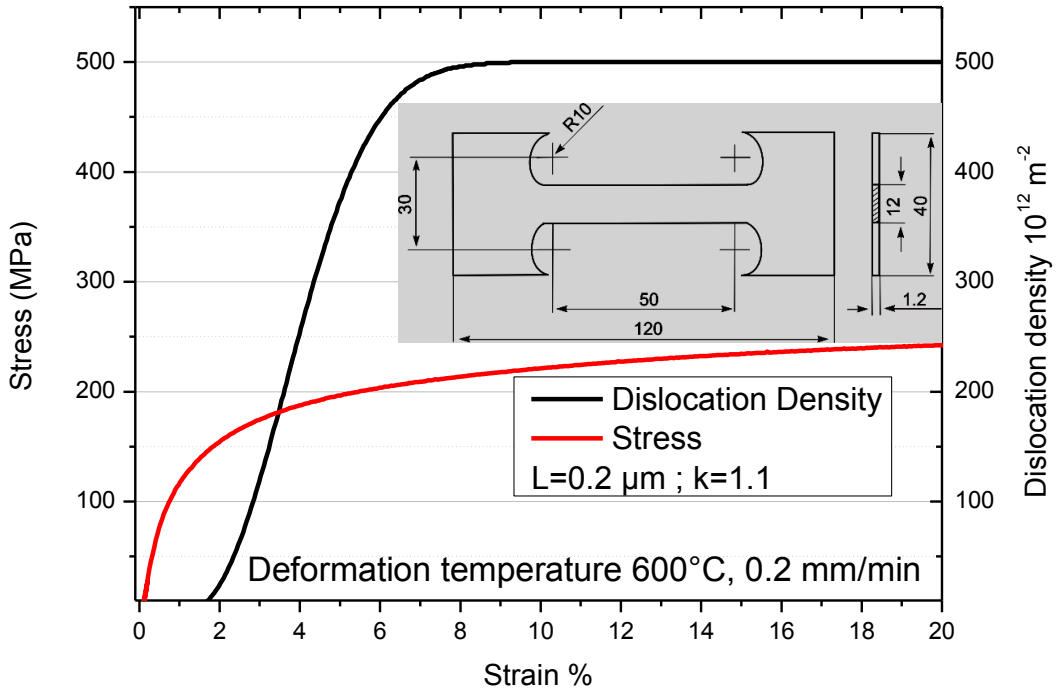

Fig. 2.3.3. Stress-strain curve of DF_RX grade tungsten tested at 600°C with a crosshead speed of 0.2 mm/min. The inset figure shows the sample geometry. The secondary y-axis refers to the dislocation density evaluated by fitting the strain-hardening curve to the Mecking-Kocks equation (see details in [19]).

2.3.2 High flux plasma exposure.

Tungsten samples were exposed to a pure deuterium plasma in the Pilot-PSI linear plasma generator [20, 21], which delivers a high-density, low-temperature plasma mimicking the 'sub-displacement threshold' plasma wall interaction conditions expected in the ITER divertor.

Figure 2.3.4 shows the experimental setup of Pilot-PSI with the location of the diagnostic tools to measure surface temperature (infra-red imaging) and local plasma conditions (Thomson scattering). The deuterium plasma is produced with a cascaded arc source, originally developed at the Eindhoven University of Technology and optimized by DIFFER.

The operation regime of the deuterium gas flow into the source was between 1 – 3 slm (standard liter per minute, which corresponds to 4.5×10^{20} particles per second). Plasma was formed in the discharge channel by an ionizing current of 150 – 250 A. Plasma then expands out of the high pressure source into a cylindrical vacuum vessel (Ø 0.4 m and

1m long). During plasma operation the pressure in the vacuum chamber typically was 1 – 3 Pa. The vacuum chamber is surrounded by oil cooled coils that produce an axial magnetic field of 0.4 – 1.6 T axi-symmetric to the source. The magnetic field radially confines the expansion of the plasma and generates an intense magnetized cylindrical beam to the target. Due to the cooling requirement of the coils, Pilot-PSI runs in pulsed mode.

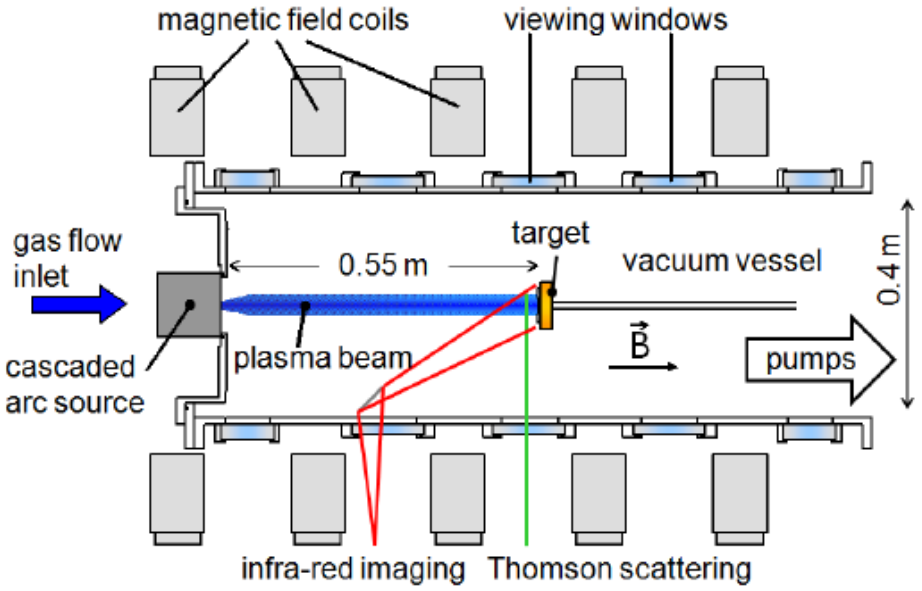

Fig. 2.3.4. Schematic drawing of Pilot-PSI plasma generator setup. The main elements are reflected on the drawing.

A sample is installed normal to the plasma beam and is clamped onto a copper holder (also acting as heat sink), which is cooled with flowing water (1 – 6 L/min). The sample is polished several days prior to the exposure and then stored in the desiccator to reduce oxidation. Due to the floating schedule of the device, it is impossible to predict exactly the day of the exposure. To enhance the thermal contact, a graphite-oil film is placed between the sample and the holder. From the description above, it follows that the surface temperature on the sample is not actively controlled but is defined by the balance of the power load and heat removal. This means that exactly equivalent exposures are impossible to perform in principle, but repeating the exposure conditions showed that with similar surface temperatures, - which varied within ±25°C from one shot to another - were possible to achieve, simply requiring fine preparation of the samples, good thermal contact with the holder and stable water flow.

The sample of 10×10×1 mm size was electrically grounded so that a negative bias with respect to the plasma potential could be applied in order to adjust the ion energy to the required level. The deuterium ion energy was ~50 eV (controlled by negatively

biasing the target), while energies in excess of 900 eV are required to initiate atomic displacement in tungsten [22]. Although the plasma beam was non-uniform (full width at half maximum ~10 mm), the relatively small sample area ensured a small temperature gradient across the surface. Fig. 2.3.5 shows an example of the temperature profile across the sample during plasma exposure, with a target temperature of 200°C.

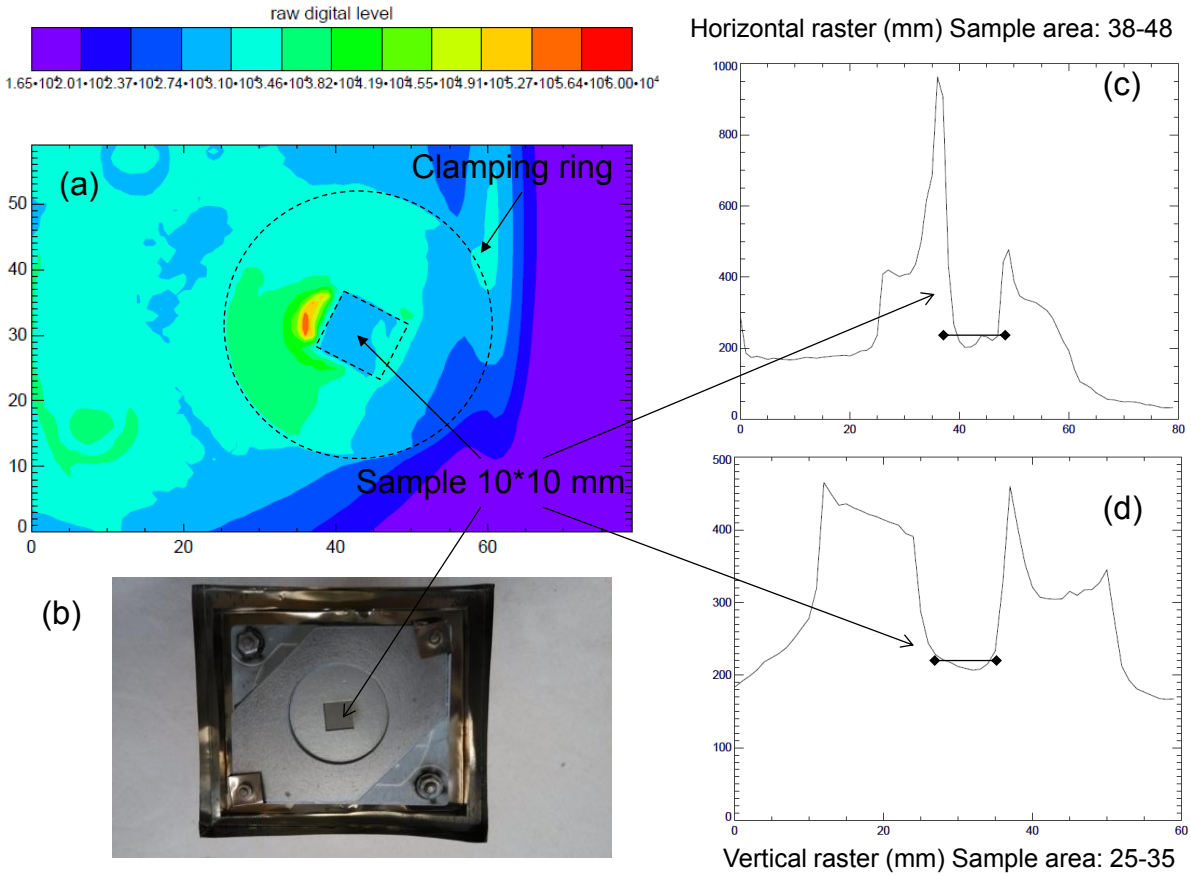

Fig. 2.3.5. (a) raw digital level signal of the infra-red camera scanning the area near the sample holder. The clamping ring and sample areas are shown in dashed lines. (b) photo of the sample clamped by the similar rig and placed on the TDS heating stage. (c) and (d) is, respectively, horizontal and vertical distribution of the temperature across the sample holder, as calculated on the basis of the infra-red camera measurements. Sample position is shown by the black line. Temperature is in degree C.

For the samples studied here, the deviation from the desired temperature was ±10°C, as measured and confirmed by an infra-red camera (FLIR A645 sc). The maximum particle flux in the center of the sample was ~7×10^{23} D/m²/s. Flux was calculated from the plasma electron density and electron temperature, as measured by Thomson scattering [23] at a distance of ~25 mm upstream from the plasma-facing surface.

2.4 Transmission electron microscopy and analysis.

Visible light microscopy resolution is limited by the range of visible light wave lengths. Electron microscopy can overcome this limit by using high energy electrons with wavelengths several orders of magnitude shorter than that of visible light. A 200 keV electron wavelength is about 2.3 pm, which is much smaller than the diameter of an atom. Thus, by substituting visible light particles with electrons and optical lenses with electro-magnetic ones, we can conduct investigations at a nano-scale level.

In transmission electron microscope a high-energy beam of electrons hits a thin specimen generating a variety of signals. Some of them are summarized on Fig. 2.4.1.

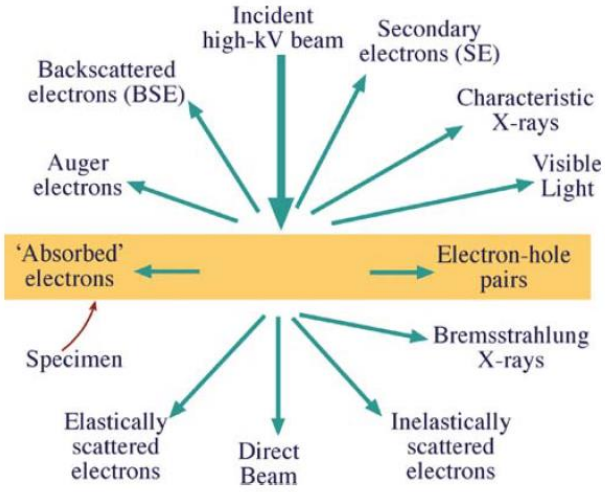

Fig. 2.4.1. Signals generated upon interaction of a high-energy beam of electrons and a thin specimen.

Electron-specimen interactions can be divided in two main groups – elastic and inelastic scattering. Elastic scattering generates signal that is the main source of contrast on TEM images and diffraction patterns (DP). Signals generated by inelastic scattering are used in Electron Energy Loss Spectroscopy and Energy-dispersive X-ray Spectroscopy. These techniques are core instruments of Analytical Electron Microscopy and provide information on the chemistry and electronic structure of the specimen.

TEM images can be formed in a bright field (BF) mode and a dark field (DF) mode. The BF TEM image is acquired when diffracted beams are cut off by the objective aperture

of the TEM and the image is formed with only the transmitted electron beam. The DF image is formed by selecting only the diffracted beam(s).

2.4.1. TEM image mode.

In imaging mode the electrons emerging from the specimen are guided by the electro-magnetic lenses of the TEM to form an image that is projected onto the viewing screen or CCD camera. There are two main origins of TEM image contrast – amplitude and phase contrast. In turn, amplitude contrast has two principal types - mass-thickness contrast (or Z-contrast) and diffraction contrast

Phase contrast is the result of interference between the transmitted and the diffracted beams.

Mass-thickness contrast arises from a strong dependency of scattering power upon atomic number 'Z' and the thickness (more material, hence, more mass) of the specimen. Thicker or higher-Z parts of the specimen will scatter more electrons off axis resulting in less intensity of the signal in the transmitted beam in comparison with thinner or lower-Z areas.

Diffraction contrast is another form of amplitude contrast. It arises when the electrons are scattered at special (Bragg) angles, therefore it is controlled by the crystal structure and orientation of the specimen. Diffraction-contrast image is acquired by selection of single transmitted or Bragg-scattered beam. In a perfect single crystal such amplitude will be uniform and there will be no contrast. But if some defects are present, for example dislocations or dislocation loops, distortion of the crystal lattice will give raise to diffraction contrast. For example, the presence of a dislocation will result in scattering of electrons on it and loss of intensity in the transmitted beam. In case of the BF mode the dislocation line will appear dark on the bright background and in the DF image it will be vice versa.

2.4.2 TEM diffraction mode.

In diffraction mode electro-magnetic lenses collect all the electrons that have been scattered through particular angle in one point. Thus, each point in a DP represents a differently oriented set of planes that satisfy the diffraction condition. In case of crystalline materials DPs allow determination of crystallographic orientations of the investigated specimen. Given the small size of the incident electron beam, it can be done very locally, down to nm level.

Imaging mode and diffraction mode are the primary modes of TEM operation and the main sources of microstructural information. Obtaining both a DP and an image from the same area of a specimen is a core strength of a TEM.

In this work TEM investigations were performed with a JEOL 2010 TEM operating at 200 keV located at CIEMAT, Madrid, Spain and JEOL 3010 TEM operating at 300 keV, located at SCKCEN, Mol, Belgium. Both microscopes are equipped with LaB6 electron emission gun.

2.4.3. Dislocation density calculation.

Regardless of the method, calculating dislocation density in the area of a given TEM micrograph requires determination of specimen thickness at that exact location. There are two main ways of doing so - electron energy loss spectroscopy analysis (EELS) and convergent beam electron diffraction (CBED) pattern analysis.

When a beam of electrons with a known value of kinetic energy passes through the specimen, some of the electrons can be scattered inelastically and thus lose energy. This energy loss can be measured in an electron spectrometer and the acquired spectra then analyzed to identify the thickness of a specimen in the given area.

In this work CBED pattern analysis was utilized, where specimen thickness can be measured from a single image of a CBED pattern. In diffraction mode of TEM the incident beam is focused on a specimen to form a fine convergent probe (usually ~1–100 nm in diameter), unlike a parallel beam used for obtaining diffraction patterns. The electrons in a convergent beam enter the specimen at different angles and can then be diffracted over twice the incident angle. The different angles result in the formation of disks, rather than dots, on a diffraction pattern.

Under two-beam conditions – with only one strongly exited reflection – each disc in a CBED pattern contains parallel lines (Kossel-Möllenstedt fringes (K-M fringes)). Such contrast is caused by variations in intensity arising from the difference in relation between the angle of the incident beam and the number of diffracted electrons for each point in the disc. The theory behind intensity distribution is discussed in [62].

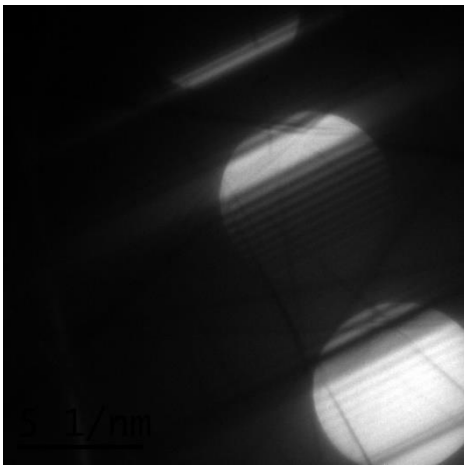

Fig. 2.4.2. An example of a CBED pattern.

Specimen thickness can be calculated with the following formula:

$$\left(\frac{s_i}{n_i}\right)^2 = -\left(\frac{1}{\xi_g}\right)^2 \left(\frac{1}{n_i}\right)^2 + \left(\frac{1}{t}\right)^2 \quad (2.1)$$

where s_i is the excitation error of the *i*th minimum, n_i is an integer that indicates with which minimum of the K-M fringe this minimum corresponds, ξ_g the extinction distance for that specific reflection g and t is specimen thickness. The excitation error can be calculated using the following expression:

$$S_i = \frac{\Delta\theta_i}{2\theta_B} g^2 \lambda \quad (2.2)$$

where $\Delta\theta_i$ is the distance between the middle of the central bright fringe and each of the dark fringes, θ_B is the Bragg angle for the diffracting plane, **g** is the reciprocal vector and λ is the relativistic wavelength of the electrons in Å. $2\theta_B$ is just the separation of the *ooo* and *hkl* disks on a CBED pattern and λ can be calculated as λ (Å)= $12.2643/(E_o + 0.97845 \times 10^{-6}E^2)^{1/2}$ [63], where E is the acceleration voltage in volts. A recorded CBED pattern with K-M fringes contains all the necessary information to determine the thickness of the specimen in the given area:

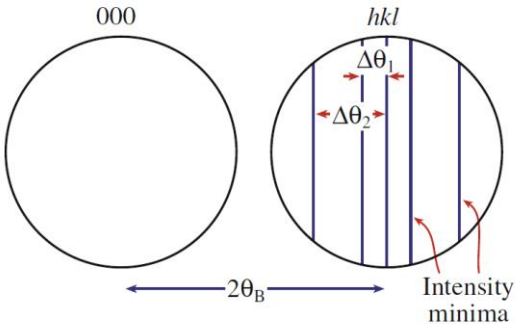

Fig. 2.4.3. Schematic drawing of two CBED discs indicating distances between them ($2\theta_B$) and distances between dark fringes (minimum intensity) and the central bright fringe ($\Delta\theta_i$).

Expression 2.1 shows that there is a linear dependence between $(s_i/n_i)^2$ and $(1/n_i)^2$. The slope of this line equals $-(1/\xi_g)^2$ and its intersection with the Y-axis equals $(1/t)^2$. For a specimen thickness $t < \xi_g n_i$ equals 1, for $\xi_g < t < 2\xi_g$ $n_i = 2$, etc.

In practice, the relation between $(s_i/n_i)^2$ and $(1/n_i)^2$ is plotted on a graph for several values of n_i starting with 1. Only the correct value of n_i will give a straight line.

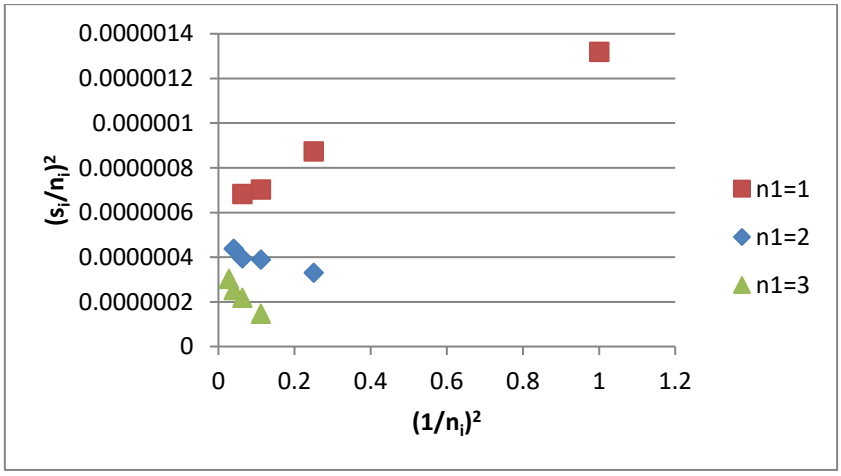

Fig. 2.4.4. A relation between $(s_i/n_i)^2$ and $(1/n_i)^2$ plotted on a graph for several values of n_i.

Then the specimen thickness in the given area can be calculated from the intersection of this line and the Y-axis.

Once the specimen thickness is determined it is possible to calculate dislocation density. Two methods were used in this work.

The first method involves direct calculation and summation of lengths of all the dislocations on the TEM micrograph via a dedicated TEM imaging sensor software and dividing it over the volume, given that we already know the thickness and can calculate the surface from the same micrograph.

The second method is described in [64]. In the TEM software, a circle is drawn randomly in an image and the number of intersections of it with dislocation lines is counted (see Fig. 2.4.5). Dislocation density is then calculated as $\rho=2N/Lt$, where N is the number of intersections of the circle with dislocation lines, L – length of the circle, t – local thickness of the specimen at the area of the image. The length of the circle is automatically calculated in the software package.

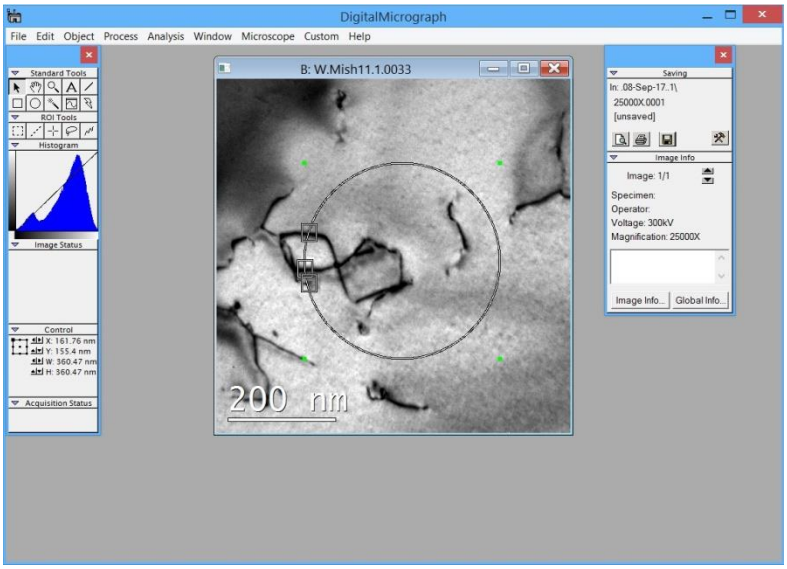

Fig. 2.4.5. A window of a TEM software program showing a process of counting the number of intersections of dislocation lines with a randomly drawn circle in a TEM micrograph.

The choice of method depends on the microstructure of the material being studied. If the images show high inhomogeneity, low count of dislocations or short length, the direct calculation method is easier to apply and it gives more accurate results. For example, on Fig. 2.4.6 (a) only two dislocation lines are observed, so a randomly placed circle can have zero, one to two intersections. That would translate in the dislocation density being zero or up to 2, if one or two intersections are taken into account. In cases like this the direct calculation method will give more accurate results. On the other hand, if observed dislocations are numerous or hard to define precisely, like on Fig. 2.4.6 (B) the second method is much faster and just as accurate.

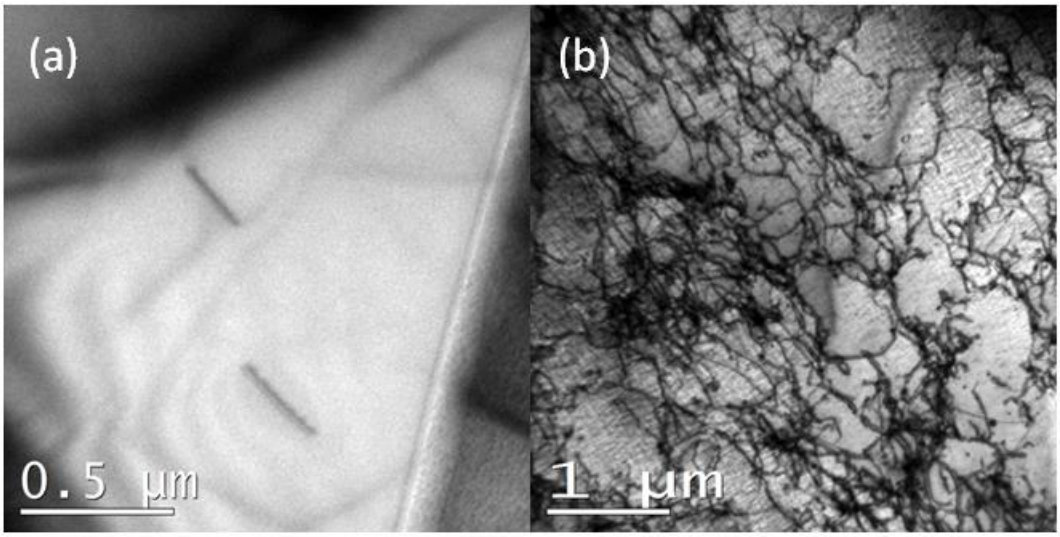

Fig. 2.4.6. TEM micrographs showing an example of different number of dislocations observed in one picture.

An important factor for correct dislocation density calculation is accounting for visibility/invisibility of dislocation lines depending on the diffraction conditions of each particular TEM micrograph used for density calculation. In accordance with dislocation invisibility criterion a screw dislocation will be invisible if $\mathbf{g}\cdot\mathbf{b}=0$, where **g** is a diffracting vector and **b** is Burgers vector of a dislocation [65]. For an edge or mixed dislocation Burgers vector **b** is no longer parallel to the dislocation line vector **u**, and the invisibility criterion has more conditions to satisfy. For such dislocation to be invisible, $\mathbf{g}\cdot\mathbf{b}$ and $\mathbf{g}\cdot\mathbf{b}\times\mathbf{u}$ must be both zero. In cases when only first condition is satisfied, an edge dislocation will show some faint contrast because $\mathbf{g}\cdot\mathbf{b}\times\mathbf{u}$ is not zero.

In practice, correction coefficients can be calculated for two types of dislocation burgers vectors observed in BCC tungsten - $a_0/2\langle 111\rangle$ and $a_0\langle 100\rangle$. First, $\mathbf{g}\cdot\mathbf{b}$ values are calculated for different g reflections, see Table 2.4.1.

Table 2.4.1. The values of **g•b** for the first three possible reflections in BCC material and $a_0/2\langle 111\rangle$ Burgers vector.

	Possible Burgers vector			
Reflection	$a_0/2[111]$	$a_0/2[\bar{1}11]$	$a_0/2[1\bar{1}1]$	$a_0/2[11\bar{1}]$
110	1	0	0	1
101	1	0	1	0
011	1	1	0	0
$\bar{1}10$	0	1	$\bar{1}$	0
$\bar{1}01$	0	1	0	$\bar{1}$
$0\bar{1}1$	0	0	1	$\bar{1}$
200	1	1	1	1
020	1	1	$\bar{1}$	1
002	1	1	1	$\bar{1}$
$\bar{2}00$	$\bar{1}$	1	$\bar{1}$	$\bar{1}$
$0\bar{2}0$	$\bar{1}$	$\bar{1}$	1	$\bar{1}$
$00\bar{2}$	$\bar{1}$	$\bar{1}$	$\bar{1}$	1
211	2	0	1	1
121	2	1	0	1
112	2	1	1	0
$\bar{2}11$	0	2	$\bar{1}$	$\bar{1}$
$\bar{1}21$	1	2	$\bar{1}$	0
$\bar{1}12$	1	2	0	$\bar{1}$
$2\bar{1}1$	1	$\bar{1}$	2	0
$1\bar{2}1$	0	2	$\bar{1}$	$\bar{1}$
$1\bar{1}2$	1	0	2	$\bar{1}$
$21\bar{1}$	1	$\bar{1}$	0	2
$12\bar{1}$	1	0	$\bar{1}$	2
$11\bar{2}$	0	$\bar{1}$	$\bar{1}$	2

From the first several rows of Table 2.4.1 it follows that for any $g=\langle 110\rangle$ half of $a_0/2\langle 111\rangle$ dislocations will be invisible. The proportion of invisible dislocations for the first three possible **g** vectors in BCC material is given in Table 2.4.2.

Table 2.4.2. Proportion of Burgers vector invisible in BCC material under two-beam diffraction conditions.

Diffraction condition	Proportion of invisible $a_0/2<111>$ Burgers vector	Proportion of invisible $a_0<100>$ Burgers vector
g=<110>	1/2	1/3
g=<200>	0	2/3
g=<211>	1/4	0

From this table one can see that, for example, under a two-beam diffraction conditions with g=<110> half of $a_0/2<111>$ dislocations and one-third of $a_0<100>$ dislocations will be invisible. Our calculations show that an average proportion of these two dislocation types is 70% and 30% correspondingly. Taking this into account, in an image taken with a g=<110> and having an actual dislocation density of ρ we will observe (and calculate) a dislocation density ρ_v (where "v" stands for - visible) that will be equal to: $\rho_v = 1/2 \cdot 0.7 \cdot \rho + 2/3 \cdot 0.3 \cdot \rho$. From this equation it follows that an actual dislocation density under this diffraction conditions is ~1.81 times higher than a visible one. Following the same logic, correction coefficients for g=<200> and g=<211> were found to be 1.25 and ~1.21 correspondingly.

As a methodology for the calculation of dislocation densities we used the following steps: firstly, scanning different parts of the specimen to see the general microstructure and locate areas of interest and areas representative to the specimen; next, capturing 15-25 micrographs suitable for analysis along with corresponding diffraction patterns and CBED patterns to determine specimen thickness and invisibility correction coefficients specifically for each micrograph, from which an average dislocation density is then calculated.

The dedicated TEM software used was DigitalMicrograph version 3 by Gatan.

2.4.4 Supporting techniques

Electron backscatter diffraction (EBSD) is a microstructural-crystallographic characterization technique that is used to study grain size, shape, misorientation in polycrystalline materials as well as defects, phases, strain and deformation analysis inside the grains. It is based on recording and indexing of so-called Kikuchi lines that are produced by the backscattered electrons that are subsequently diffracted by the crystal planes. EBSD patterns are obtained using a SEM equipped with a dedicated EBSD detector. To do so, a flat-polished specimen is installed in the SEM chamber at an angle of approximately 70° from horizontal in order to maximize the intensity of the

resultant EBSD pattern. The electron beam is then focused on the area of interest and some of the back-scattered electrons, leaving the specimen, will be Bragg diffracted [66] by the crystal planes and form the Kikuchi lines on the phosphor screen of the EBSD detector placed in their way. These images are then recorded by a CCD/CMOS sensor of the EBSD detector and can be automatically indexed afterwards (using the look up tables with international crystal data bases) in the dedicated software in order to identify the diffracting planes and calculate the crystal orientation in the given spot. This basic method, coupled with modern computer technologies, makes possible the recording and indexing of patterns with a speed up to several thousand per second. In turn, it allows to perform detailed orientation mapping of polycrystal samples and acquire EBSD maps showing grain boundaries and grain orientation and giving various statistical information on grain misorientation, grain size and crystallographic texture.

In this work EBSD investigations were performed with a JEOL 6610LV SEM with the Bruker QUANTAX EBSD system.

Nuclear reaction analysis (NRA) is a technique used to measure concentration of certain chemical elements as a function of depth from the probed surface in a solid specimen. It is especially useful in case of measuring light atoms in heavy matrix. The principle of the NRA is the following – an incident ion beam enters the specimen and loses energy proportional to the penetration depth. At a certain depth ion particles can undergo a nuclear reaction with chemical elements in the matrix. If the initial kinetic energy of the ion beam and its energy loss per distance travelled in the specimen is known, the depth at which the nuclear reaction will take place can be calculated. Thus, changing the initial energy of the projected ion beam, different depths in the specimen are probed in order to obtain the intensity of nuclear reaction at the corresponding depth and calculate the concentration of a chemical element in question.

In the case of D(3He; p)α type nuclear reaction, no variation of the incident beam energy is needed as the energy of the fast proton detected depends on the depth of the deuterium atom in the sample.

The NRA measurements were carried out using a 3 MV accelerator which emits highly energetic ^{3}He ions. These can be used to probe for the presence of deuterium, thanks to the nuclear reaction of D(^{3}He; p)α type. The latter is an exothermic reaction which emits a 11-14 MeV (kinetic energy) proton. After the nuclear reaction is initialized, the reaction products (p;α) are captured by detectors and their energy distribution and scatter cross-sections provide information on the depth profile of deuterium in the investigated layer. The resulting depth resolution is defined as the ratio of the energy range of the detected particles (generated at certain depth, which is obtained by the best fit) and the effective stopping power. The results presented below were obtained using a standard procedure previously developed at IPP Garching by Alimov and co-workers (see e.g. [44, 50]). NRA measurements were performed in the central part of

the sample, corresponding to the highest flux. The D(^{3}He, p)α nuclear reaction was used by exposing the sample to a ^{3}He beam at multiple energies (0.5, 0.69, 1.2, 1.8, 2.5, 3.2, 4.5 MeV). This enables the collection of information from different depth regions. For the currently employed range of ^{3}He ion energies, the deuterium depth profiles can be accurately measured up to a depth of 6 μm. The shape and intensity of the proton spectrum for each ^{3}He beam was analysed and fitted. The reconstruction of depth profiles was performed using the SimNRA [67] and NRADC [68] software packages.

The purpose of nanoindentation (NI) is to measure the hardness of small volumes of material with high precision, thus allowing data collection from the probed volume down to tens of nanometers. NI methodology is the same as traditional indentation testing (i.e. macro or micro indentation) - a hard tip with known mechanical properties (usually diamond) is pressed into a sample, the properties if which are to be determined. The load applied to the indenter tip is increased as the tip penetrates more deeply into the specimen until it reaches a user-defined value. At this point, the load is removed and the back-force (elastic rebounding force) acting on the indenter is measured. The hardness of the material can therefore be determined at different indentation depths with high accuracy up to a penetration depth of one micrometer. It is important to note that during the NI process the actual extension of the plastic zone (propagation of the geometrically necessary dislocations) under the indenter is considerably larger than the penetration depth itself. Usually, this extension of the plastic zone is considered to be larger by a factor of about 5-10, dependent upon the material being tested and the test temperature. Thus, when the response of the material is analyzed, this phenomenon should be taken into account, and therefore instead of the penetration depth (h_{NI}) we use the term called "Plastically Affected Region" taken to be 5× h_{NI}.

Nano-indentation measurements of the reference and exposed samples were performed using an Agilent G200 NI machine to obtain both the Young's modulus and hardness. The indentation measurements were performed in continuous stiffness mode (CSM) [69] using the standard XP head equipped with a Berkovich diamond tip. The oscillation amplitude and frequency were respectively 2 nm and 45 Hz. The indentation strain rate was set to 0.05 s^{-1} and the specimens were indented down to a penetration depth of h_{NI}=1.5 μm. Two zones on the exposed sample were investigated by performing 25 indents arranged in a square and spaced 60 μm apart. These two indentation zones were located in the middle of the sample and about 2mm apart. Sample hardness was calculated using the classical Oliver & Pharr method [69]. Calibration for the tip area function was performed by carrying out a series of indents in a reference fused silica sample.

3. Experimental Results.

In this chapter the experimental results are presented and discussed. The Chapter is subdivided into three sub-sections dealing with: characterization of the original microstructure of the studied materials, evolution of the microstructure due to the plastic deformation, and finally the microstructure after the high flux plasma exposure. Obtained TEM results are presented and discussed through each sub-section. At the end of the last sub-section, the supporting experimental data obtained by other colleagues on the materials studied here is presented to substantiate the summary and conclusions given in chapter 4.

3.1 Investigation of reference microstructure.

In this section, we provide some basic information about the reference microstructure of three polycrystalline tungsten grades studied. This comprises optical, scanning and transmission electron microscopy images to illustrate the grain size, texture and dislocation patterns.

The reference microstructure of the above mentioned grades was investigated by three types of microscopic analysis, namely: Visible Light Microscopy (VLM), SEM-EBSD and TEM techniques. The corresponding images are provided in Fig. 3.1.1-5, respectively. To better understand the differences in the microstructure, it is useful to recall the fabrication route, described in details in Section 2.1.

DF_RX, IGP and IPP grades were fabricated by Plansee AG and have nominally the same composition. DF_RX was produced as a rod and then annealed at 1600°C for one hour. IGP was produced by double hammering and was supplied in the shape of a bar with a square cross-section. Prior to the investigation, IGP was annealed at 1000°C to degas from gas impurities. IPP was produced as sheet of 1 mm thickness by hot rolled deformation, and the investigated samples were annealed at 1600°C to achieve large grain size and reduce dislocation density.

VLM images, shown in Fig. 3.1.1, show that DF_RX material exhibits large grains, which are equiaxed in shape. The IGP has fine grain structure with elongated grains and thus likely has a texture (grain boundaries orientation is biased by forging process in one direction). Finally, IPP also has big grains, equiaxed in shape as well, but somewhat smaller than grains of DF_RX.

Larger magnification and therefore more detail of the grain and sub-grain morphology could be obtained by SEM-EBSD analysis. The latter is presented in Fig. 3.1.2. It clearly

shows that the IGP material has a texture and typical size of grains is about 50-150 μm and 10-30 μm normal to and along the forging direction (see figure caption and above provided description). So the aspect ratio of the grains is about 20. Many sub-grains are present inside the grains, their size is below 5 μm and can go down to less than 1 μm. The forging axis is evident for the IGP samples, see Fig.3.1.2(b). The DF_RX grade appears to have grains with a size of about 50-150 μm, see Fig.3.1.2(a), and some of the grains (only few) reach size of up to 200 μm. Finally, the EBSD map for the IPP, show on Fig. 3.1.2 (c), demonstrates that the size of grain is about 10 to 50 μm and grains are clearly equiaxed. Note that IPP grade has many grains adjusted by the low angle grain boundaries (i.e. the colour contrast is weak), whereas the DR_RX material has large grains which are mostly connected by high angle grain boundaries (i.e. intensive colour contrast suggesting high mis-orientation angle, see Fig. 3.1.2(a)).

The most detailed information on the morphology of the sub-grains as well as dislocation density values was obtained by TEM analysis. The composite images for the three studied grades are presented below.

The DF_RX grade, shown in Fig. 3.1.3, appears to have sub-grains which have rather uniform size distribution (mean size of about 2.5-5 μm) and dislocation density estimated to be about (2-8)×10^{12} m^{-2}. The average dislocation density is found to be 2.8×10^{12} m^{-2}. Note that the SEM-EBSD analysis revealed that a typical grain size is in the range of 50-150 μm. Thus, the sub-grain size is about ten times smaller than the grain size. The sub-grains are mainly connected by low angle grain boundary interfaces.

The IGP grade, shown in Fig. 3.1.4, demonstrates very a complicated microstructure, consisting of many sub-grains, which have elongated shape (coinciding with the forging direction). Their size varies in the range 0.6 – 1.7 μm and 2.3 – 4 μm, respectively, normal to and along the elongation directions. It is important to note that the size of elongated grains is so large that several grains cannot be resolved on the composite TEM image from a single sample. Higher magnification allows one to resolve dislocation lines. Their density appeared to be less than one would initially expect (given that the materials was only degassed at 1000°C after the fabrication). The dislocation density is about (4-8)×10^{12} m^{-2}, depending on particular sub-grain, and is 4.5×10^{12} m^{-2} on average.

Finally, a TEM composite image of IPP is shown in Fig. 3.1.5. The analysis has revealed mostly the presence of either high angle mis-oriented grain boundaries, or the presence of triple junctions. An example of such a triple junction is shown in the inset of Fig. 3.1.5. The results of TEM observations cannot be used to make a statistically reliable estimation of the grain orientation because the low numbers seen, however SEM-EBSD examinations are more reliable. The dislocation density is about 5×10^{12} m^{-2}, which is not so low, despite the fact that the material was annealed at 1600°C.

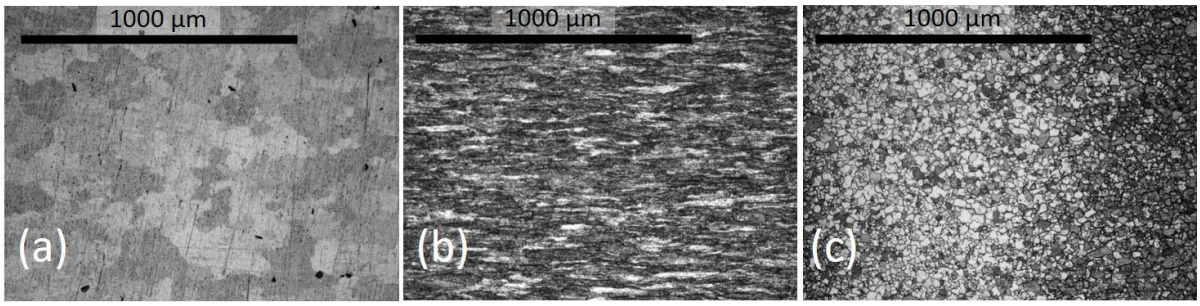

Fig. 3.1.1. Visible light microscope images of (a) DF_RX, (b) IGP and (c) IPP tungsten grades. The forging direction in Fig(b) goes from left to right.

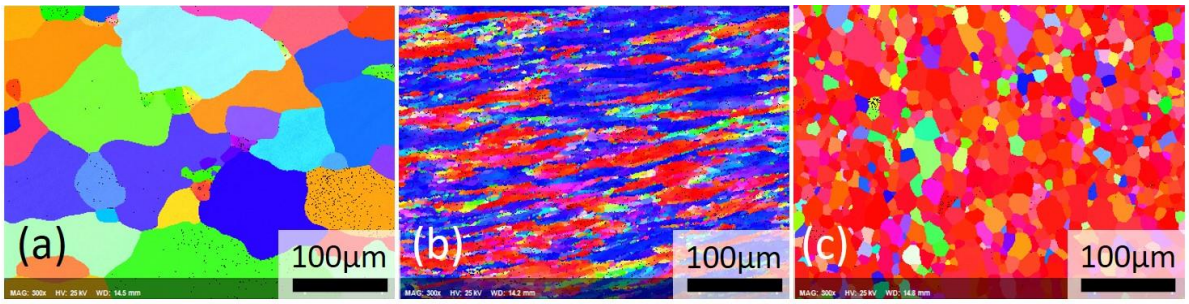

Fig. 3.1.2. EBSD images of (a) DF_RX, (b) IGP and (c) IPP grades. In Fig.(b) the forging axis goes from left to right.

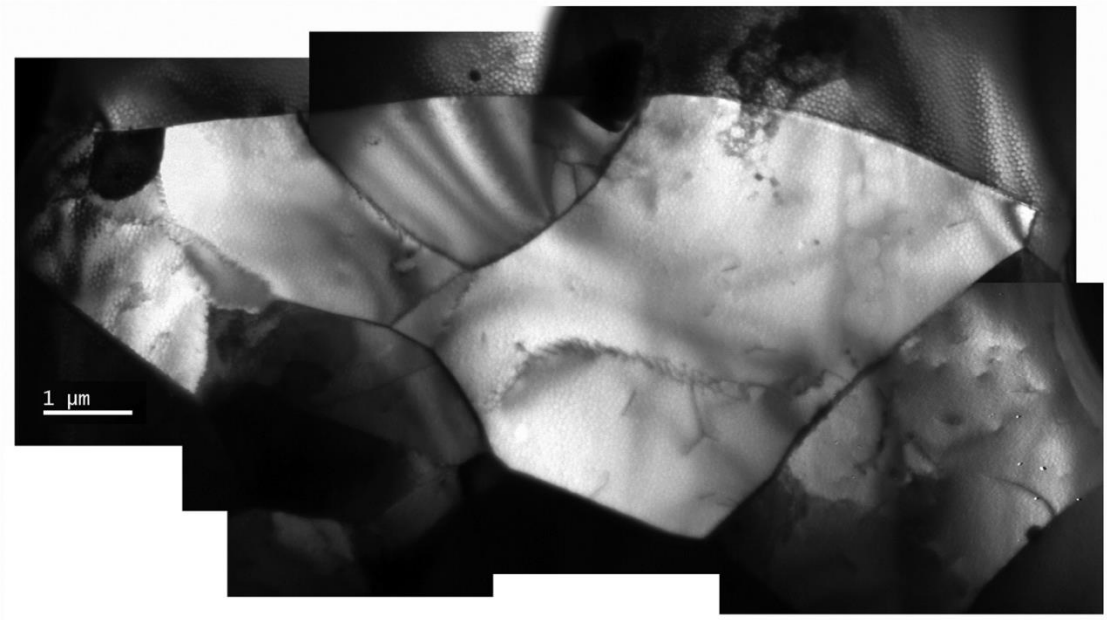

Fig. 3.1.3. Composite TEM image of DF_RX grade.

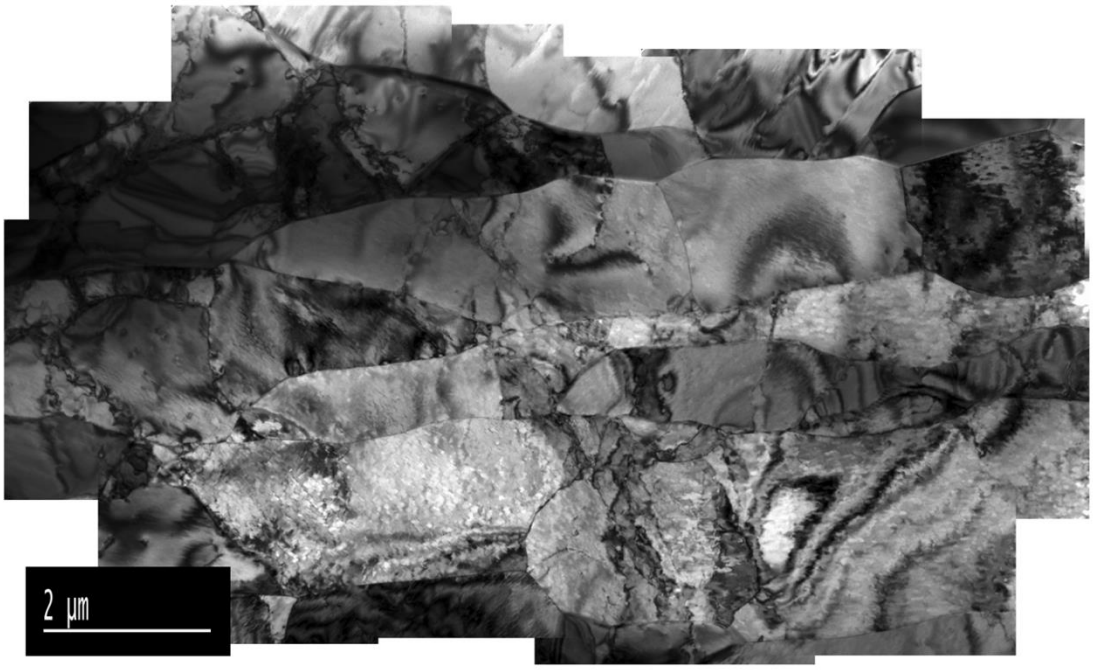

Fig. 3.1.4. Composite TEM image of IGP grade.

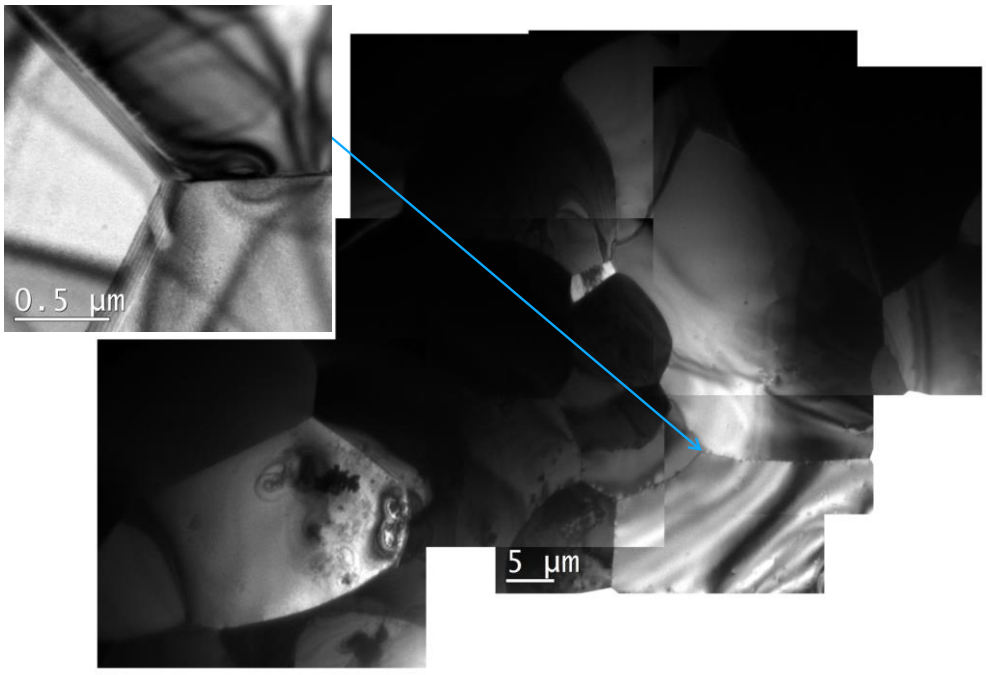

Fig. 3.1.5. Composite TEM image of IPP grade.

Finally, we present the data of the tests done using micro-hardness measurements (MHM), these results are shown in Fig. 3.1.6. The hardness of the three grades of tungsten and that of a single crystal (with <110> surface orientation) at different loads is measured by employing the micro Vickers hardness method. Note that the surface of the studied samples was prepared in the exactly same way as was used for the VLM and

EBSD. The single crystal was fabricated and polished by the factory (we did not apply any additional surface treatment after this, or before the plasma exposure), while other tungsten grades were cut from the blocks and polished in our lab.

For the single crystal, the measurements reveal that the hardness decreases with increasing indentation test load from 410 HV down to 340 HV. No such decrease was observed for the electro-chemically polished W grades. We attribute this difference to the residual defects present on the surface due to the mechanical polishing. However, once the large enough weight of the indenter is used, the hardness saturates to a value of 340-350 HV and apparently the effect of residual defects on the surface does not play any further role. Hence, for hardness measurements employing a weight exceeding about 0.2 kg the presence of residual defects due to mechanical polishing should not affect the response of the material.

From the data measured in the range of 0.2-2 kg, we conclude that single crystal has the lowest hardness – as expected because of the absence of structural defects inside the material. The IGP has the highest hardness, about 430 HV, while the IPP and DF_RX grades are located in between (360-380 HV).

As TEM examination established, the main difference between DR_RX/IPP and IGP is the removal of high number of sub-grains and the increase of grain size. The dislocation density between DF_RX and IGP material was not very different. Thus, we can conclude that the higher hardness of IGP should be attributed to the presence of numerous small sub-grains (in particular, to the thin lath-like sub-grains formed due to the forging). Hence, the present measurements using the Vickers hardness test could also help to distinguish the signature of the microstructure consisting of textured heavily deformed sub-grains. This observation can be useful for the analysis of the plastically deformed materials and those exposed to the plasma.

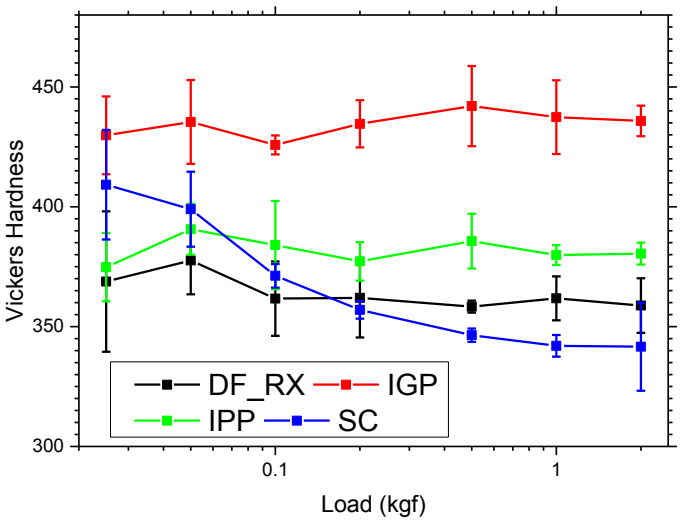

Fig. 3.1.6. Micro-hardness of three polycrystalline tungsten grades.

3.2 Plastic deformation mechanisms under tensile load.

3.2.1 Mechanical tests.

In this section, the results of mechanical tests and the corresponding post-deformation TEM investigations are reported. The deformation of different polycrystalline grades is compared and conclusions regarding the character of the plastic deformation and dominating mechanisms are discussed. Most of the tests were performed at 600°C, but for the IPP grade we also performed the test at 300°C.

The results of the mechanical tests are presented in Figs. 3.2.1-4, which show the engineering stress-strain curves. The non-recrystallized IGP (see Fig. 3.2.2) clearly shows strongly different response to the applied load as compared to the DR_RX (see Fig. 3.2.1) and IPP (see Fig. 3.2.3), which were annealed at 1600°C. The yield stress in the two recrystallized samples, RF_RX and IPP, is 102.5 MPa and 98 MPa respectively, i.e. it is practically the same, whereas the yield stress in the IGP is much higher and calculated to be 470 MPa. The evident increase of the yield stress in the IGP should be undoubtedly associated with the fine sub-grain microstructure and/or higher dislocation density. Almost the same yield stress measured in the DR_RX and IPP grades points to the fact that grain boundaries are likely to be the defects controlling the onset of the yield of the material.

Fig. 3.2.4 shows stress-strain curves of IPP tungsten deformed at 300°C. When compared to the results obtained at 600°C, we can see the presence of a spike at the onset of the yield. This is so called upper yield strength, which is associated with the

presence of interstitial impurities (like carbon) which segregate as a result of the applied annealing. These impurities form clouds near the dislocations such that a higher stress needs to be applied to release the dislocations from these atmospheres. This phenomena is called yield drop [60].

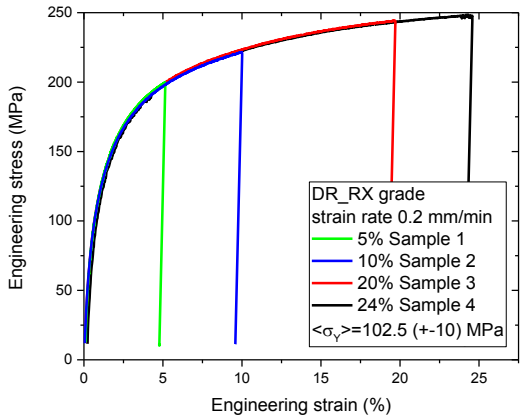

Fig. 3.2.1. Stress-strain curves of DF_RX grade deformed at 600°C.

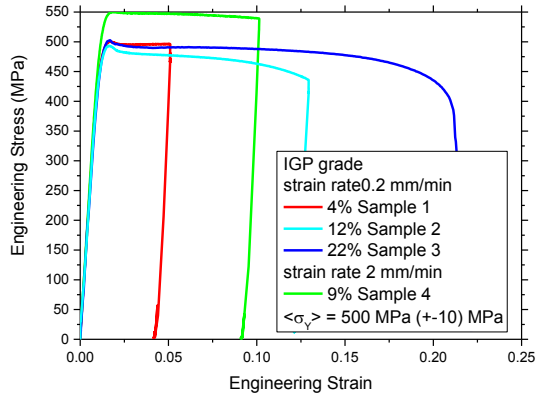

Fig. 3.2.2. Stress-strain curves of IGP tungsten deformed at 600°C.

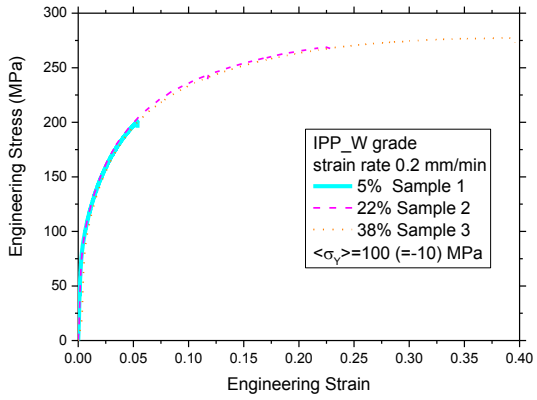

Fig. 3.2.3. Stress-strain curves of IPP grade deformed at 600°C.

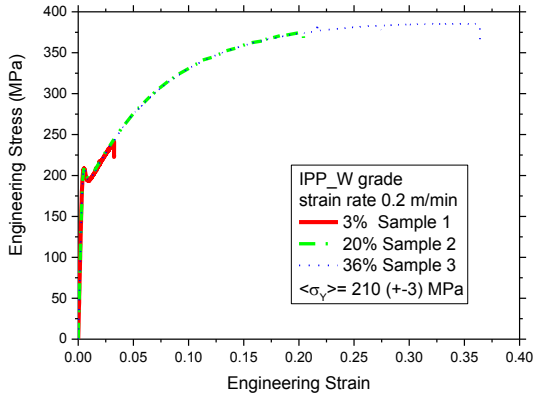

Fig. 3.2.4. Stress-strain curves of IPP grade deformed at 300°C.

In order to investigate the impact of the plastic deformation on the microstructure, the interrupted deformation tests were performed to achieve different level of strains. Depending on the investigated grade, we have typically picked the deformation strain about 5%, 10% and 20%. Since IPP has shown very large deformation strain to fracture, we have also investigated 40% deformation strain in this material.

The appearance of grains after the deformation process was studied by VLM measurements. The results are presented in Fig. 3.2.5, 3.2.6 and 3.2.7 for respectively, DF_RX, IGP and IPP grades. In the case of DR_RX which has the largest grains, see Fig. 3.2.5, the elongation of grains as a result of the plastic deformation is evident. For other two materials it is less pronounced. However, for all these inspected materials we can conclude that the grains detectable by VLM techniques did not experience a remarkable change of their size as compared to the non-deformed state (i.e. there were no obvious formation of new high angle grain boundaries). Thus, the main response of the material to the applied deformation occurred within the VLM-detectable grains.

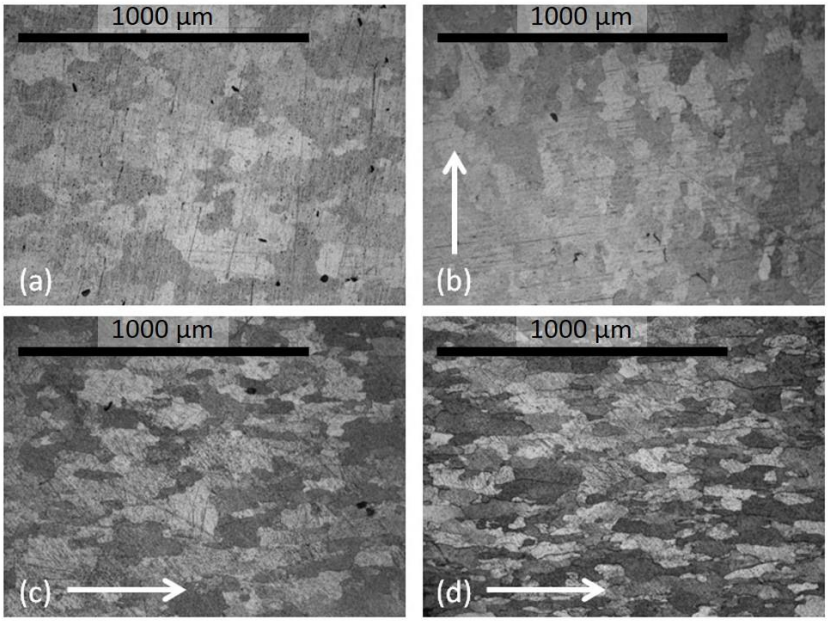

Fig. 3.2.5. Visible light microscope images of DF_RX grades in (a) the reference state and deformed to (b) 5%, (c) 20%, (d) 28% of strain. The deformation direction is shown by an arrow added to the images.

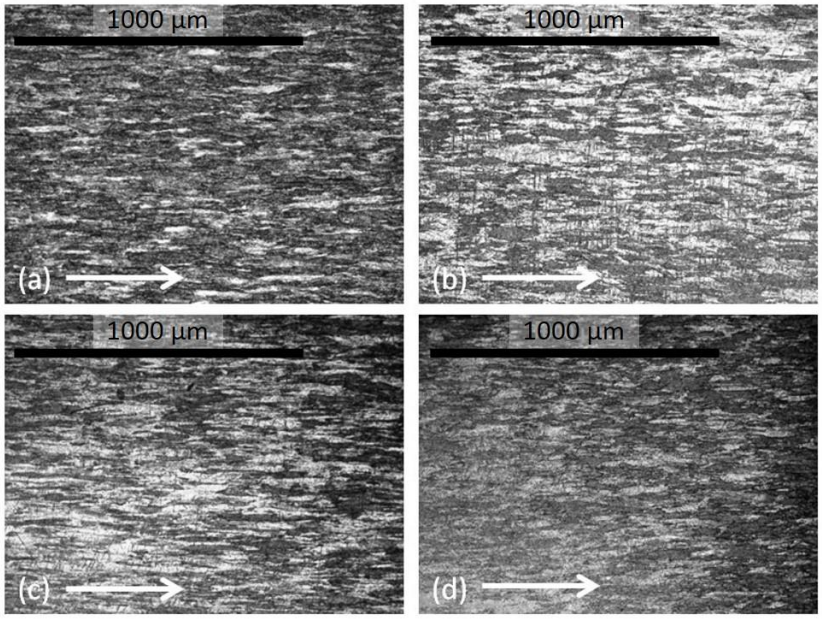

Fig. 3.2.6. Visible light microscope images of IGP grades in (a) the reference state and deformed to (b) 4%, (c) 9%, (d) 22% of strain. The deformation direction is shown by an arrow added to the images.

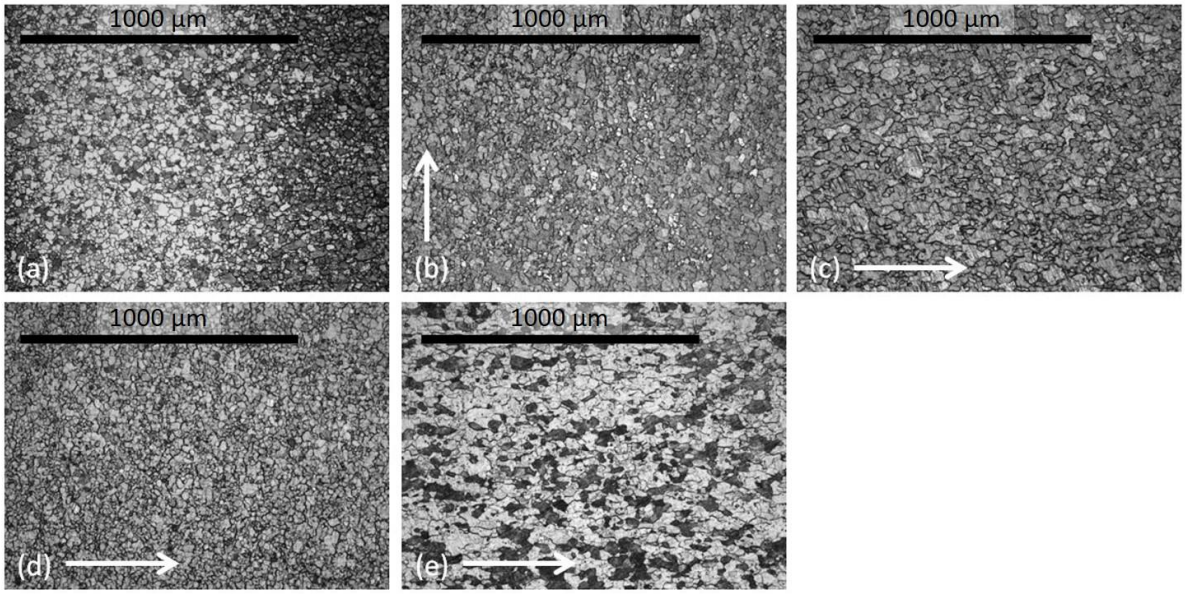

Fig. 3.2.7. Visible light microscope images of IPP grades in (a) the reference state and deformed to (b) 3%, (c) 37% at 300°C as well as (d) 5%, (e) 22% at 600°C. The deformation direction is shown by an arrow added to the images.

3.2.2 TEM investigation of the plastically deformed materials: DF_RX grade tungsten.

Here we begin by showing TEM results from plastically deformed samples of the DR_RX material, micrographs of these are shown in Fig. 3.2.8. Evolution of the dislocation microstructure with an increase of deformation level is demonstrated. It is notable that while only screw dislocation segments with Burgers vector $a_0/2\langle 111\rangle$ were observed in non-deformed and 5% deformed samples, a densely tangled dislocation network (with a significant presence of edge component) was found in the 20% and 28% deformed samples. Moreover, in the 20% deformed samples, regions with dense dislocation pile-ups forming next to the grain boundary interfaces were regularly seen, and in the 28% deformed sample a limited grain refinement had started to take place. The latter can apparently be explained by local sub-grain re-orientation under heavy plastic deformation. Several TEM micrographs demonstrating these observations are presented below in Figs. 3.2.9-13, and must be accounted for when discussing the evolution of dislocation density versus applied strain.

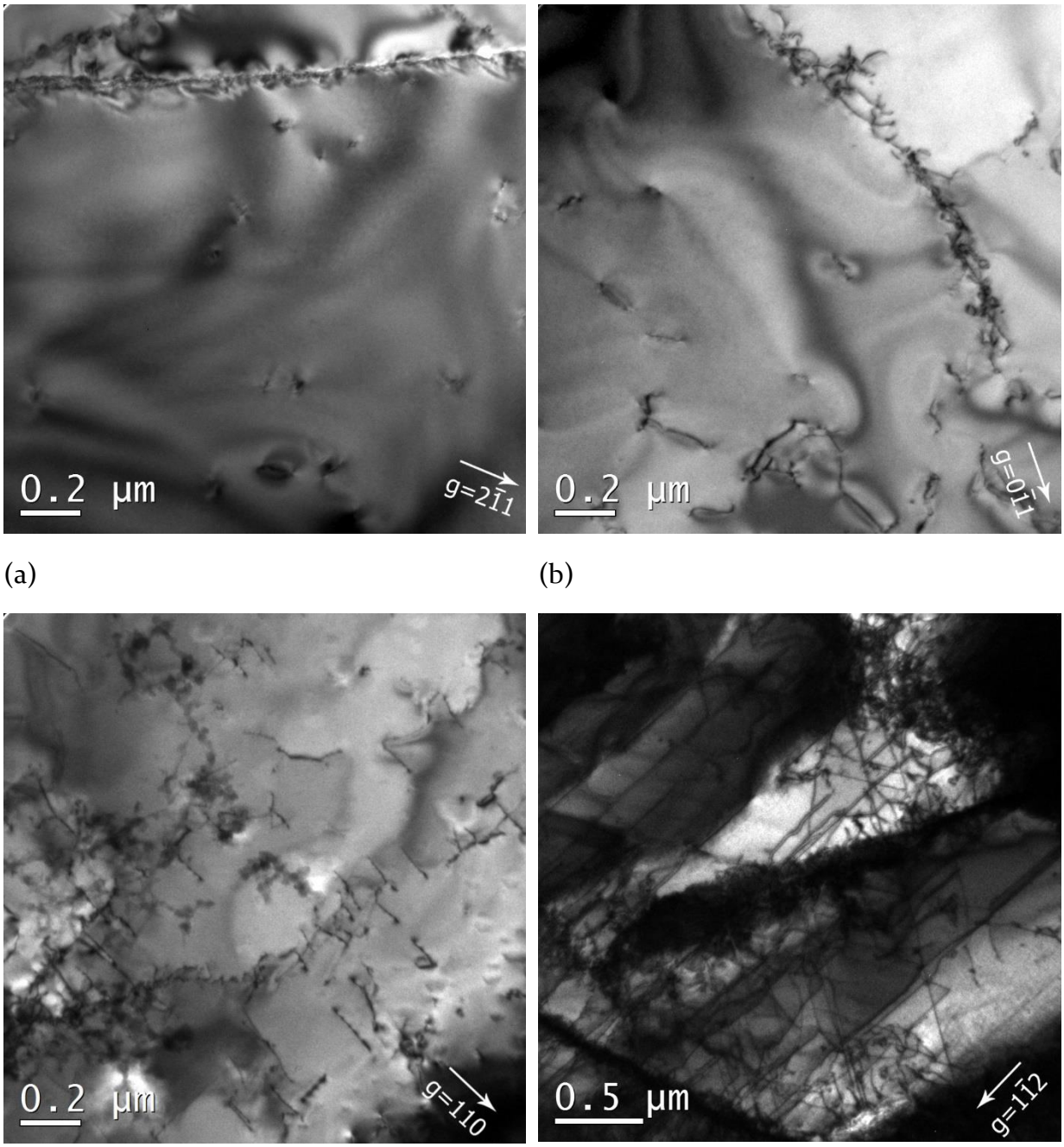

(a) (b)

(c) (d)

Fig. 3.2.8. TEM micrographs showing a typical dislocation pattern in tungsten corresponding to (a) as-annealed condition, g=(2$\bar{1}$1) (211)and close to a [113] zone axis; (b) 5% deformed, g=(0$\bar{1}$1) and close to a [011] zone axis; (c) 20% deformed, g=(110) and close to a [001] zone axis; (d) 28% deformed, g=(1$\bar{1}$2) and close to a [111] zone axis.

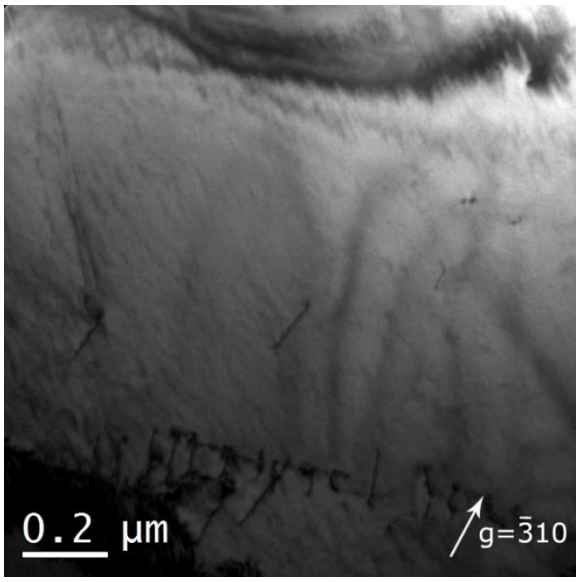

Fig. 3.2.9. TEM micrograph showing inhomogeneous distribution of dislocations in the non-deformed DR_RX sample, g=($\bar{3}$10) and close to a [$\bar{1}$33] zone axis.

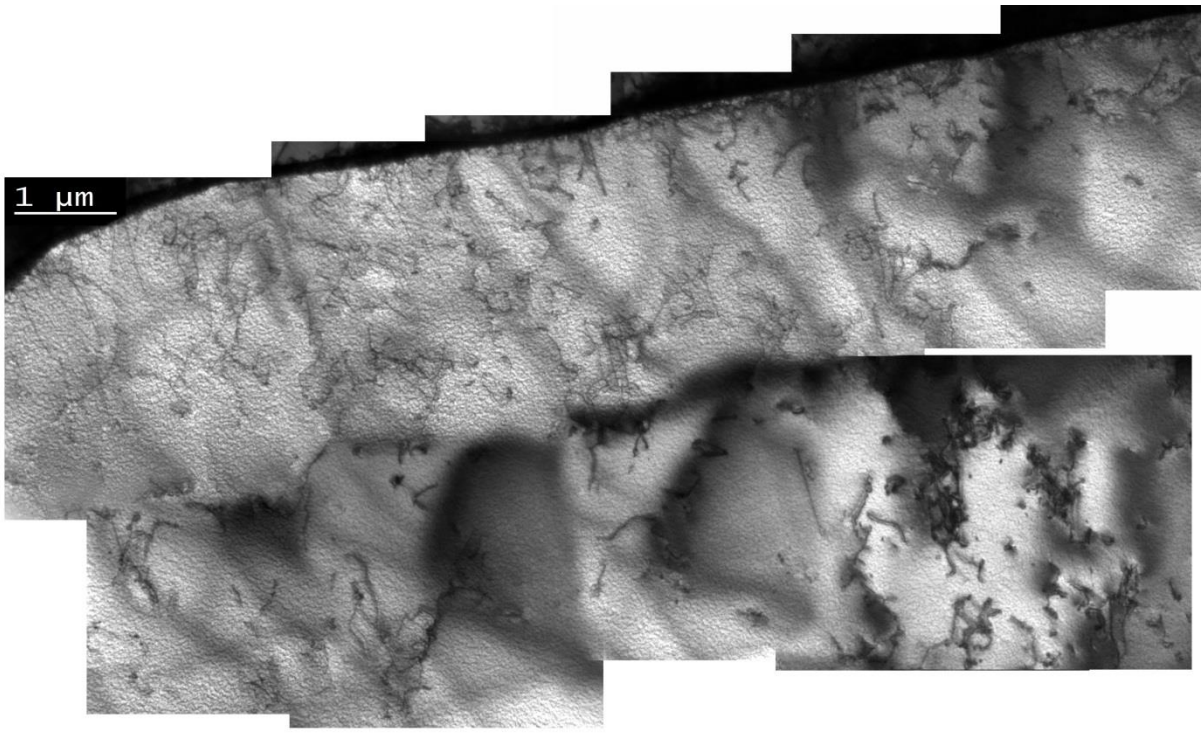

Fig. 3.2.10. Composite TEM image of the 5% deformed DF_RX sample showing a reduction of the inhomogeneity in the distribution of dislocations and overall increase of the dislocation density in comparison with the non-deformed tungsten sample.

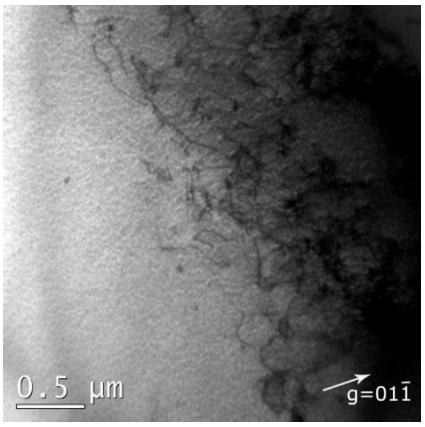

Fig. 3.2.11. TEM micrograph showing inhomogeneous distribution of dislocations in 5% deformed DF_RX sample, g=(01$\bar{1}$) and close to a [111] zone axis. In particular, it is possible to see the front of the dislocation forest and defect-free material.

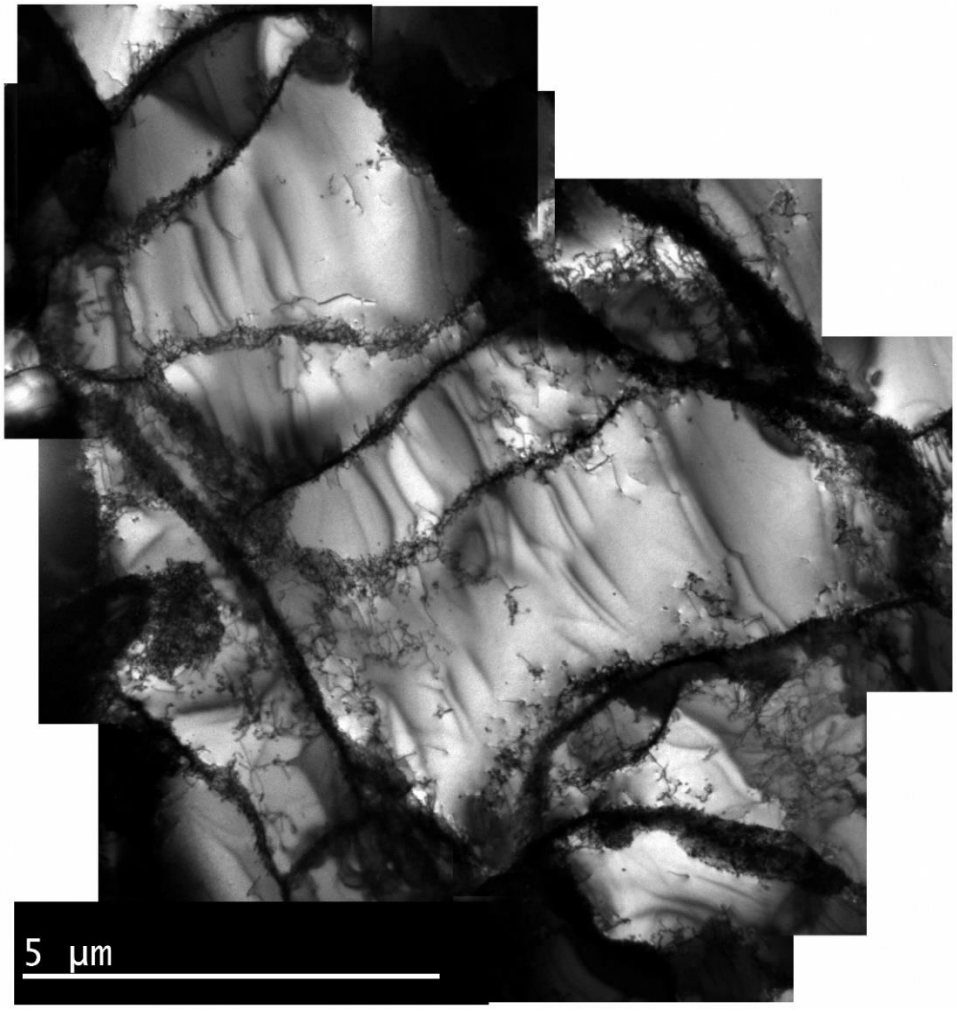

Fig. 3.2.12. Composite TEM image of a 20% deformed DF_RX sample showing initiation of grain refinement, dislocation pile-ups next to grain boundaries and increased dislocation density in comparison with the as-annealed non-deformed and 5% deformed DF_RX samples.

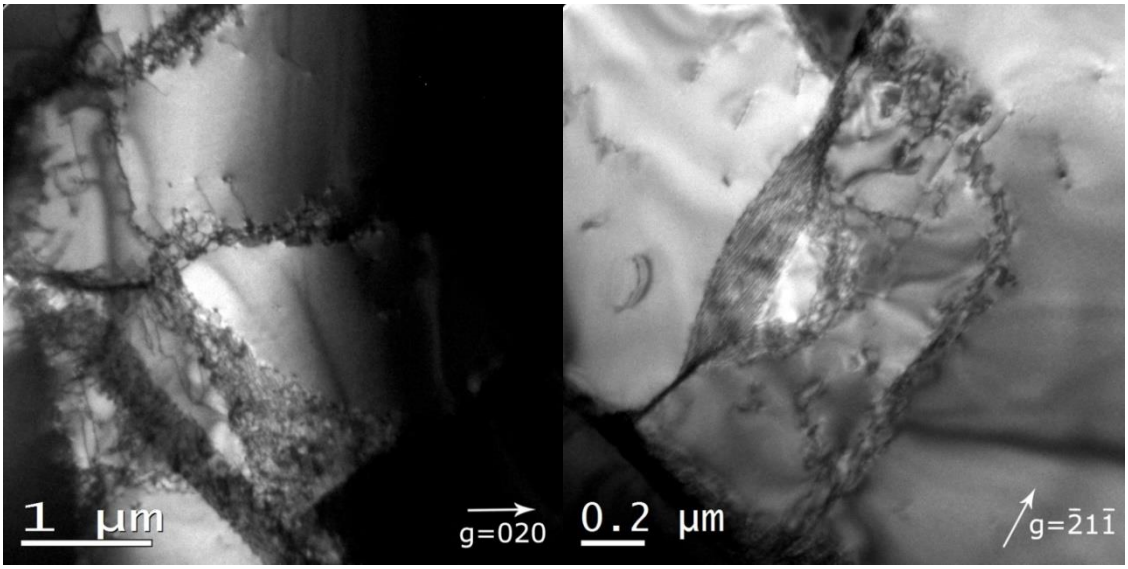

Fig. 3.2.13. TEM micrographs showing dislocation pile-ups in front of grain boundaries in 20% deformed tungsten sample, g=(020) and close to a [001] zone axis; g=($\bar{2}1\bar{1}$) and close to a [011] zone axis.

3.2.3 TEM investigation of the plastically deformed materials: IGP tungsten.

The next set of images illustrates the microstructure of the plastically deformed IGP tungsten. TEM micrographs discussed below were usually taken so as to respect the elongation axis being left-right on the figures. However, in some cases, it was impossible to find a good zone for TEM measurements, and in this case the elongation axis is shown by an arrow to guide an eye.

Figs. 3.2.14-16 present composite TEM images of the microstructure obtained after 4, 9 and 22% of deformation. The elongation axis is evident in each figure. Note that all these measurements were taken in the post-necking deformation regime, because the ultimate tensile strength (UTS) in the IGP is typically reached at about 0.5-1% of plastic stain. Another important detail to note is that for the deformation states at 4% and 9% strain, the engineering stress was approximately the same being around 490 and 485 MPa, and slightly reduced down to 440 MPa at 22%. The actual local stress was apparently much higher which intuitively appears from the evolution of the microstructure shown in the figures. Below we describe it in more details.

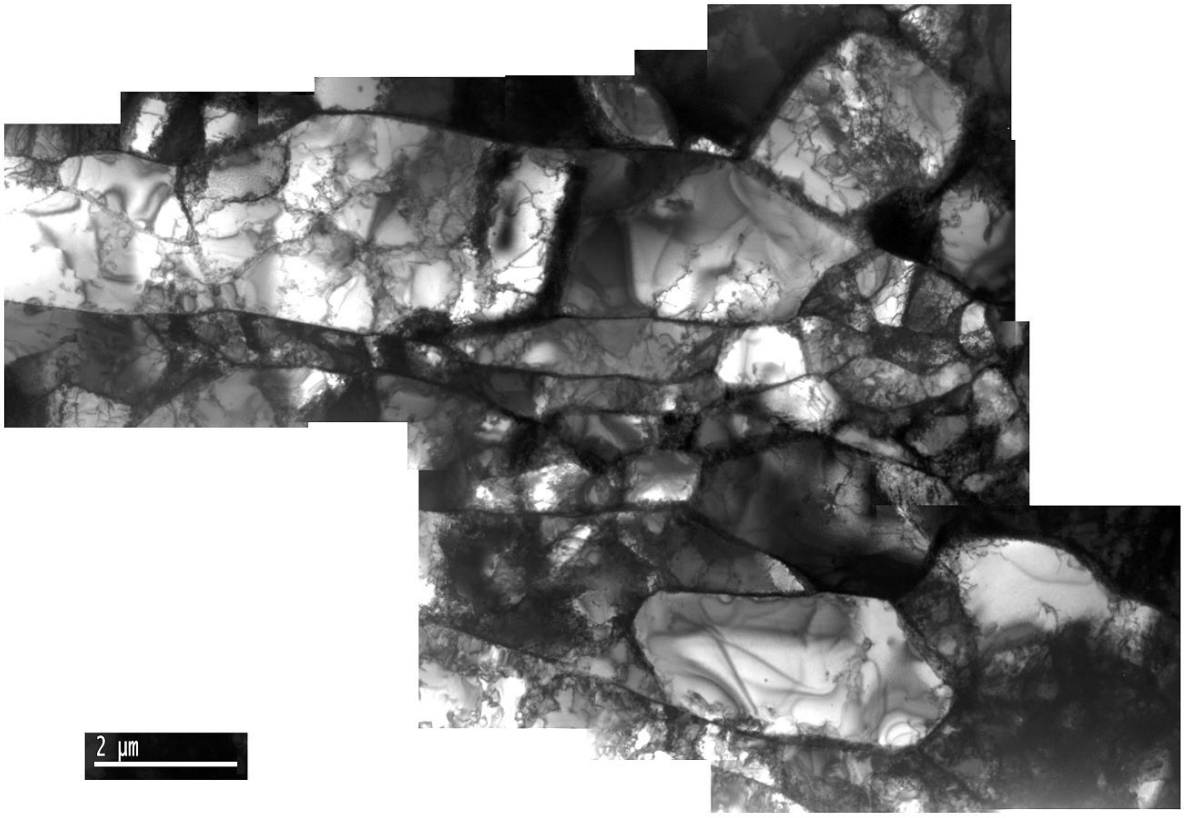

Fig. 3.2.14. Composite TEM image of the microstructure of IGP material deformed up to 4%. The sub-grains are elongated in the left-right direction.

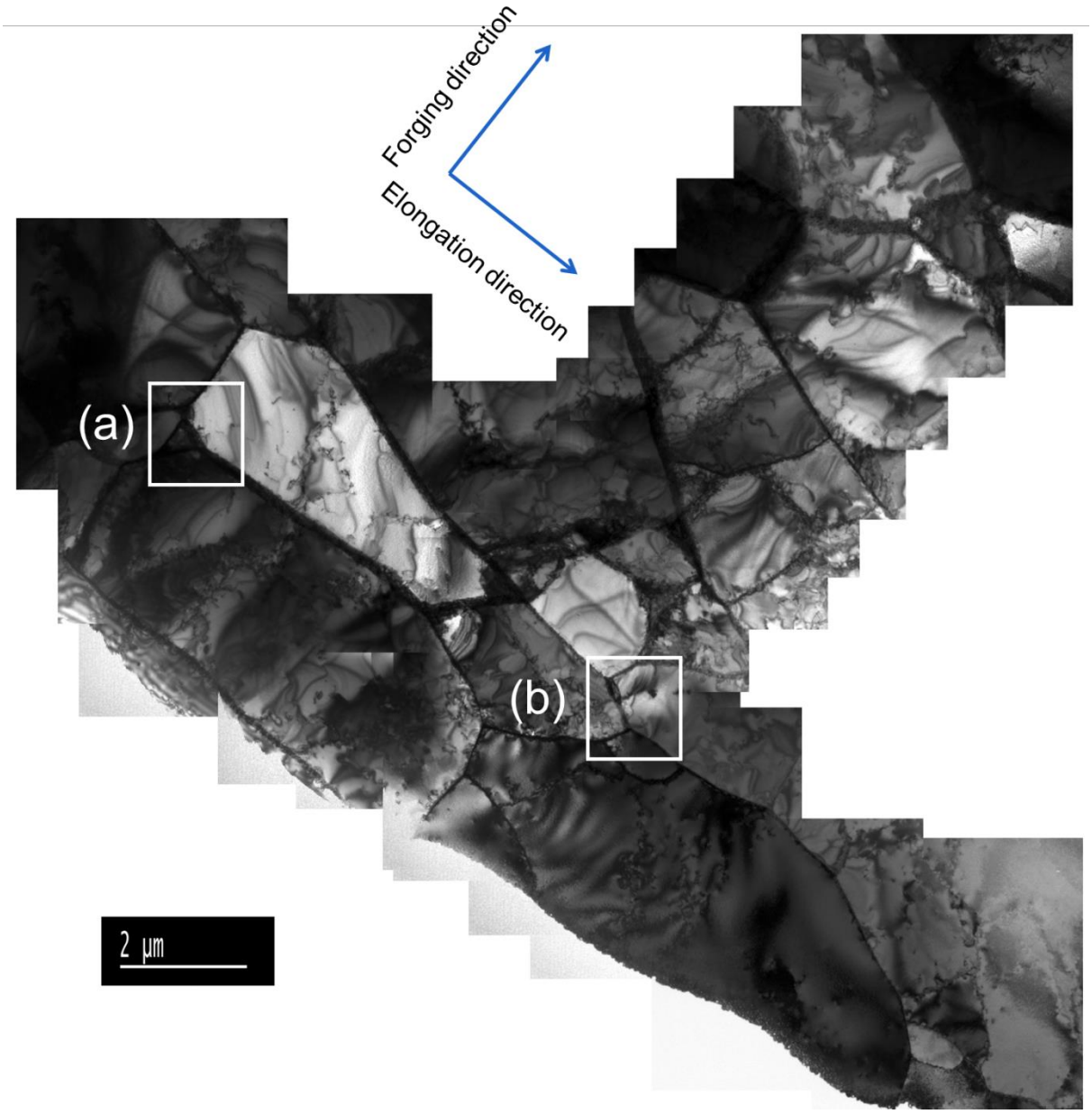

Fig. 3.2.15. Composite TEM image of the microstructure of IGP material deformed up to 9%. The sub-grains are elongated as noted by the forging direction.

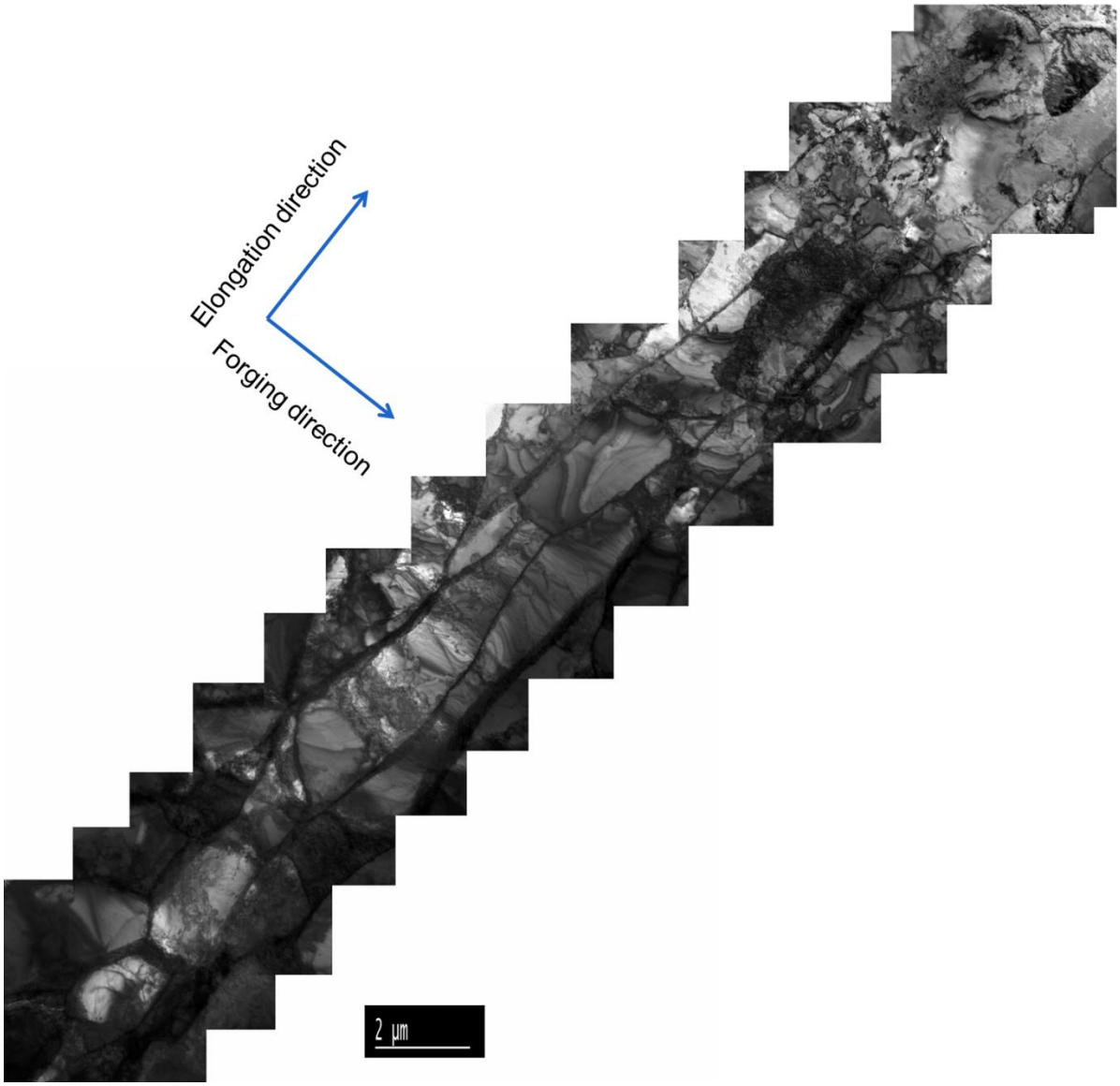

Fig. 3.2.16. Composite TEM image of the microstructure of IGP material deformed up to 22%. The sub-grains are elongated as noted by the forging direction.

In 4% deformed samples, the increase of the dislocation density is obvious. A closer look at the sub-grain boundary interfaces revealed that a significant accumulation of dislocations and formation of dislocation pile-ups took place there. An example of such evolution is presented in Fig. 3.2.17, where similar microstructural arrangements are compared in the reference and 4%-deformed materials. The broadening of sub-grain interfaces is evident in these figures as well as the formation of dislocation pile-ups near the low-angle grain boundaries. Here, by broadening we mean the formation of sub-structures observed as bended dislocation lines which are located nearby the grain-boundary interfaces (which were rigid in the non-deformed material). Apparently, such structures are formed under the action of the external stress and

being the signature of the presence of strain fields, see the examples of broadened grain boundaries in Fig.3.2.17.

Furthermore, there are many sub-grains where there is a high dislocation density and many sub-grains with the dislocation density comparable to the initial value, as illustrated for example in Fig. 3.2.18. This creates a large error bar associated with the mean dislocation density. The mean dislocation density grows up to $(3\pm2)\times10^{13}$ m^{-2}.

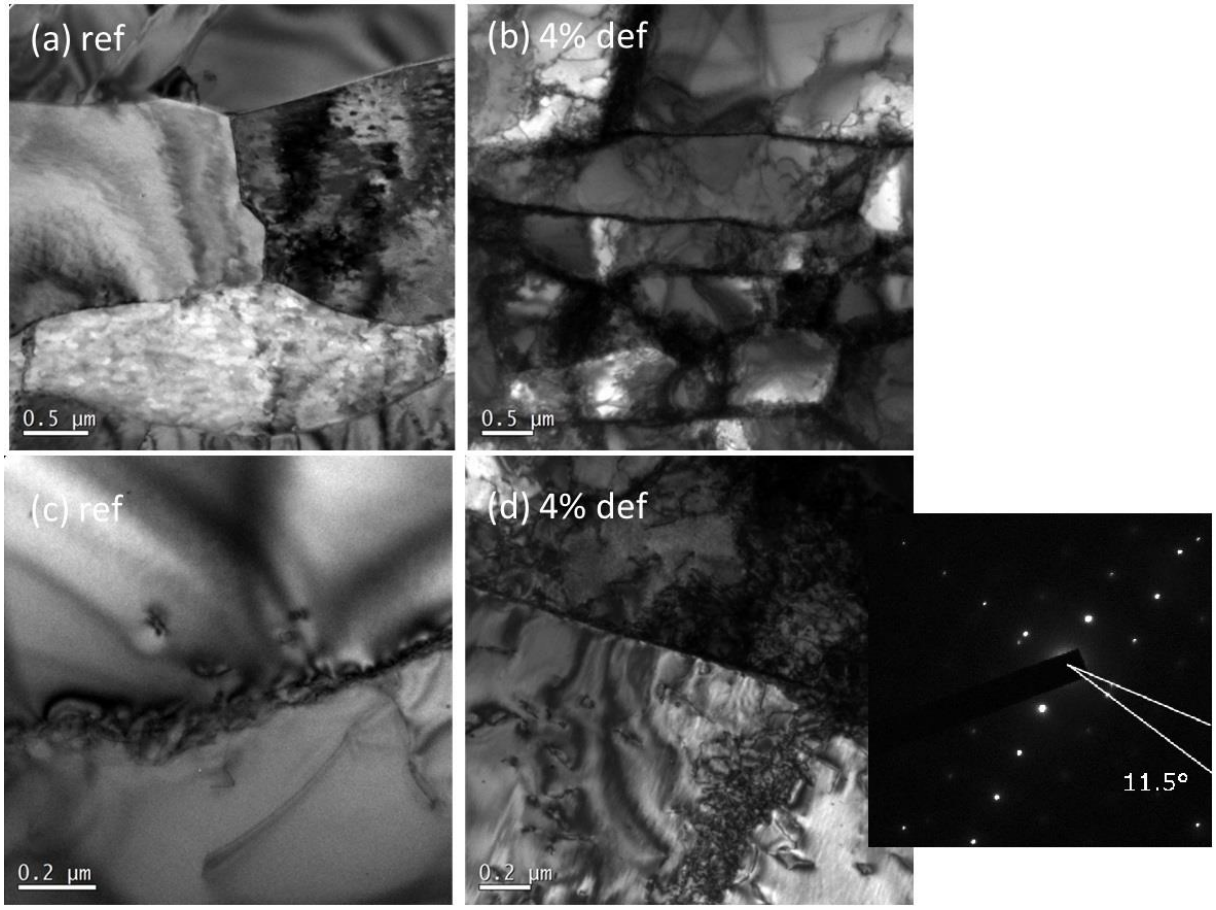

Fig. 3.2.17. Comparison of sub-grain microstructure in reference (a,c) and 4% deformed (b,d) samples, given as bright field images. Draw attention to the broadening of the sub-grain interfaces, as noted in the text. The inset figure next to (d) is a diffraction pattern corresponding to the grain boundary with misorientation angle of 11.5°.

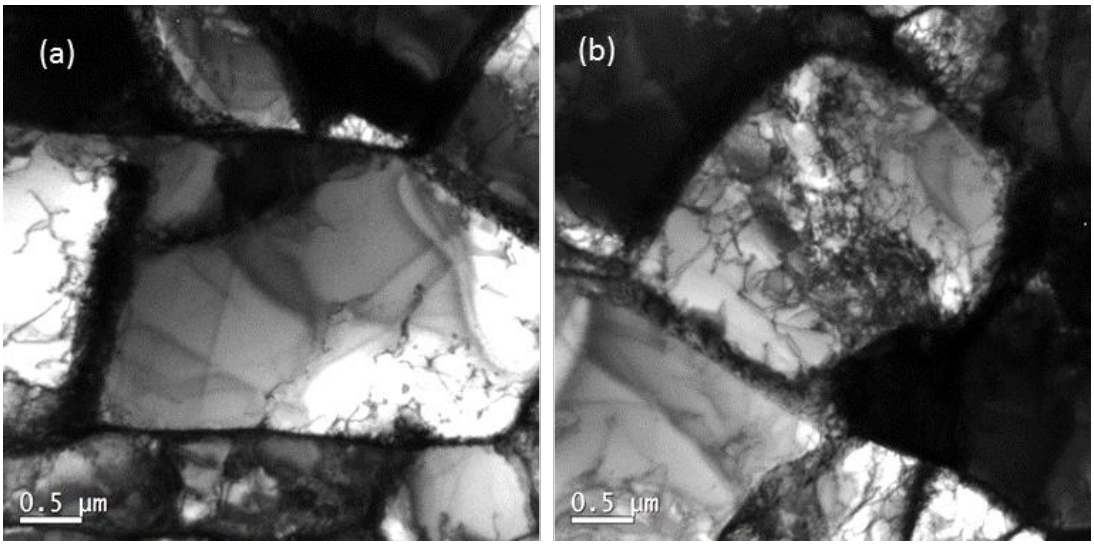

Fig. 3.2.18. Increase of the dislocation density induced by 4% deformation. Draw attention to the presence of sub-grains with strongly different dislocation density. Difference of the dislocation density on (a) and (b) is one order of magnitude.

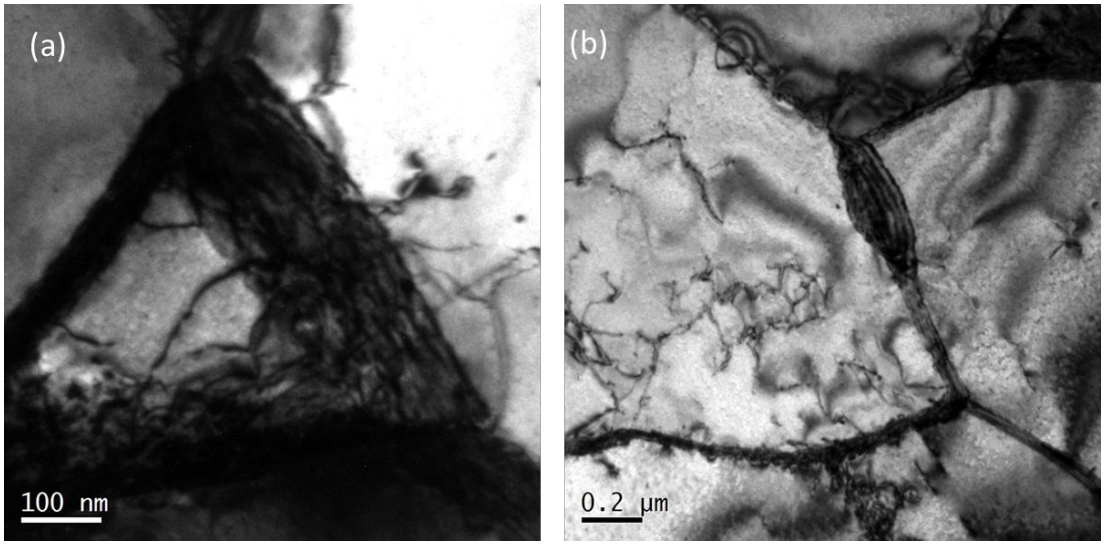

Fig. 3.2.19. Modification of the sub-grain boundary structures induced by 9% deformation. (a) and (b) show the spread of the sub-grain boundary interfaces.

In the 9% deformed sample, there is no visible increase of the dislocation density as compared to the 4% deformed material. The plastic deformation is mainly carried by dislocation slip and multiplication near the grain boundary interfaces. Fig. 3.2.19 shows enlargements of the two zones marked in Fig. 3.2.15 by 'a' and 'b'. These zones demonstrate regions close to the triple junctions. The reader's attention is drawn to the spread of the sub-grain boundary interfaces (broadening), which start to acquire a band-like structure with a width of 100-200 nm. Locally, the dislocation density can be

very high and easily reach 10^{15} m^{-2}. These are apparently the regions with the highest internal stress-state.

At 22%, the highest strain level investigated here, dislocation tangles start to grow out of the grain boundary interfaces and spread inwards towards the bulk. A closer view of such modified sub-grain boundaries is presented in Fig. 3.2.20. It can be interpreted as that all the grain interior dislocation sources are blocked and dislocation multiplication occurs by the emission of new dislocations from the grain boundaries. It seems that movement/expansion of dislocation tangles is the prevailing mechanism for plastic deformation at this stage. For some sub-grains, one can clearly see well-defined borders between dislocation-tangled regions and dislocation-free zones. An example of such microstructure is given in Fig. 3.2.21. Finally, we notice that some dislocation loops were also observed. We did not perform rigorous analysis of the loops, but expect the formation of shear loops as a result of dislocation-dislocation interaction. The presence of these loops in the as-deformed samples is shown in Fig. 3.2.22.

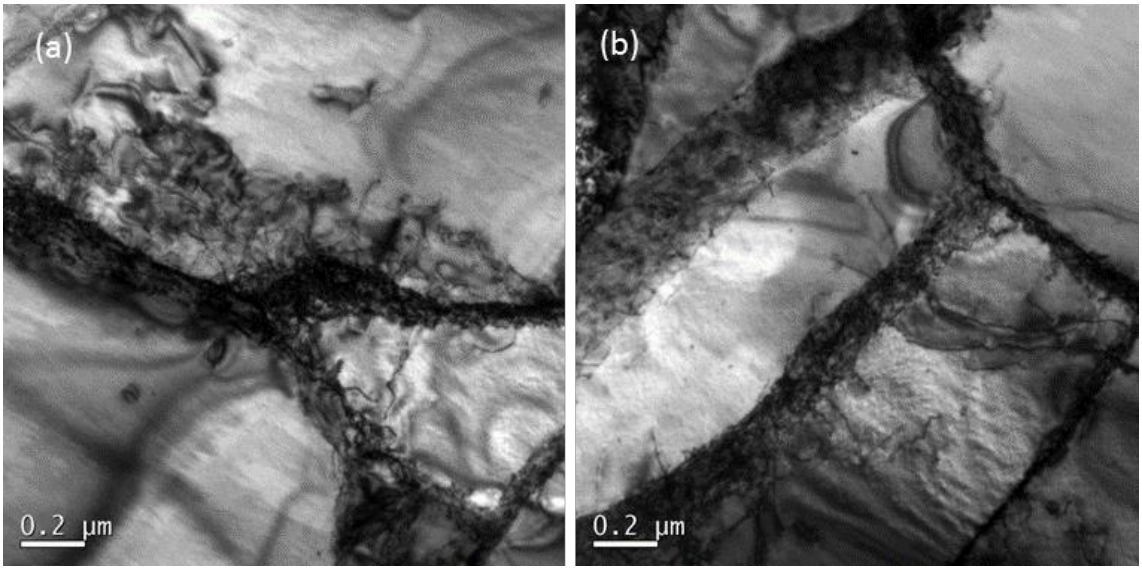

Fig. 3.2.20. Formation of the dislocation tangles near the sub-grain boundary interfaces observed in the 22%-deformed material. Pay attention to the local spread of the dislocation tangles away from sub-grain boundary interfaces. The central part of some sub-grains remains almost free of dislocations.

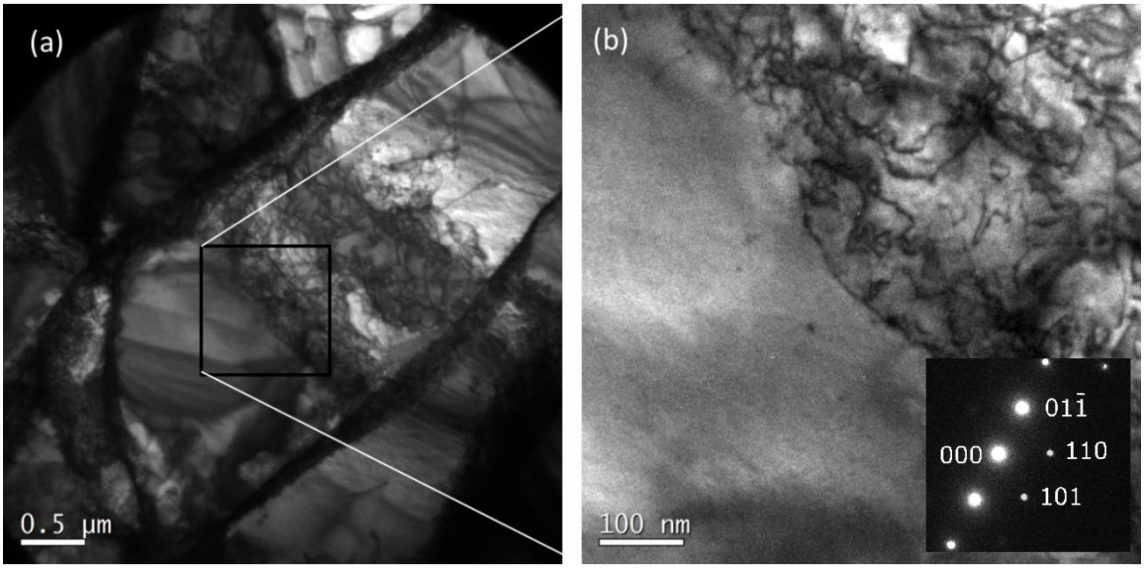

Fig. 3.2.21. Observation of the strong gradient of dislocation density in the 22%-deformed material. (a) dislocation tangles spreading from top to bottom of the middle sub-grain. (b) zoom-in of the region where the tangle meet dislocation free zone.

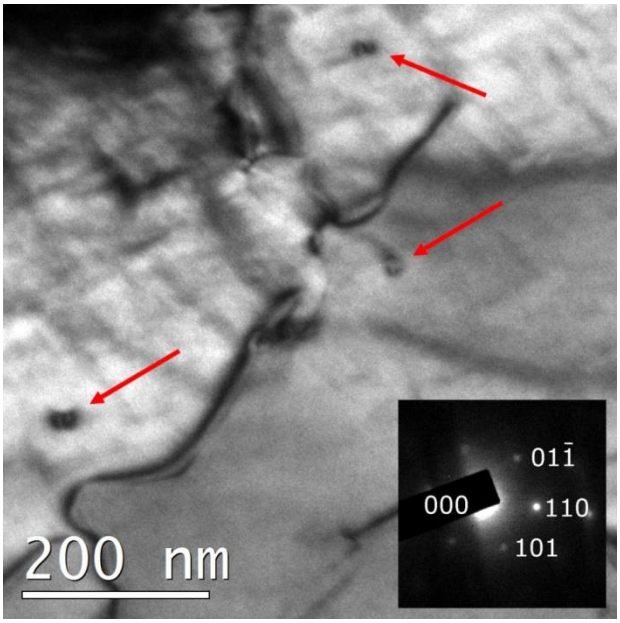

Fig. 3.2.22. Observation of the dislocation loops in 4% deformed IGP.

3.2.4 TEM investigation of the plastically deformed materials: IPP grade tungsten.

In this section we present a set of images and discuss the microstructural features of the IPP grade tungsten deformed at 600°C. This material does not have a texture and therefore the TEM images discussed below do not refer to the deformation axis, unlike the case with IGP grade.

Figs. 3.2.23-24 present composite TEM images of the microstructure obtained after 5% and 39% of deformation performed at 600°C. These measurements were taken in the range of the uniform elongation. The engineering stress applied was approximately 180 and 280 MPa, at respectively 5% and 39% deformation strain, while the yield stress is nearly 100 MPa.

Fig. 3.2.23 shows a composite TEM image of the microstructure of IPP grade tungsten deformed by 5%. The figure presents two entire grains surrounded by a few other grains which could not be captured completely. At 5% deformation, the grain interfaces begin to spread, which indicates that dislocations originate from the grain boundaries. Dislocation density increases by about a factor of two as compared to the non-deformed material, from 5×10^{12} m^{-2} to 1.15×10^{13} m^{-2}. Overall, the deformation induced microstructure is reminiscent of that observed in the 5% deformed DF_RX sample.

Fig.3.2.24 shows a composite TEM image of the microstructure of IPP material deformed by 39%. The figure shows several grains. The fact that more grains (with a smaller size) are found in the 39% deformed material clearly demonstrates that plastic deformation induced the grain refinement. Many newly formed grain interfaces are spaced by a distance of 100-500 nm, suggesting that extensive plastic deformation by dislocation tangling and transformation into dislocation walls indeed occurred within the pre-existing larger grains. An increase of dislocation density in the grain interiors is also evident. The measured dislocation density amounts to 2.05×10^{15} m^{-2}, which is twice as high as that seen in the 5% deformed material. Just as in the case of DR_RX and IGP, regions free of defects, and regions heavily populated by dislocation tangles and networks could be found in some of the grains. Thus, a strong heterogeneity in the distribution of dislocations seems to be a common feature for all of the samples subject to the load corresponding to the ultimate tensile strength.

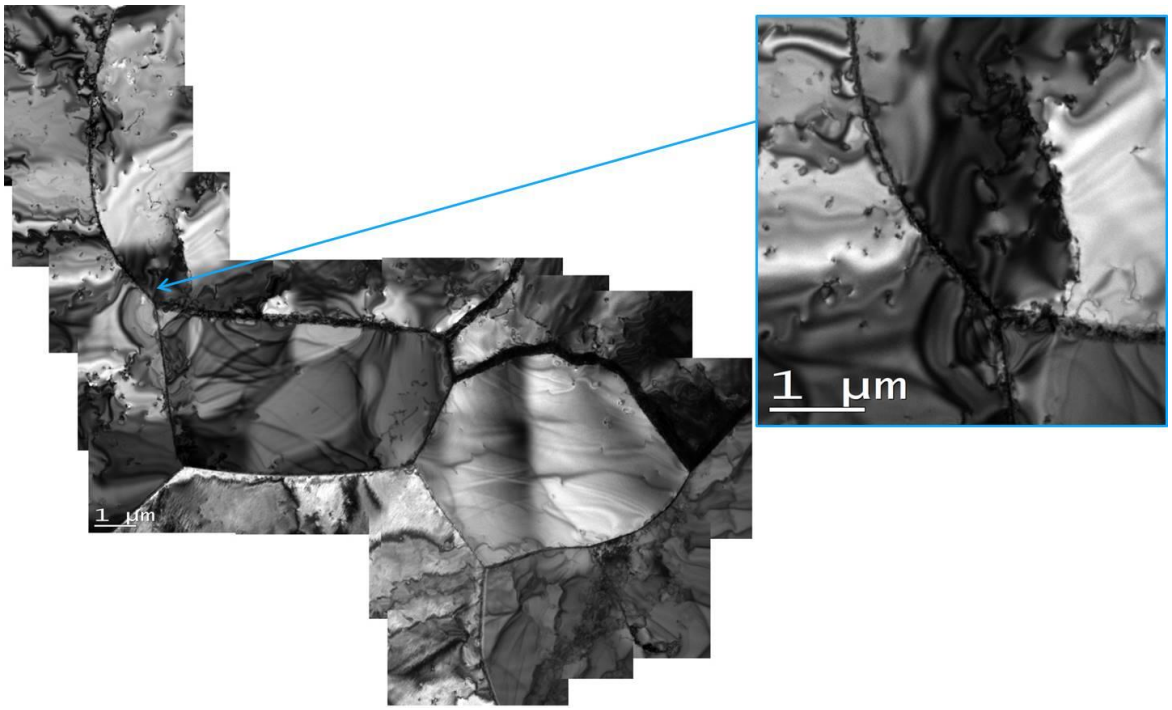

Fig. 3.2.23. Composite TEM image of the microstructure of IPP tungsten deformed up to 5%.

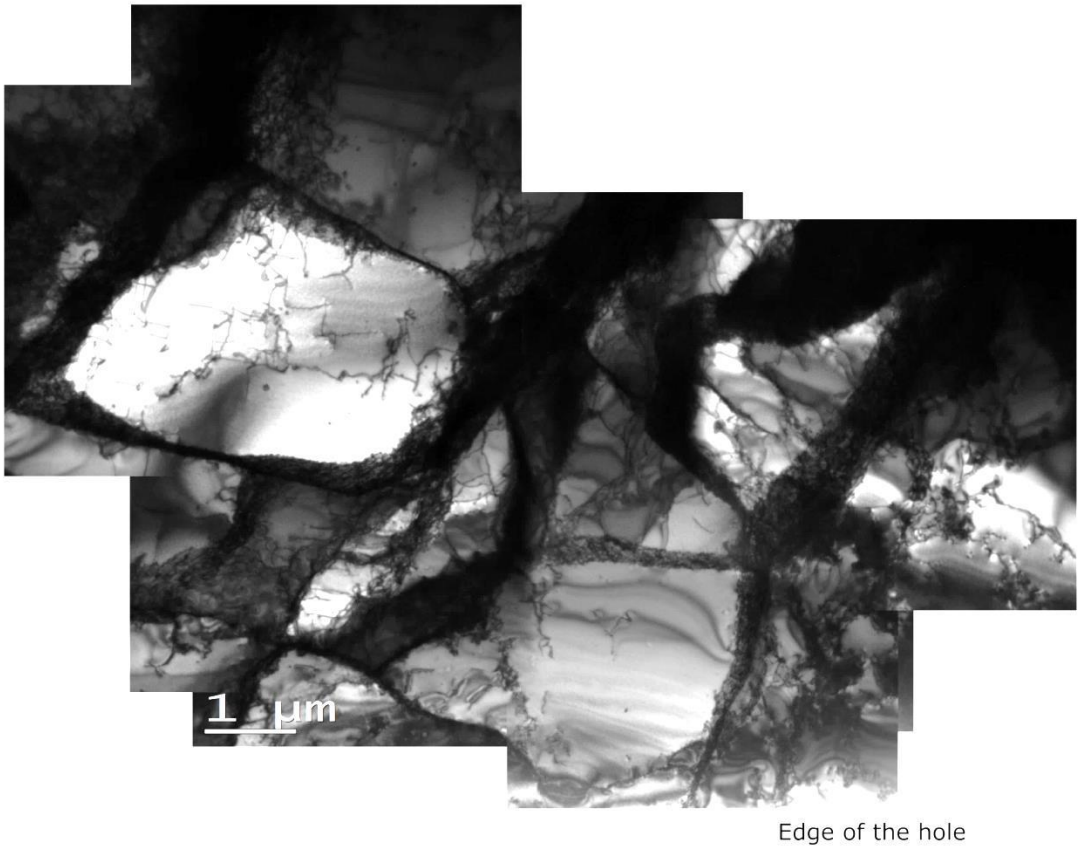

Fig. 3.2.24. Composite TEM image of the microstructure of IPP material deformed up to 39%.

3.2.5 Discussion of the results.

The evolution of the dislocation density vs. applied strain as measured by TEM in the three studied grades of tungsten is shown in Fig. 3.2.25. When we measured the dislocation density, our main concern was to study the evolution of this density in the grain interior. Therefore, regions containing dense dislocation pile-ups, and regions containing dislocation cells and walls were excluded from the examination. According to our understanding those regions appear to be precursors of the sub-grain walls, which are clearly seen in all deformed samples as soon as the applied strain exceeds about 10-20%.

From the Fig. 3.2.25 we can see that the dislocation density follows approximately a square root law. It is apparent that even at relatively high strain (i.e. from 20 to 40%), dislocation density keeps growing. However, growth rates in the deformation range 0-20% are much higher. This change of growth rates might be linked to the onset of grain refinement, which occurs in the 10-20% deformation region. The formation of secondary small grains, established by the arrangement of dislocations in cells and walls, would alter the process that controls the plastic deformation, and subsequently would change the growth rate.

Another point to be noted is the impact of the test temperature, which was examined for the IPP grade material. We can see that at high strain levels, close to the ultimate tensile strength, dislocation density is virtually for the same deformation at 300°C and 600°C. At 5% of the deformation strain, the dislocation multiplication rate is slightly higher at 300°C, which is logical since the dislocation-dislocation zip-unzip mechanism is a thermally activated process. Here, the zip-unzip mechanism implies the sequence of the formation of the mixed junction of <100> type (zip) made by the interaction of two ½<111> dislocations (moving in the two mutually inclined planes), bending of the two dislocations (being blocked by the immobile <100> junction) due to continuously applied load, and breakaway of the dislocation - achieved as soon as the critical stress to break the junction (unzip) is reached. The latter means that temperature assists in unzipping the crossed dislocations (which formed a junction binding them), such that the critical curvature (stress) required for this junction break-up is lower at higher temperatures. Correspondingly, the total increase of the dislocation length per unit of dislocation-dislocation interaction will also be lower at a higher test temperature. However, we must admit that increasing temperature from 300°C and 600°C (in the case of IPP grade) still has a minor effect on the dislocation multiplication, while the yield stress has decreased by nearly twice as much.

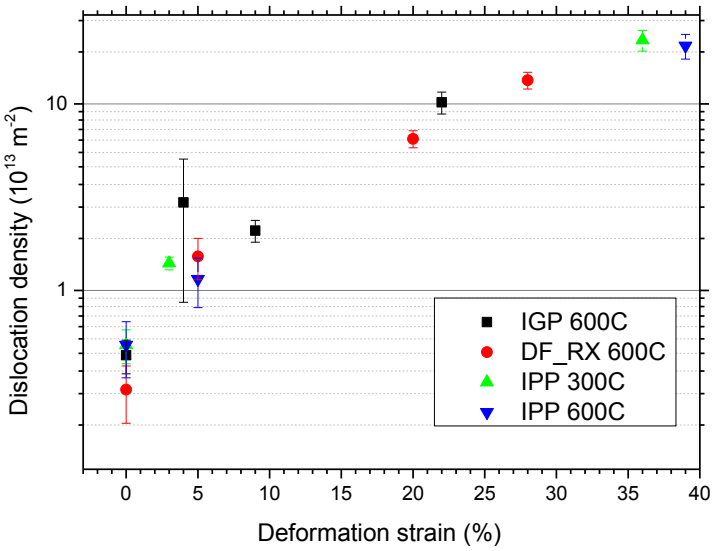

Fig. 3.2.25. Dislocation density as measured by TEM.

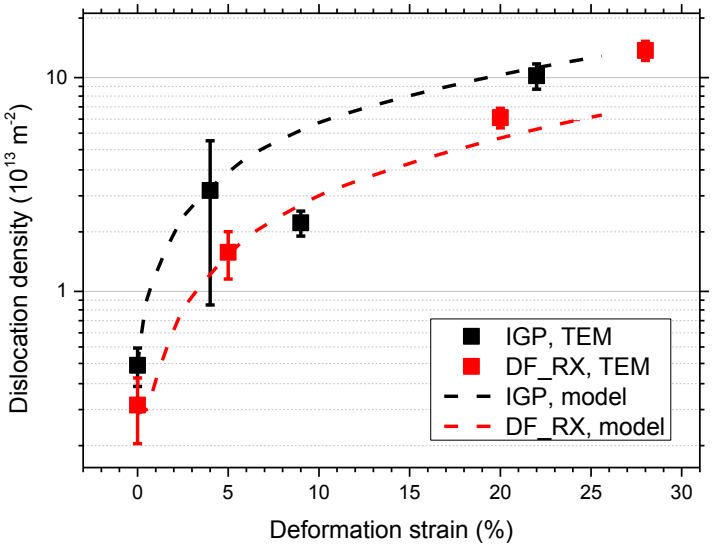

Fig. 3.2.26. Dislocation density, comparison of the experimental measurements and model of Mecking and Kocks [70].

There is a considerable interest in understanding how the dislocation density measured in the grain interior compares to well-established models describing dislocation evolution in metals. To analyse the evolution of the dislocation density as a function of applied strain, one can apply one of the most famous models, the one proposed by Mecking and Kocks in [70]:

$$\dot{\rho}(\varepsilon) = \dot{\varepsilon}\left(k_1\sqrt{\rho} - k_2(\dot{\varepsilon},T)\rho(T)\right) \tag{3.1}$$

The above expression basically describes two processes primarily governing the response of a crystalline material to external load and subsequent changes in dislocation density, used as an internal variable, and linking the damage induced inside the material to the applied work. The strain dependency of dislocation density (ρ) results from the multiplication term (the first one on the right-hand side of Eq. 3.1) and the removal term (the second one on the right-hand side of Eq. 3.1).

The multiplication of dislocation occurs as a result of self-pinning by means of the zip-unzip process and the formation of junction segments which is an energetically favourable process, leading to a reduction of the dislocation core strain energy. This latter process results in observations of the dislocation segments with the Burgers vector of a_o<100> type, which was formed by a junction of two $a_o/2$<111> pre-existing dislocation lines. Another reason for this dislocation multiplication is the formation of dislocation pile-ups and tangles near the microstructural defects, which act as non-transparent barriers, for example grain boundaries.

The removal of dislocations from the bulk polycrystalline tungsten is realized either by self-annihilation of dislocations with opposite signs, or due to the absorption of dislocations by grain boundary interfaces. The latter represents a mechanism where a dislocation pile-up, formed in a front of a grain boundary, results in either transmission of the piled dislocations into a neighbouring grain, or conversion of the bulk dislocations into grain boundary dislocations (also called disclinations or steps). The latter mechanism is generally responsible for the grain-boundary displacement and reshaping under external load.

The evolution of the dislocation density is thus defined by the balance of dislocation multiplication and recovery/storage. These two opposite processes are effectively parameterized by introducing coefficients dependent on temperature and strain rate: k_1 and k_2. Following Beyerlein and Tome [71], the mutual relationship between these two coefficients reads:

$$\frac{k_2(\dot{\varepsilon},T)}{k_1} = \frac{\chi \cdot b}{g}\left(1 - \frac{k_B T}{D b^3}\ln(\frac{\dot{\varepsilon}}{\dot{\varepsilon}_0})\right) \tag{3.2}$$

Here χ, g, D, $\dot{\varepsilon}_0$ and $\dot{\varepsilon}$ are respectively, the interaction parameter, the normalized activation energy, a proportionality constant, a reference and experimentally applied strain rate. The rationale behind the derivation of Eq. 3.2 is consideration of the steady-state deformation process described by Eq. 3.1 (i.e. complete or close to the saturation of the flow stress), where the rate of dislocation generation is equal to the rate of removal. The parameters applied are reported in Table 3.2.1, and are adopted without any change from the originally published data [72]. The experimentally used strain rate and initial dislocation density were used to calculate the evolution of the

dislocation density using Eq.3.1. This prediction of the model is superposed in Fig. 3.2.26 for two tungsten grades which have the highest and lowest initial dislocation density, respectively, IGP and DF_RX grades.

Table 3.2.1 Parameters for Mecking and Kocks model applied with the Beyerlein and Tome expression for the k_2/k_1 relationship.

Parameter	Definition	Value	Unit	Used in
k_B	Boltzmann constant	1.38×10^{-23}	J/K	Eq.(3.2)
b	Burger's vector length	2.74	Å	Eq.(3.2)
k_1	Kocks-Mecking parameter	[a]4.8×10^8	m^{-1}	Eq.(3.1)
χ	Interaction parameter	[b]0.9	-	Eq.(3.2)
g^{α}	Normalized activation energy	[b]2.8×10^3	-	Eq.(3.2)
D^{α}	Proportionality constant	[b]10^4	Pa	Eq.(3.2)
$\dot{\varepsilon}_0$	Reference strain rate	[b]10^7	s^{-1}	Eq.(3.2)

[a]REF [72]; [b]REF [71];

Before comparing the results predicted by the model with experimental ones, one should notice two important issues. First of all, the comparison is adequate strictly speaking for "bulk" dislocations and not for the dislocations forming pile-ups and cell walls. In those regions, the local dislocation density will be much higher because of the stress concentration. Naturally, the Mecking-Kocks model does not account for such heterogeneities, and that is why we focused on measuring the "bulk" dislocation density. Secondly, as we noted earlier the formation of cells and then new grains occurs as deformation strain reaches 20%, and this is also not accounted for by this simple model. Having this in mind, one can see from the Fig. 3.2.26 that the model works as expected in the case of DF_RX tungsten grade – the modeled graph corresponds well with the TEM measured values up to the deformation values of 10-

20%, and then gives lower results due to the reasons mentioned above. The IGP material, which contained higher initial dislocation density shows a higher rate of dislocation multiplication, but also faster saturation.

At this point, we can make an intermediate summary of the results obtained from TEM measurements done on three tungsten grades deformed at 300°C and 600°C up to their ultimate tensile strength. All studied grades have nearly the same purity, but were produced by different fabrication routes. Differences in terms of fabrication route and initial microstructure are described in Section 2.1 and Section 3.1, respectively. The principal difference between IGP and two other grades (IPP, DF_RX) was that IGP was not recrystallized and exhibited relatively high initial dislocation density with small elongated grains and texture, therefore had high ratio of the initial dislocation density to the grain size. While the two other grades had comparable initial dislocation density, grains were large and equiaxed.

TEM was used to investigate the necking region in tensile samples deformed up to the fracture strain. A few tests were interrupted to study samples at intermediate strains, so as to follow up the evolution of the microstructure. The resulting microstructure was characterized and compared between the three grades in terms of dislocation density, heterogeneity, observation of pile-ups and tangles specifically near high angle grain boundaries. The main microstructural features registered by the TEM inspection are summarized in Table 3.2.2, while the evolution of the dislocation density is presented in Fig. 3.2.25. The observed evolution of the dislocation density was compared with predictions of the previously developed thermo-mechanical model for the plastic deformation of polycrystalline tungsten and good agreement was found without any need to modify the original parameter set.

Based on the features of the plastically-induced microstructure measured in the recrystallized sample, it can be concluded that at both 300°C and 600°C the initial contribution to plastic deformation comes from the multiplication of dislocations inside grains. The next stage is the formation of the pile-ups in a front of high angle grain boundaries, and finally transformation of these pile-ups into cells, resulting in grain refinement. Such a sequence of the plastic deformation mechanisms, in the case of deformation of the recrystallized material, ensures significant capacity for work-hardening and therefore the material exhibits large uniform elongation. However, the recrystallized material has a very important drawback – very much lower yield strength, hence it has potentially very high susceptibility to thermal cycle fatigue.

Table 3.2.2. Features of microstructure induced by the plastic deformation.

	DF_RX	IPP	IGP	Comment
Initial dislocation density, m^{-2}	2.8×10^{12}	5×10^{12}	4.5×10^{12}	Strong heterogeneous distribution of dislocations in IGP
Initial grain (EBSD)/sub-grain (TEM) size, μm	50-150 / 1.5	10-20 / -	50-150 (forging direction), 10-30 (normal to forging) / 0,6-1,7 (forging direction), 2.3-4 (normal to forging)	IGP has elongated grains
Yield stress (proof stress at 0.2%), MPa	102	98	470	
UTS (engineering), MPa	250	280	500	UTS in DFR is achieved at about 25-30%, UTS in IGP is achieved around 0.5-1 %
Dislocation density at UTS (engineering), m^{-2}	1×10^{14}	2×10^{14}	4×10^{12} - 3×10^{13}	Homogenous distribution in DFR, heterogeneous in IGP
Special features of microstructure at UTS	Many dense dislocation pile-ups in a front of large angle grain boundaries. Grain refinement.		Strong heterogeneous distribution of dislocation tangles within sub-grains.	

In the case of the non-recrystallized IGP grade, with much higher yield strength, the strain hardening capacity is very small, because of the high ratio of initial dislocation density to grain size. Due to the small grain size, the major contribution to the flow stress is due to the Hall-Petch mechanism [60]. The yield stress of the IGP at 600°C is 470 MPa i.e. more than four times higher when compared to the recrystallized material (~100 MPa). Because of the high yield stress, the ultimate tensile strength (500 MPa) is reached shortly after the yield point and diffuse necking emerges at the strain of

several percent. However, this post-necking deformation continues up to about 22% with the localized neck emerging around 20%. TEM studies performed in the region of diffuse and localized necks reveal that the dislocation density exhibits a steady increase with the accumulated strain. However, contrary to the recrystallized sample, the dislocation density was increased by the formation of bands (called here "broadening") of the low angle grain boundaries in the range of 4-9% of strain. At larger strains, this deformation occurred by the emission of the dislocations from the grain boundary interfaces, resulting in the formation of dislocation tangles spreading from the grain boundary towards dislocation-free grains. The expansion of the dislocation tangles basically controlled the plastic deformation level and accommodation of the elongated grains to the applied load. This is likely to be the principal difference in the mechanisms controlling plastic deformation of recrystallized and as-fabricated tungsten materials at 600°C in the region of plastic strains exceeding 10%. This important discussion will be referred to further on, when results for the plasma-exposed samples are presented.

3.3 Microstructure of the plasma exposed samples.

In this section the results of TEM investigation of the plasma exposed samples are presented. The plasma exposures were performed using pure D plasma in the temperature range of 470-620 K and fluence of 5×10^{25} D/m^2. The fluence was achieved in one pulse of 70 s duration. The flux was 7×10^{23} D/m^2/s. More information on the details of the plasma exposure is provided in Section 2.3.2. The primary purpose of this study was investigation of the relationship between the initial microstructure and trapping of plasma components. TEM analysis was seen as a key point study to support the regular measurements done by thermal desorption spectroscopy and nuclear reaction analysis, especially to clarify the types of the microstructural defects that plasma induces. Overall, five types of samples were exposed and investigated in-depth by TEM. Rear-face electro-chemical polishing technique was utilized to study the microstructure at different depths from the plasma exposed surface. The results in this section are organized and presented in the following order: firstly, we show the plasma-induced microstructure in the baseline tungsten grade – IGP material; then, we demonstrate the impact of plasma damage in the recrystallized tungsten i.e. in DF_RX; in particular, we study the microstructure of the exposed DR_RX in both reference and heavily-deformed states; finally, we describe the plasma-damage in single crystal tungsten.

3.3.1 Plasma exposure of the reference tungsten grade at 470 K.

The initial microstructure of the IGP grade (which is baseline ITER specification grade) exposed at 470 K using the Pilot PSI device is presented in this section. As mentioned earlier, measurements performed in the as-received material revealed the average dislocation density to be (4-8)×10^{12} m^{-2}, depending on particular sub-grains, and is 4.5×10^{12} m^{-2} on average. TEM observations showed that dislocation segments are nearly ubiquitously present within sub-grain interiors. No dislocation networks or pile-ups were observed, proving that the material is stress-relieved.

Importantly, to provide an adequate comparison between the bulk and surface microstructure, the TEM examination was performed using rear-face electrochemical polishing for both reference and as-exposed samples, and this approach was also adopted for further measurements. The top surface of the as-received sample was mirror-polished before the plasma exposure and no further polishing on the exposed surface was applied to avoid any post-exposure damage. The reference sample was characterized using exactly the same procedure. All TEM specimens that were used for investigation of the plasma exposure influence on the microstructure were prepared so as to study the surface in a plane normal to the plasma beam.

TEM observations, made in the immediate implantation region, i.e. at a depth of 100-150 nm, showed a significant increase in dislocation density, as shown in Fig. 3.3.1. The computed dislocation density was found to be one order of magnitude higher in the first sub-surface region (6×10^{13} m^{-2}) of the exposed sample as compared to that observed in the bulk i.e. (4-8)×10^{12} m^{-2}. Statistical analysis was performed by measuring the dislocation density in 15-20 different sub-grains, showing that the standard error does not exceed 25% of the absolute value.

In addition to the dislocation lines and tangles, shown in Fig. 3.3.2 (a), a pattern of elongated sub-grains is clearly seen, which means that the grain structure was not affected by the plasma exposure. The interface of sub-grains, seen to appear in a sharp contrast in the reference sample, has become broadened after the plasma exposure, see Fig. 3.3.2 (b). We interpret this to mean that the impact of thermal stress has disturbed the original arrangement of dislocation walls which form the interface of the low angle grain boundaries.

To investigate the microstructure in the deeper sub-surface region, rear-face electrochemical polishing was applied to preserve the exposed surface. This was followed by consecutive electrochemical polishing from both sides for 4, 5, 10, 15 and 23 seconds, removing approximately 3, 7, 10 and 15 μm of the exposed surface layer.

The typical appearance of dislocations at the studied depths is shown by a set of pictures in Fig. 3.3.3. The calculated dislocation density and the error bar are presented

in Fig. 3.3.4. The origin of the variation of dislocation density is related to certain inhomogeneity of the spatial distribution of dislocations inside any one grain, as well as between different grains. Evidently dislocation density decreases as the surface region is removed, reaching the value found in the unexposed sample at about 15 μm below the exposed surface.

While inspecting the dislocation microstructure, dislocation loops with "coffee bean" and "dot-like" contrasts were also regularly observed within 10 μm depth. Similar loops were observed in further experiments. These defects will be discussed further in this chapter.

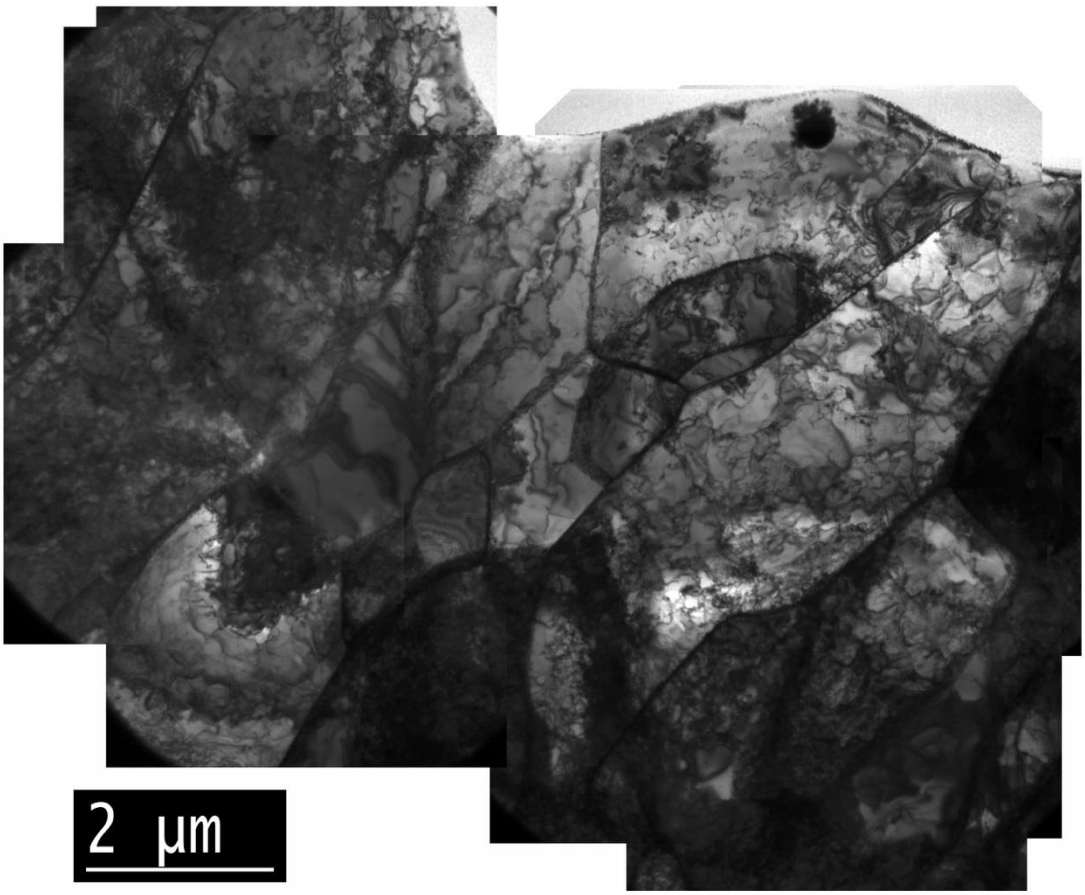

Fig. 3.3.1. Composite TEM image of the surface layer of the exposed IGP sample. Around ten sub-grains can be observed.

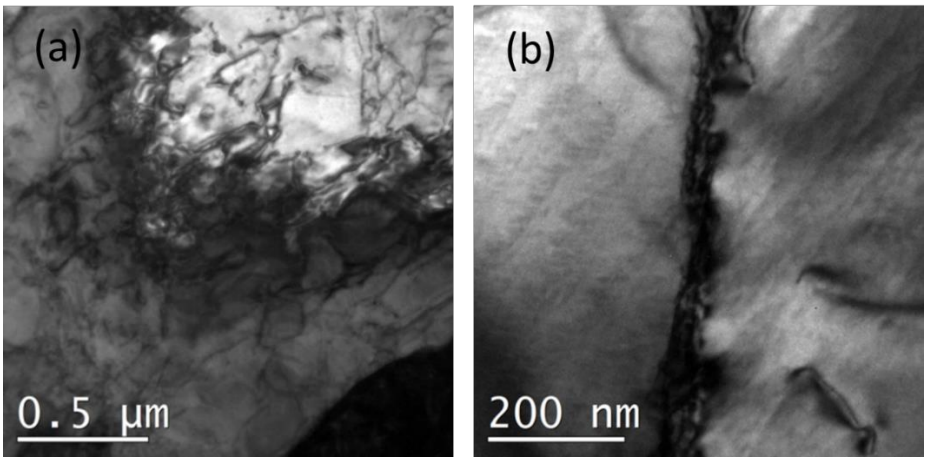

Fig. 3.3.2. Particular features of the surface microstructure, namely (a) Example of dislocation tangles identified within a sub-grain; (b) Example of a low-angle grain boundary which is broadened as a result of the exposure. Note that the grain boundary broadening after plasma exposure is reminiscent of that after the heavy plastic deformation.

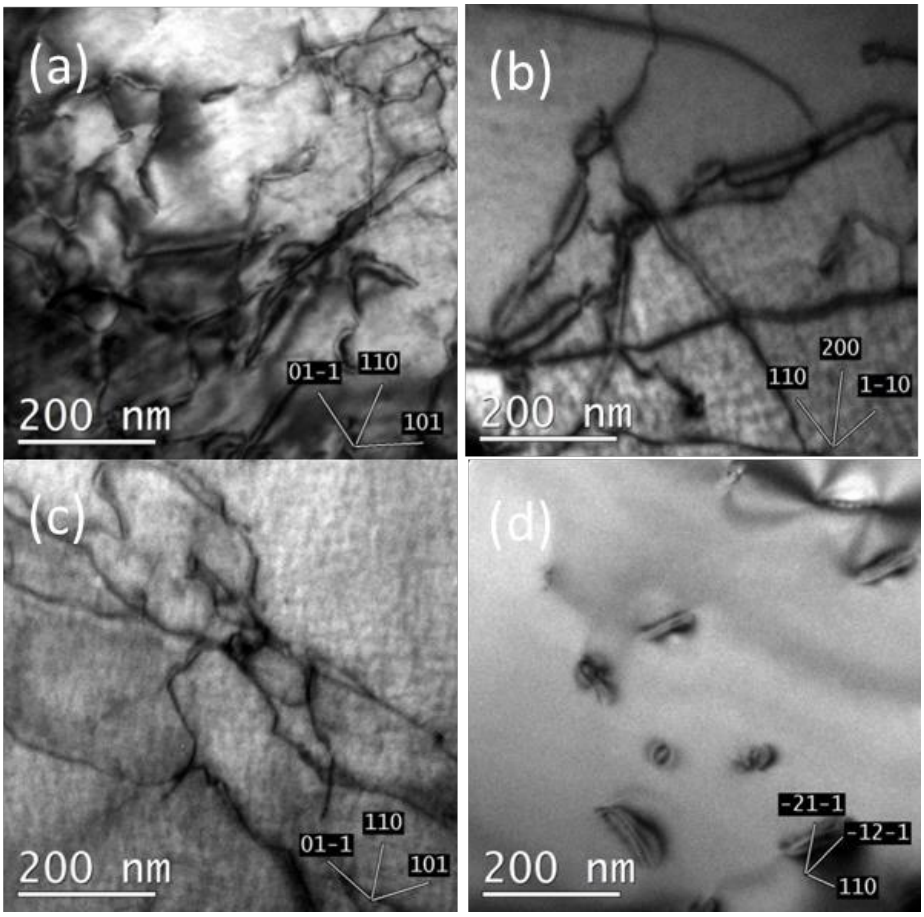

Fig. 3.3.3. TEM images used to measure the dislocation density following the removal of the exposed surface: (a) 3 μm removed, (b) 7 μm removed, (c) 10 μm removed and (d) 15 μm removed.

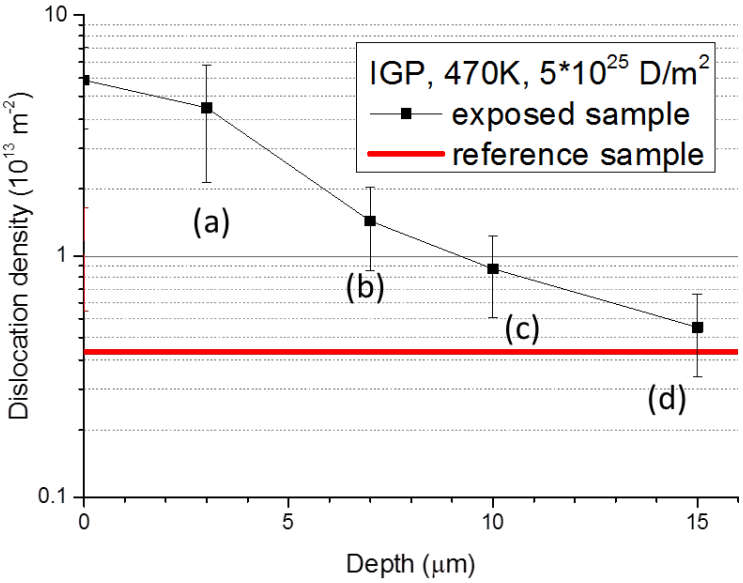

Fig. 3.3.4. Average dislocation density as a function of depth from the exposed surface. The red line corresponds to the mean dislocation density measured in the reference un-exposed sample.

3.3.2 Plasma exposure of the recrystallized tungsten grade at 570 K.

Plasma exposure applied to the recrystallized tungsten grade (noted as DF_RX) was also done at the Pilot-PSI device. The exposure fluence and flux were exactly the same as for the reference IGP material, but the surface temperature was 100 K higher (unfortunately the temperature control is technically complicated at this ultra-high flux device). The type of analysis that was applied to this sample was exactly the same as in the case of IGP sample.

The initial microstructure in terms of dislocation density and grain size was characterized by TEM and EBSD techniques, as presented earlier in Section 3.1. In the non-exposed sample the dislocation density was (2-8)×10^{12} m^{-2}. The grain size was mostly between 50-150 μm.

TEM observations of the surface layer show a significant increase in the dislocation density and pronounced in-homogeneous spatial distribution, as well as the presence of dense dislocation networks. See micrograph in Fig. 3.3.5 (a) and (b) for the DF_RX which is similar to that observed for the IGP.

The computed surface layer dislocation density was found to be higher by more than a factor of two compared with dislocation density in the bulk. In some regions, the dislocation density in tangles and networks reached 10^{15} m^{-2}. However, the area of those regions was rather small (typically 0.3×0.3 μm) as compared to the sub-grain size. Therefore, we have not included this estimated figure in the statistical analysis. Unlike what is seen in the non-exposed sample, the formation of dislocation tangles and pile-ups is no longer correlated with the presence of nearby sub-grains. It is also worth mentioning that after plasma exposure, the increase of the dislocation density was not uniform from one sub-grain to another. An example of the two neighbouring sub-grains with relatively low and high dislocation density is shown, in Figures. 3.3.5 (c) and (d) respectively. The measured dislocation density is reported in the figure captions. Note that the dislocation density between the two sub-grains shown differs by almost one order of magnitude.

Rear-face electrochemical polishing was applied to preserve the exposed surface. This was then followed by consecutive polishing from both sides for 2, 5 and 10 seconds which removes approximately 2.5, 7 and 12 μm of the exposed surface layer. The typical appearance of dislocations at different depths is shown in Fig. 3.3.6.

Because of the initial recrystallization, for the DF_RX sample we could perform a more detailed analysis to clarify possible correlations between the dislocation microstructure induced by plasma exposure and grain orientation. Based on the primary analysis of the orientation of the grains, several of the most-frequent orientations have been selected, namely: (113), (001) and (011). Fig. 3.3.7 shows an example of the dislocation patterns in these grains and Table 3.3.1 reports the average dislocation density and its variation (i.e. min-max). Overall, one can conclude that there is no strong difference in the dislocation density of the grains with different surface orientation in the plasma exposed reference polycrystalline tungsten.

Using data from the TEM micrographs, the dislocation density was calculated and is presented as a function of depth in Fig. 3.3.8. Due to variations in the dislocation density from one region to another, we show the standard error in addition to the mean value. The causes of this variation in dislocation density are related to the distribution of grain size as well as to the crystallographic orientation of the grains relative to the plasma beam. It is indeed known that <111> grains are more susceptible to surface damage (see e.g. [45]). Fig.3.3.8 reveals that in DF_RX samples dislocation density decreases as the surface layer is removed in a similar way to that seen in the IGP samples, reaching the reference value at a depth of 12.5-15 μm beneath the exposed surface.

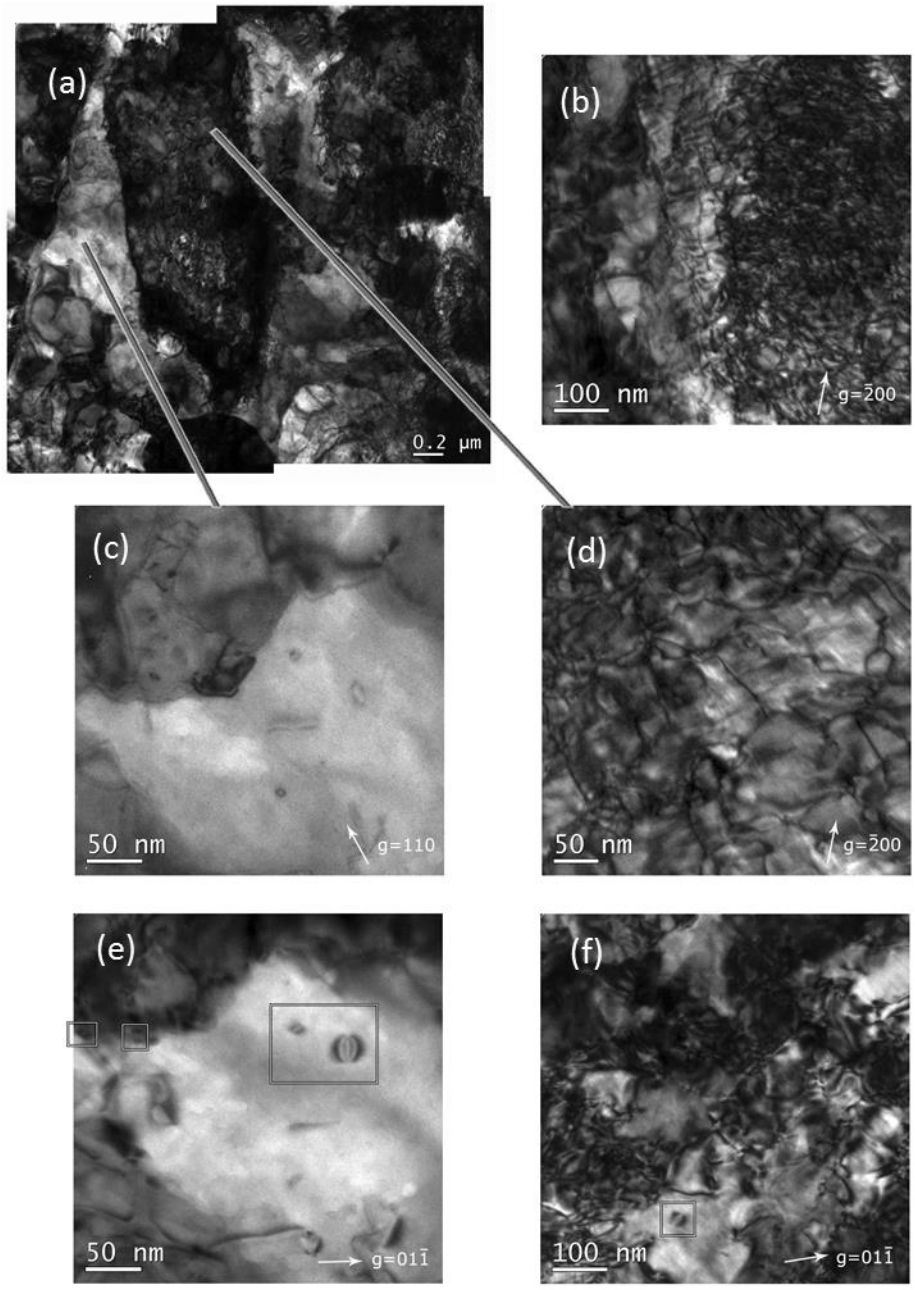

Fig. 3.3.5. TEM micrographs of DF_RX tungsten grade after plasma exposure showing the microstructure of the rear-face polished sample: (a) top surface; (b) higher magnification of the top surface to demonstrate the presence of dislocation tangles; (c) and (d) higher magnification of two neighboring sub-grains with a strong difference in dislocation density, namely (c) 4×10^{13} m^{-2} and (d) 1.5×10^{14} m^{-2}; (e) and (f) show the presence of dislocation loops with a typical "coffee-bean" pattern.

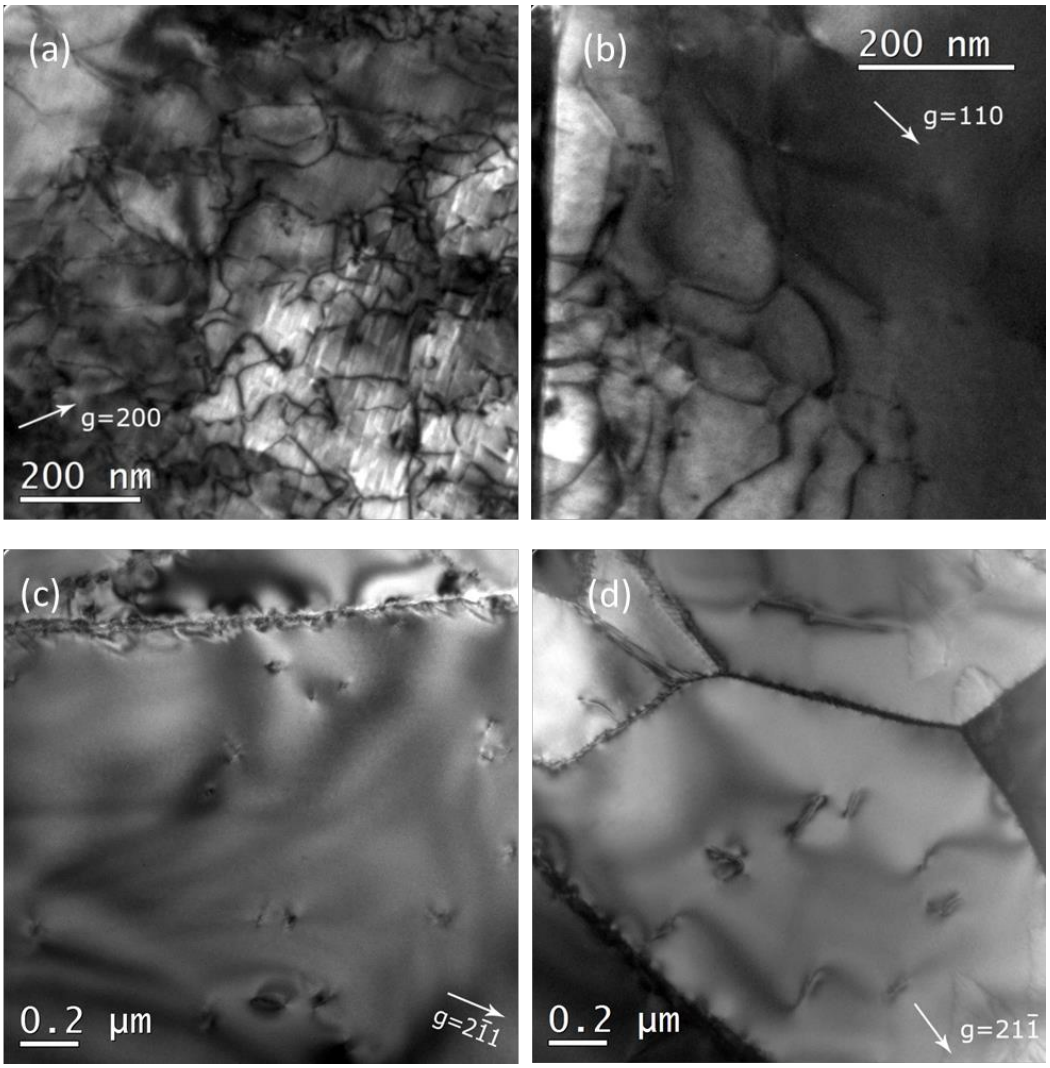

Fig. 3.3.6. TEM micrographs of DF_RX specimen after plasma exposure showing changes in dislocation density when flash electro-chemical polishing is applied for different time periods to remove: (a) 2.5 µm, (b) 7 µm and (c) 12 µm. A TEM image of unexposed tungsten is presented in (d).

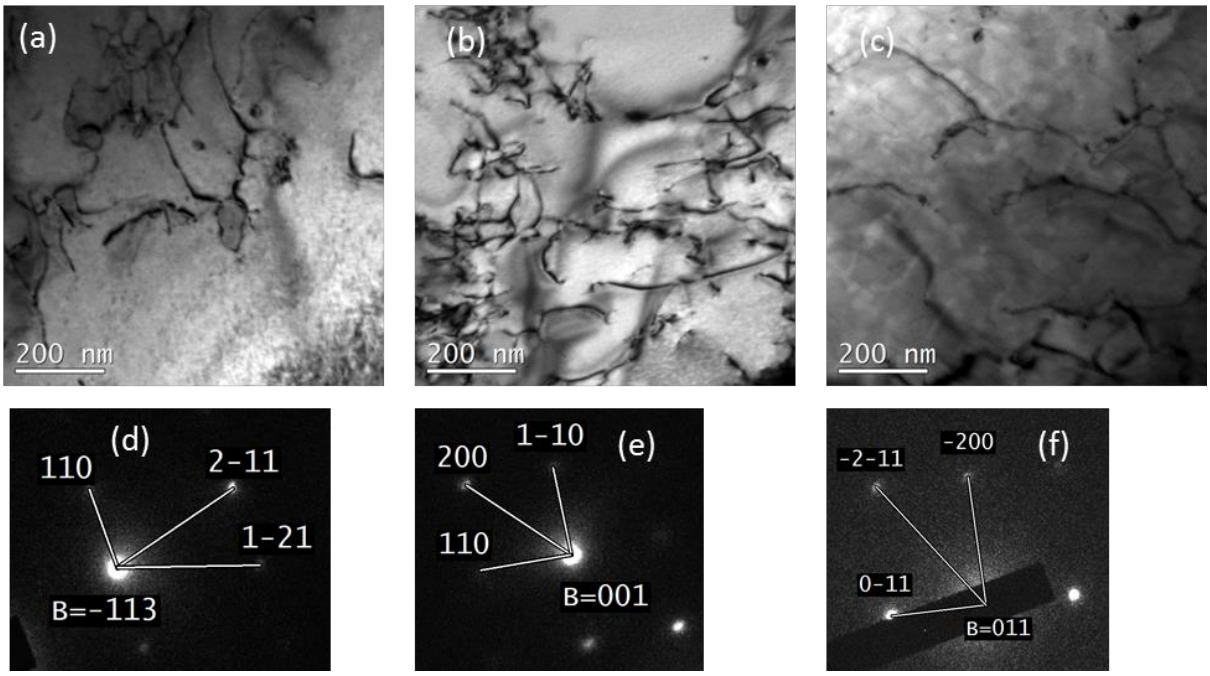

Fig. 3.3.7. TEM micrographs of the top surface of DF_RX material after plasma exposure. Figs. (a-c) show the dislocation pattern in grains with orientation of (113), (001) and (011), respectively. Figures below, labeled as (d-f), demonstrate the diffraction pattern.

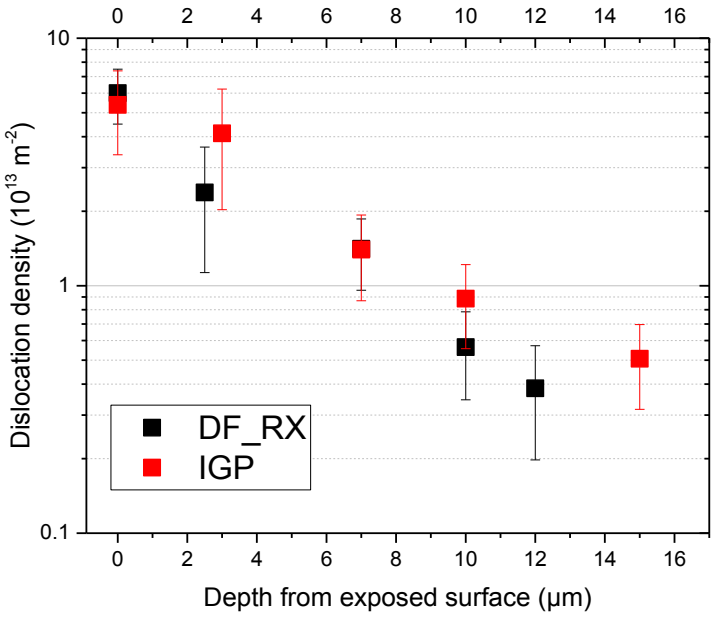

Fig. 3.3.8. Average dislocation density measured in DF_RX and IGP grades as a function of the distance from the exposed surface.

Table 3.3.1. Dislocation density measured in grains with different orientations for which the TEM images are presented in Fig.3.3.7. Data for the most frequent orientations of the sub-grains is reported.

Normal to the surface	Avg. dislocation density, m^{-2}	Range of variation of dislocation density, m^{-2}
113	7.4×10^{13}	$(5.7\text{-}9.5)\times10^{13}$
001	8.9×10^{13}	$(5.3\text{-}13.4)\times10^{13}$
011	5.3×10^{13}	$(3.7\text{-}7)\times10^{13}$
Averaged over the whole area observed	6.0×10^{13}	

3.3.3 Plasma exposure of the recrystallized tungsten grade after heavy plastic deformation at 620 K.

This section describes the result of plasma exposure applied to the DF_RX material that was modified by heavy plastic deformation. The exposure was performed at Pilot-PSI device applying the same conditions described for the DF_RX samples presented in the previous section.

As reported in section 3.1, measurements performed in the deformed material revealed the dislocation density to be in the range of $(5\text{-}7)\times10^{13}$ m^{-2}. The grain size was about 50-150 μm i.e. the same as in the non-deformed material. TEM observations showed the presence of dislocation lines to be almost ubiquitous in grain interiors. However, near grain boundary interfaces, dislocation pile-ups were regularly observed. The refinement of sub-grains was also observed.

In plasma exposed sample TEM observations made in the immediate sub-surface region, see Fig. 3.3.9, showed a significant increase in dislocation density, presence of dislocation networks and strongly un-homogeneous spatial distribution of these defects. The computed dislocation density was found to be more than a factor of two higher in the upper surface region when compared to the bulk dislocation density. In some regions, the dislocation density in tangles and networks was seen to reach 10^{15} m^{-2} or even higher. Such a strong increase in dislocation density corresponds to about 30-40% of plastic deformation, as one could predict based on the analysis made in Section 3.2. However, the area of those regions was rather small (typically 0.3×0.3 μm) when compared to the sub-grain size, therefore this estimate is not included in the statistical analysis. Unlike our observations of the non-exposed sample, the formation of

dislocation tangles and pile-ups was no longer correlated with the presence of nearby sub-grains.

The evolution of the microstructure is dependent upon distance from the top of the exposed surface as shown in Fig. 3.3.10. The microstructure was studied at the depth of 2.5, 5 and 12.5 μm. One can see that the dislocation pattern changes from dense tangles to networks, and finally to isolated dislocation lines. The calculated dislocation density is presented in Fig. 3.3.11. It shows that dislocation density decreases linearly with depth, reaching the reference value (i.e. the same as the dislocation density in bulk) at a depth of 12.5 μm. As in previous cases, we provide an error bar for the mean value, which is considerable, because of the variation of dislocation density between sub-grains.

Dislocation loops with "coffee bean" and "dot-like" contrasts were also regularly observed when we inspected the microstructure within a depth of 6 μm, as shown in Fig. 3.3.10 (e) and (f). The size of the dislocation loops varied in the range of 10-35 nm, and their density could be estimated to be 10^{19} m^{-3}. Identification of the Burgers vectors showed that both $a_0/2\langle 111\rangle$ and $a_0\langle 100\rangle$ loops were present. The g•b analysis revealed that these loops were of the edge type and interstitial in nature. Note that earlier we also observed similar loops in the DF_RX and IGP plasma exposed samples.

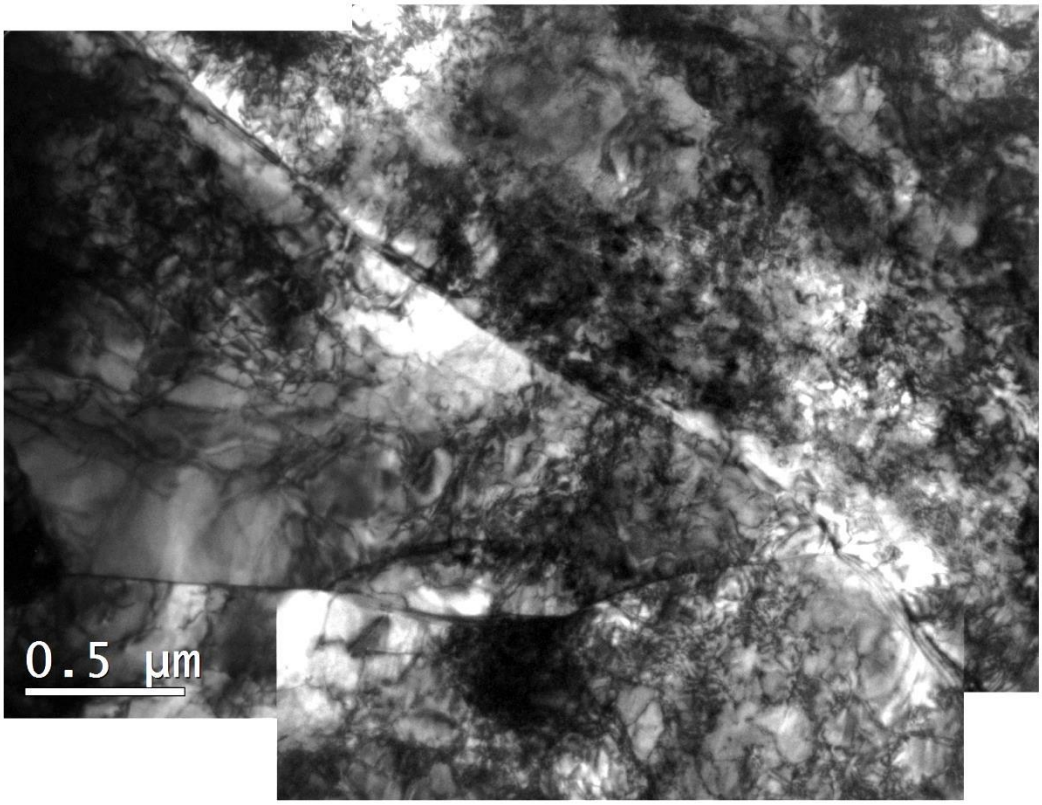

Fig. 3.3.9. Composite TEM image of the surface microstructure of the plasma exposed DF_RX 20% deformed sample.

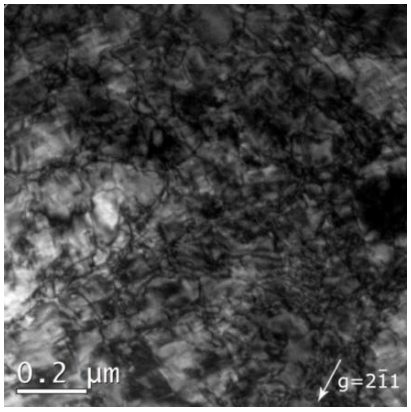

a)

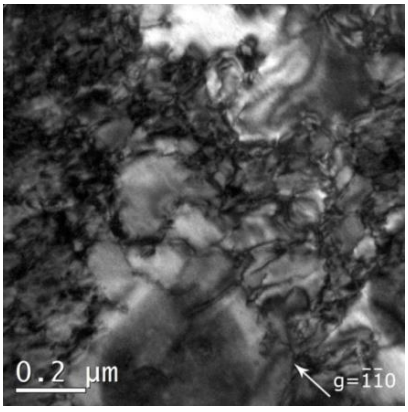

b)

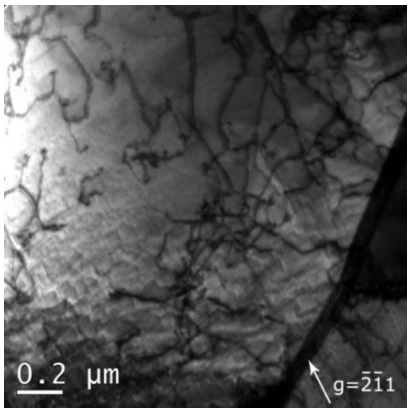

c)

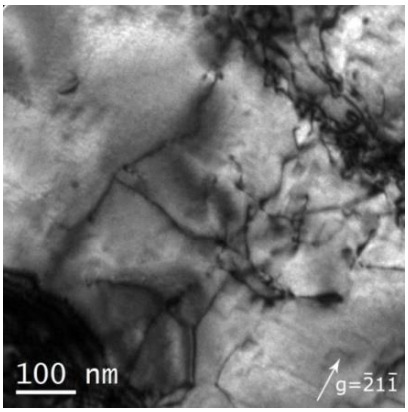

d)

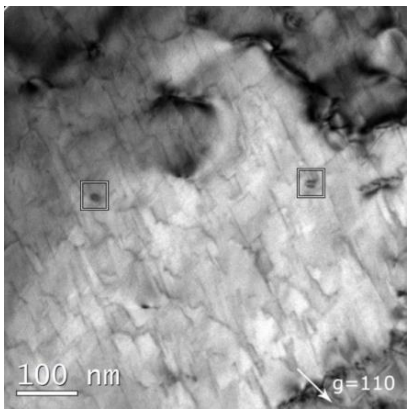

e)

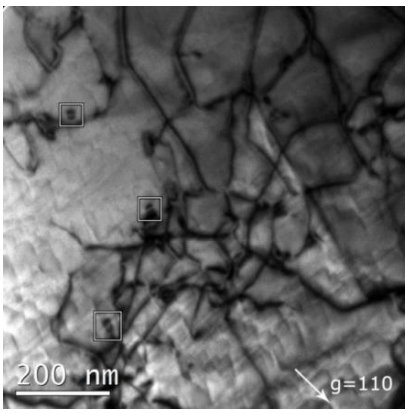

f)

Fig. 3.3.10. TEM micrographs showing the change in dislocation density with removal of the exposed surface layers in DF_RX 20% deformed sample: a) at the exposed surface, b) 2.5 μm removed, c) 5 μm removed, d) 12.5 μm removed. Figs. (e) and (f) demonstrate the dislocation loops observed within 6 μm depth from the exposed surface.

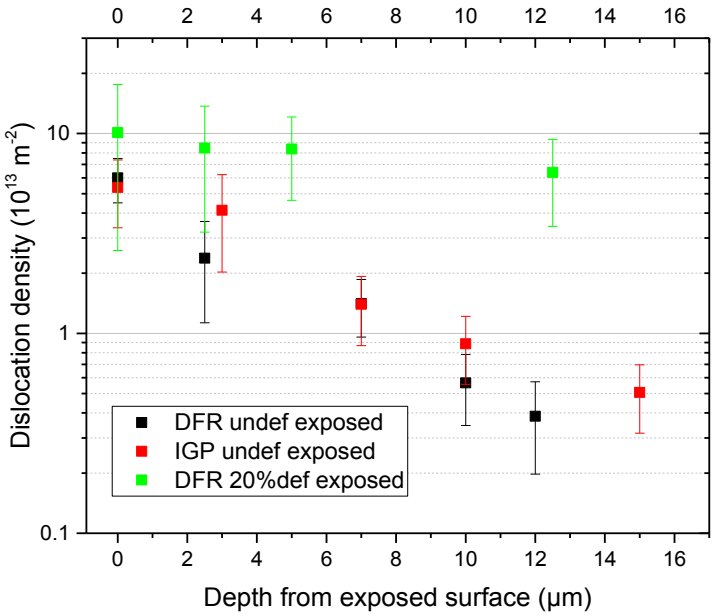

Fig. 3.3.11. Average dislocation density measured in DF_RX and IGP tungsten grades as a function of distance from the top of the exposed surface.

3.3.4 Plasma exposure of single crystal tungsten.

Deuterium retention and surface morphology in the single crystal tungsten samples exposed to high flux plasma was investigated in the PhD thesis of Luxherta Buzi [73] using scanning electron microscopy. Here we present a systematic study of the surface and sub-surface regions of similar material which reveals the microstructure induced by the high flux plasma exposure. Using TEM we reveal fine features of the microstructure which help to provide explanations for the thermal desorption spectroscopy measurements, as well as to clarify the impact of initial defects in the material on the emergence of the plasma exposure induced defects. Unfortunately, there was not a lot of material left after the different post-exposure analysis. We have received two samples for the in-depth TEM investigation, which were exposed at 520 K and 870 K at PSI-2 and Pilot PSI devices respectively. While the total fluence was the same on both samples (with a value of 10^{26} D/m^2), the particle flux was 10^{22} D/m^2/s and 10^{24} D/m^2/s on the PSI-2 and Pilot-PSI devices, respectively. SEM revealed the presence of blisters in both samples after plasma exposure. The blisters were of so-called 'dome' and 'flat-top' form with a size of 0.1-1 μm in diameter [74], see Fig. 3.3.12. The presence of such blisters is usually associated with plastic slip, causing displacement of a part of the crystal, under which the blister is located.

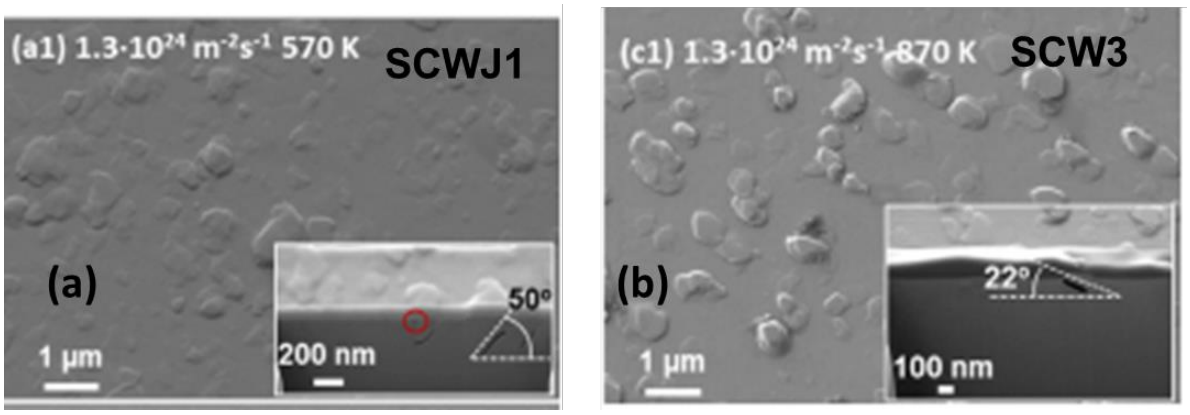

Fig. 3.3.12. SEM images of blisters observed in the single crystal tungsten exposed at (a) PSI-2 and Pilot-PSI (b). The images are taken from [74].

The microstructure of the single crystal tungsten sample exposed at PSI-2 at 520 K is presented in Fig.3.3.13. Reference measurements done for the bulk sample (double side polishing) and non-exposed surface (bottom-side polishing) did not reveal any microstructural features as expected for a pure single crystal. Example of a reference TEM picture is shown in Fig. 3.3.13 (d). Diffraction pattern confirmed the orientation of the crystal to be <110>. After the exposure, the dislocation networks and individual lines were identified up to the depth of 10 μm, as demonstrated in Fig. 3.3.13. No dislocations were registered by inspecting the slice taken at a 12 and 25 μm distance from the exposed surface. Hence, we conclude that the depth limit of plasma exposure induced microstructure changes was in the range of 12 μm.

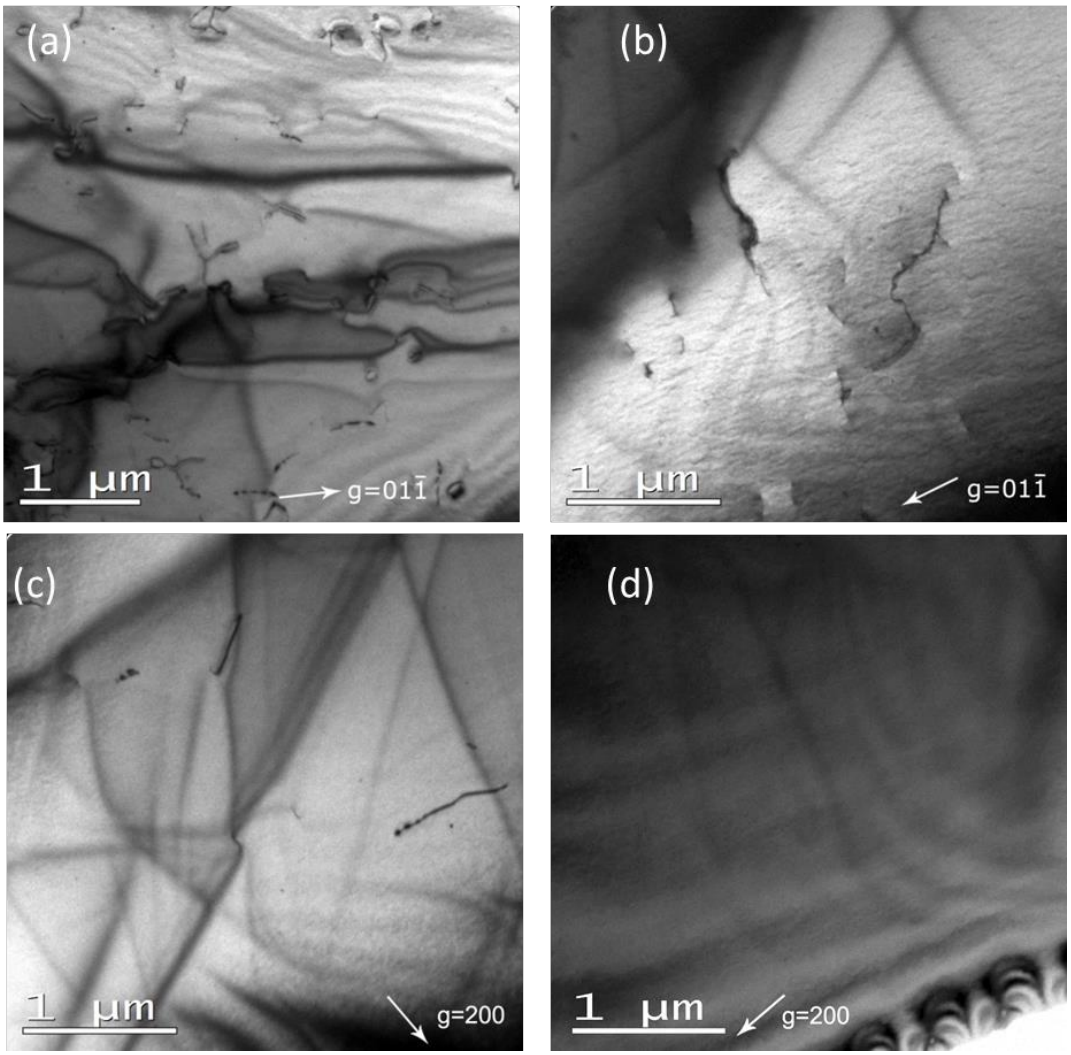

Fig. 3.3.13. TEM micrographs of single crystal tungsten (PSI-2 exposed) showing change in dislocation density with removal of the exposed surface: a) top surface (back-side polishing); b) 3 μm removed; c) 8 μm removed; d) 12 μm removed.

The microstructural evolution of the single crystal exposed at Pilot-PSI at 870 K is presented in Fig. 3.3.14. In this case, the top surface dislocation density was approximately 10^{13} m^{-2}, which is considerably lower than that seen in the PSI-2 exposed sample. This variation is attributed to the exposure temperature difference. The surface layer exhibits numerous dislocations, see Fig. 3.3.14 (a). At a depth of 3-7 μm, see Fig. 3.3.14 (b) and (c), the appearance of dislocation lines or loops becomes less frequent. Finally, at the depth of 15 μm, very few dislocation lines were seen over the whole transparent area. No dislocation structures were registered when inspecting the slice taken at a 25 μm distance from the exposed surface, demonstrating that plasma exposure induced microstructure is limited to 15-25 μm sub-surface area.

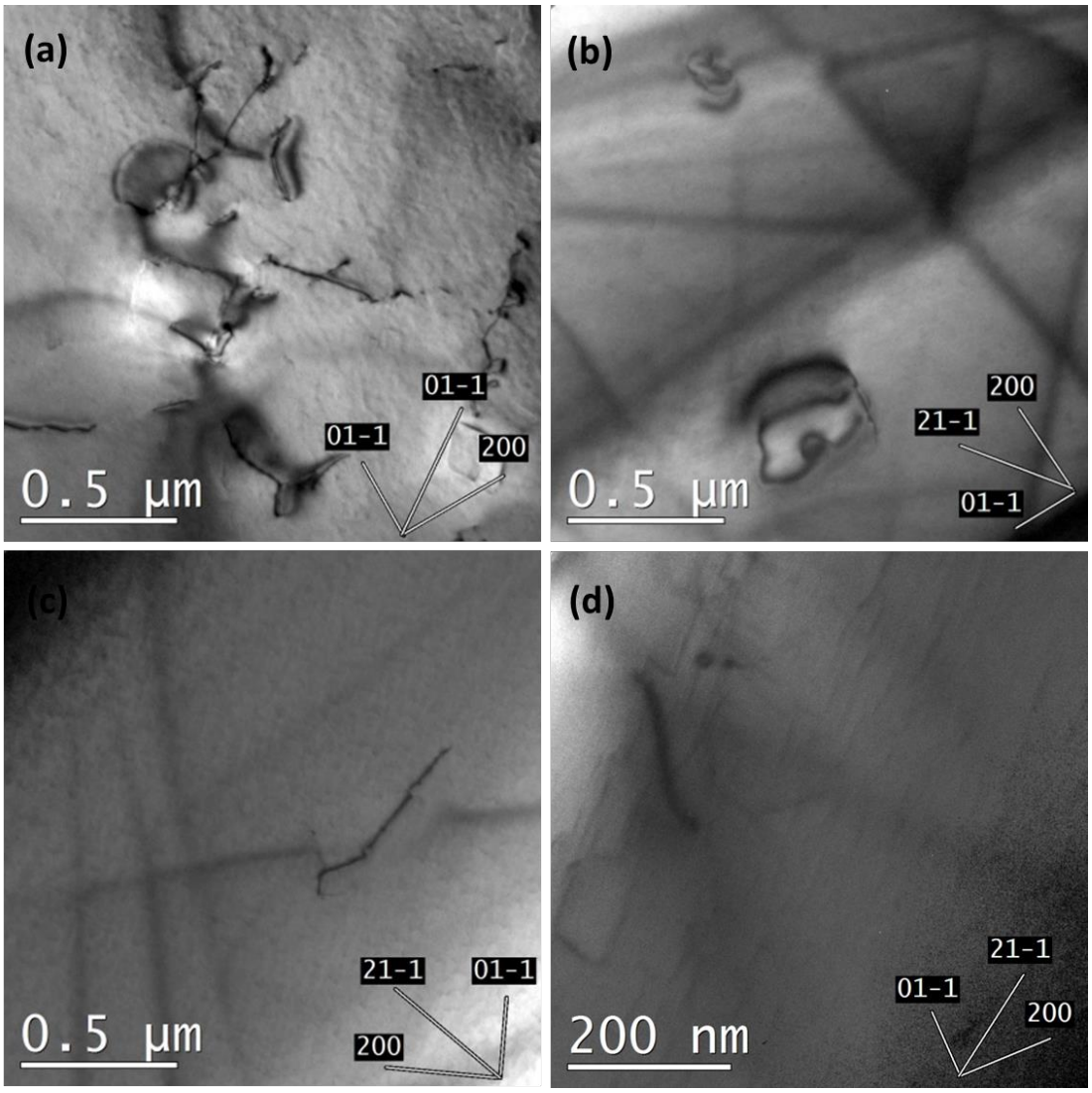

Fig. 3.3.14. TEM micrographs of single crystal tungsten (Pilot-PSI exposed) showing changes in dislocation density with removal of the exposed surface: a) top surface (single side polishing); b) 3 μm removed; c) 7 μm removed; d) 15 μm removed.

Fig. 3.3.15 presents the dislocation density calculated for both samples. As one can see the dislocation density on the surface of the exposed material (i.e. within approximately 200 nm) reaches 10^{13} m^{-2} and 7×10^{13} m^{-2} in the sample exposed, respectively, in Pilot-PSI and PSI-2. Inspection of the sub-surface region shows that dislocation density decreases nearly exponentially, dropping down by one order of magnitude within one μm. A simple analytical expression for the dislocation density as a function of depth can be derived, of the type: $p(\boldsymbol{h})=\boldsymbol{p}_0\times\exp(-\boldsymbol{\alpha}\times\boldsymbol{h})$. Here, $\boldsymbol{h}$ is the depth, $\boldsymbol{p}_0$ – initial dislocation density and $\boldsymbol{\alpha}$ is the rate of the decrease of the dislocation density. There is no specific reason behind the choice of the exponential function, however, all the measurements done on the plasma exposed samples shown

nearly linear decrease of the density in the log-linear scale. We can see that the slopes (i.e. **α**) are nearly the same for both samples. A steep reduction occurs within the whole range of the inspected depth up to the point where the detection of dislocation lines within a transparent area of the TEM sample is no longer possible. Accordingly, the pristine defect-free microstructure of both samples is once again seen beyond a depth of about 15 μm. We would like to stress that the above observations were confirmed by statistical analysis of a large amount of data. For each depth observed, 10-20 TEM images were analysed after selecting different areas, which ensures the results are representative.

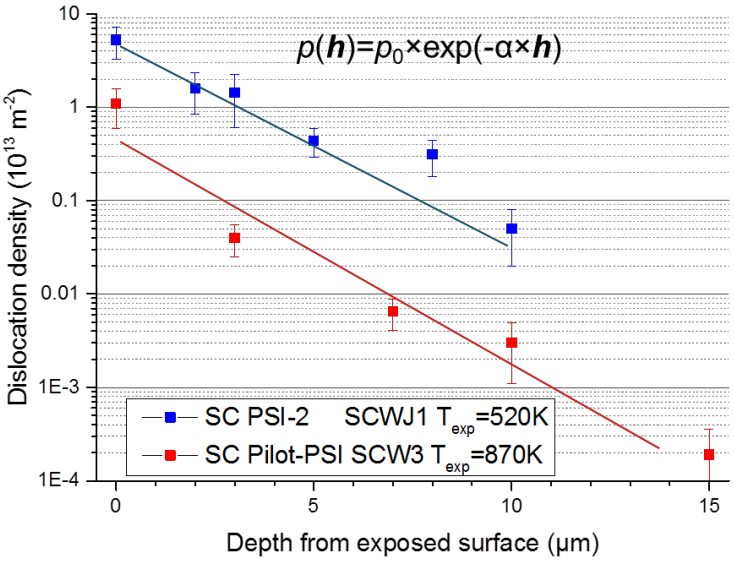

Fig. 3.3.15. Average dislocation density measured in the single crystal tungsten samples exposed at PSI-2 and Pilot-PSI.

In the last part of this section, we present TEM observations of dislocation loops. These dislocation loops were observed in both of the plasma exposed single crystal samples. Loops can reach a size of 100 nm, while their density is about 10^{18} m^{-3}. The g•b analysis revealed that these loops were of the edge type and interstitial in nature, like in the case of DF_RX samples. Identification of the Burgers vectors showed that both $a_0/2\langle 111\rangle$ and $a_0\langle 100\rangle$ loops were present. The loops were observed in the depth range between 3-10 μm. Apparently, at smaller distances from the plasma exposed surface, the loops were sunk at the surface under the action of the image forces. Whereas, the formation of loops at a depth greater than 10 μm did not occur, due to insufficient stress.

As noted in sections 3.3.1-3.3.3, the presence of similar dislocation loops was also observed in the polycrystalline samples with and without pre-applied plastic deformation. Typical images of the dislocation loops seen after plasma exposure in DF_RX 20% samples, plastically deformed DF_RX and single crystal tungsten samples are shown in Fig. 3.3.16. While the nature and Burger vector of the loops coincide in the polycrystalline and single crystal samples, their dimensions and density differ. In polycrystalline samples the loop size was in the range of 10-35 nm, i.e. much smaller (by a factor of three) than in the single crystal. On the other hand, the density of the loops (10^{19} m^{-3}) observed in the polycrystalline is one order of magnitude higher than that in the single crystal.

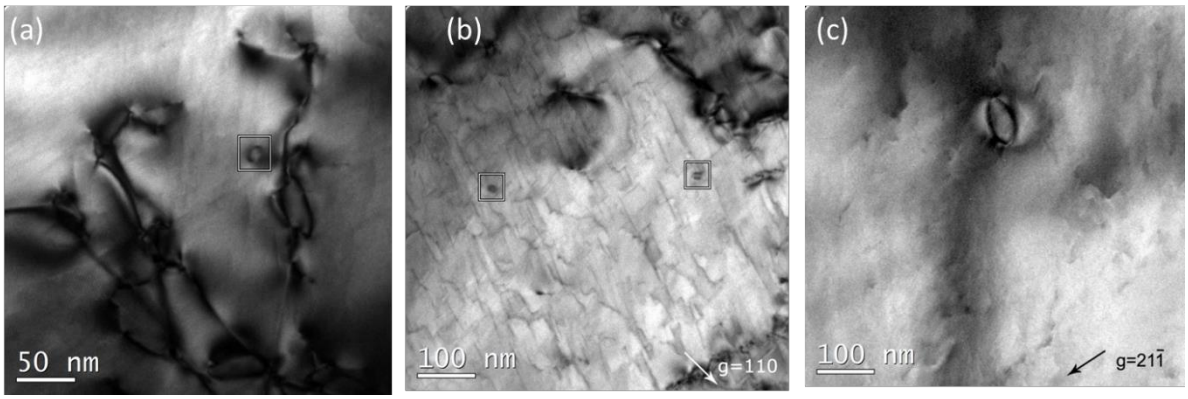

Fig. 3.3.16. Typical images of dislocation loops observed after plasma exposure in (a) DF_RX, (b) DF_RX 20% plastically deformed and (c) single crystal tungsten samples.

The formation of the interstitial dislocation loops is believed to be the result of the loop-punching mechanism [75] operating while bubbles and cavities grow under continuous plasma exposure. The essence of the loop-punching mechanism is the emission of the platelet of self-interstitial atoms (i.e. dislocation loop) from the over-pressurized bubble, which releases extra volume for the bubble thus releasing the pressure. Such consecutive process enables the growth of the bubbles in metals where the solubility of gaseous atoms is generally very low (especially for He). Recently in [76], computational analysis[1], based on the model of bubble nucleation driven by the trapping on dislocation networks (i.e. statistically stored dislocations and low angle

[1] The treatment was made specifically for a polycrystalline tungsten with the microstructure corresponding to as-forged or as-rolled conditions (i.e. textured grains, high density of small sub-grains and considerable dislocation density). Such model and analysis from Ref. 76. P. Grigorev, D. Terentyev, V. Dubinko, et al., *Nucleation and growth of hydrogen bubbles on dislocations in tungsten under high flux low energy plasma exposure.* Nuclear Instruments & Methods in Physics Research Section B-Beam Interactions with Materials and Atoms, 2015. **352**: p. 96-99. It is fully relevant for the currently studied material, but might be inapplicable for the fully recrystallized and single crystal ultra pure grades.

grain boundaries), was performed to determine plasma exposure conditions (i.e. temperature and flux) that favor the nucleation of deuterium bubbles. Subsequently, the bubble formation should be accompanied with the punching of the dislocation loops. The rather narrow range where dislocation loops are observed in the present work (i.e. within ~6 μm) can be explained by reduction of the deuterium flux (in the sub-surface region), required to induce sufficiently high pressure for loop emission, which ceases due to trapping in the sub-surface region. Observations of this strong shallow-depth trapping of deuterium under high flux exposures are regularly reported, based on the NRA measurements (see e.g. [49, 77-81]). This is an argument in favor of the scenario proposed above. However, in addition to the edge loops, some shear loops may also form due to the fast intensive plastic deformation.

Given the discussion above, we next present some supporting complementary experimental data obtained by nuclear reaction analysis and nano-indentation measurements applied to the above explored samples. These results are presented and explained in order to support the general ideas, discussion and conclusions drawn on the basis of this work.

3.3.5 Supplementary experimental data.

In this section, the data obtained by complementary experimental techniques - nanoindentation (NI) and nuclear reaction analysis (NRA), is presented for some of the above studied materials, which were measured respectively before and after plasma exposure. Note that planning such sequential experiments involving NRA, NI, TEM and plasma exposure is a rather lengthy, costly and complicated process. NRA measurements were performed at the Institute of Plasma Physics Garching (Germany), NI studies were done at Universite Catholique de Louvain (Belgium), TEM investigations were performed at both SCK-CEN (Mol, Belgium) and CIEMAT (Madrid, Spain), and the plasma exposures were performed at DIFFER (The Netherlands). For those reasons, the complete set of experimental data was collected only for the reference tungsten (IGP grade) exposed at Pilot-PSI at 470 K and single crystal tungsten exposed at PSI-2, at 570 K. NI and NRA measurements were performed by a colleague Anastasia Bakaeva, who is working to obtain a PhD in the Fusion domain, however we show these results as they make a very important contribution to the discussion and conclusions drawn at the end of this study.

NRA depth profile of the retained deuterium for the IGP grade samples exposed at 470 K is shown in Fig. 3.3.17 (a). We see a high deuterium concentration in a very narrow region close to the sample surface, in fact the majority of the NRA-detected deuterium is located within 1 μm from the top surface. The concentration goes down nearly

logarithmically with the depth. As said above, at the depth of 6-7 μm the signal is no longer strong enough to deliver reliable data [82].

The evolution of hardness as a function of the indentation depth, obtained by averaging the results of 25 indents, is presented in Fig. 3.3.17 (b). For the non-exposed IGP samples the saturated (bulk) hardness is 7±0.1 GPa. This value is considerably higher than the 6 GPa and 5.6 GPa reported for the recrystallized polycrystalline tungsten (of similar purity as studied here) by Armstrong et al. [83] and by Zhang et al. [84]. This increase must be attributed to the presence of dislocations and low-angle grain boundaries (see details in the section 3.3.1), which offer extra resistance to the penetration of the indenter thus affecting the hardness of the material. Also note that there is only a small deviation in the results obtained in the two probed areas (each area was scanned by 25 indents) indicating that the hardness profiles are likely quite uniform across the surface. The kinetic energy of deuterium ions during the plasma exposure was ~50 eV, implying that ion penetration depth is limited to several nanometers. However, the resulting increase of hardness spreads over a penetration depth of about 300 nm, meaning that the actual plasma-induced damage spreads to a distance of 1.5-3 μm, keeping in mind the extension of the plastically affected region already described. Fig. 3.3.18 (a) superimposes the results of the NRA and TEM measurements. Fig. 3.3.18 (b) compares the decay of the excess of the hardness measured by NI and the dislocation density as a function of the probed depth. This clearly shows that there is very good correlation between the D concentration profile and the increase in hardness after plasma exposure.

Yet, we see that this increased hardness vanishes as the plastically affected region reaches about 10 μm, which is close to the depth at which the dislocation microstructure induced by the plasma shot (see section 3.3.1) recovers to that corresponding to non-exposed material.

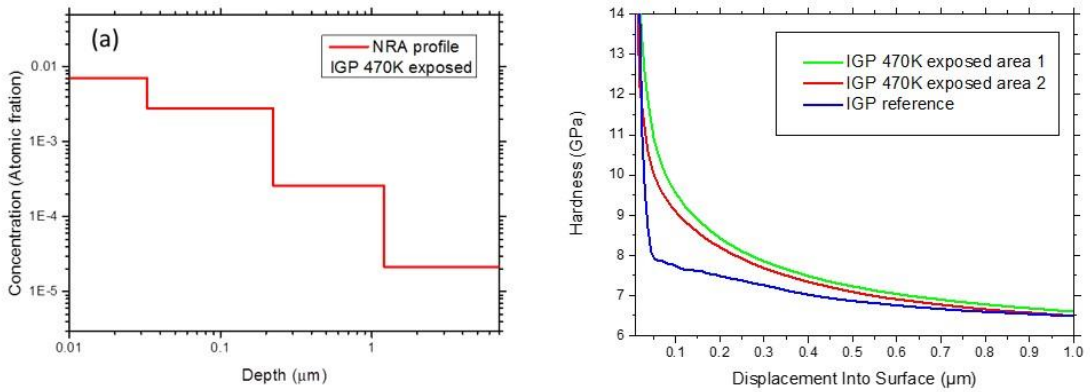

Fig. 3.3.17. (a) NRA depth profile of retained deuterium and (b) hardness depth profile measured by nano-indentation; the results are given for the IGP grade exposed at 470 K, as was studied in details by TEM in section 3.3.1.

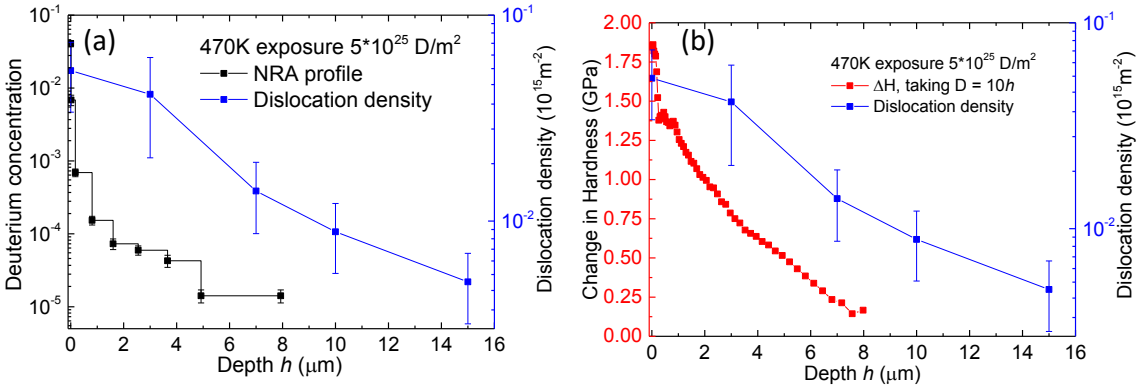

Fig. 3.3.18. (a) correlation between the NRA profile of deuterium and dislocation density profile; (b) correlation between the change of hardness and dislocation density. The depth, h corresponding to NI measurements is scaled as h_{NI}×10 to reflect the scale of the plastically-affected zone. The results are provided for the IGP grade tungsten exposed at 470 K at Pilot PSI.

The next set of NRA and NI results is given for the single crystal tungsten that has been exposed to plasma at PSI-2 at 520 K. Fig. 3.3.19 (a) shows that deuterium is retained mostly at the top surface of the material, the signal being close to the resolution limit at a depth of 1 μm. At the same time, Fig. 3.3.19 (b) shows that plasma exposure resulted in an increase of hardness which spreads to more than 1 μm of the indentation depths. Thus, the size of the plastically affected zone with the increased hardness could reach 5-10 μm.

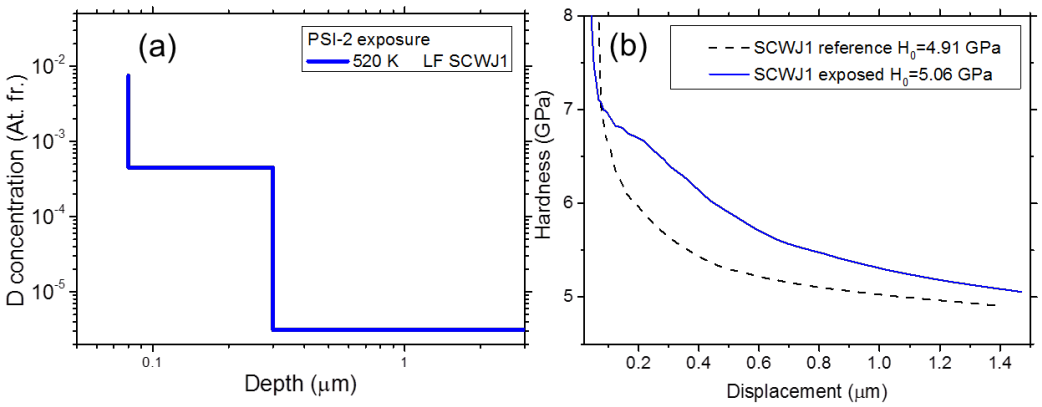

Fig. 3.3.19. (a) NRA depth profile of retained deuterium (taken from [73]) and (b) hardness depth profile measured by nano-indentation; the results are given for the single crystal tungsten exposed at 520 K at PSI-2, that was studied in detail by TEM in section 3.3.4. The increase of hardness is well resolved within at least 1 μm. The NRA and NI measurements are performed in the center of the exposed sample.

Fig. 3.3.20 collects the dislocation density, retained deuterium profile and the measured change of nano-hardness. The lower X axis denotes the depth for NRA and TEM measurements, whereas the upper X axis specifies the extension of the plastically affected zone due to the nano-indentation. From Fig. 3.3.20 it clearly follows that the strong reduction of the NRA measured deuterium concentration correlates well with the reduction of dislocation density, similarly to that observed for the IGP tungsten. At the same time, an evident increase of hardness (i.e. the difference of the hardness measured after and before the plasma exposure) occurs in the range of 1-10 μm where limited plasma exposure induced damage takes place. Hence, it appears that strong retention of deuterium in the surface layer does not give rise to the increase of the nano-hardness. However, plasma exposure induced plastic deformation might explain the high concentration of deuterium in the surface layer, its exponential reduction with depth, and the extra hardness measured up to the indentation depth of 1.5 μm.

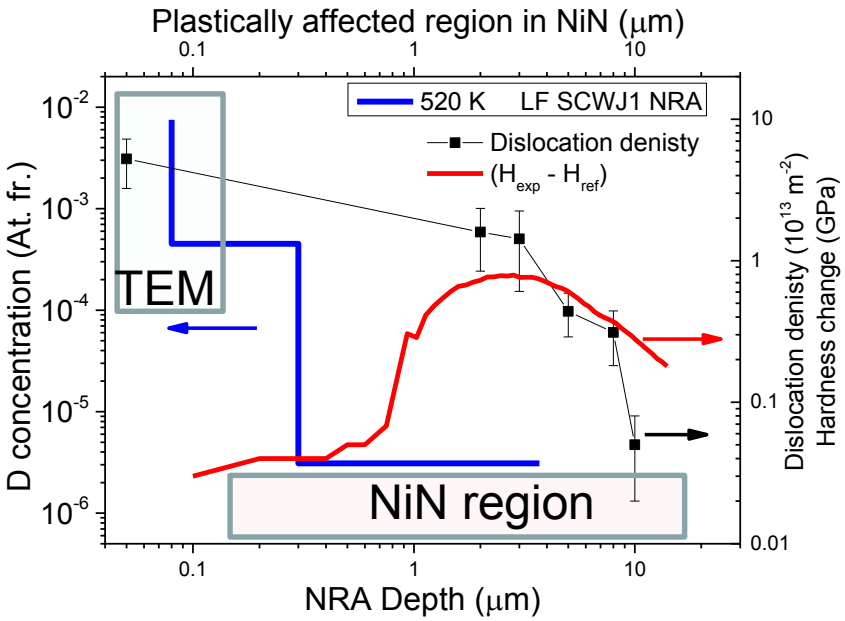

Fig. 3.3.20. Composite figure demonstrating interrelation between the depth deposition of: NRA-detected deuterium concentration (blue line); dislocation density (black line with square dots) calculated by TEM investigation; excess hardness (on right-hand side axis, in GPa units) as measured by NI (red curve). The excess hardness is the difference of the hardness measured before and after the plasma exposure. Region where the TEM was applied to investigate the surface microstructure is labeled as "TEM", and the plastically affected region under the nano-indentation is labeled as "NiN region".

These collected results suggest that the NRA detected deuterium could be stabilized by dislocation networks, which are generated as a result of plasma exposure. It could even be that dislocations assist nucleation of stable deuterium clusters which can grow further and form blisters, as was discussed in [85]. At the same time, as the density of dislocations decreases below certain critical value, the rate of trapping of continuously penetrating deuterium atoms is no longer high enough to induce the nucleation reaction. Consequently, stable deuterium clusters do not form or grow into bubbles/blisters beyond a certain depth. According to the present investigation this depth is about 1-2 μm and corresponds to a dislocation density of about 10^{12} m^{-2}. Note that the extension of the deuterium depth profile measured by NRA in the single crystal is much less than that measured in the polycrystalline material. Apparently, the availability of grain boundary interfaces and sub-grains can promote nucleation of stable deuterium clusters and bubbles at greater depth.

4. Summary, Conclusions and Outlook.

This is the last chapter which contains a concise summary of the observations made, discussion of those observations, conclusions and outlook for further study. The summary of the results is accompanied by few figures containing the most important results and data useful to reconcile the conclusions drawn afterwards. The outlook content is based on the analysis and current understanding of the observations made in the so-far explored plasma exposure conditions.

4.1 Summary of the experimental observations.

Several tungsten grades have been studied in this thesis - starting with the baseline commercial tungsten produced by Plansee according to the ITER specification [17] and finishing with samples of single crystal tungsten. The objective of the study was to examine the microstructure of this material after high flux plasma exposure, an environment which is relevant for the ITER divertor region [43]. We reveal the relationship between the initial microstructure and the final one induced by plasma exposure. To pin point the mechanisms operating under the plasma exposure, complementary interruptive mechanical tests were performed, to characterize the plastic deformation mechanisms at 300°C and 600°C, up to the ultimate tensile strength. These observations were then used to analyze the microstructure after plastic deformation and to clarify those features which control the processes under high flux plasma exposure.

To more fully understand the importance of the initial microstructure on post irradiation morphology, four chosen materials were irradiated in similar conditions, exposed to high-flux plasma at temperatures ranging between 470-620 K. This is below (or close to) the ductile-to-brittle transition temperature, but certainly not in the range where tungsten is already fully ductile. The four materials tested were: baseline tungsten produced by Plansee in as-received state (IGP); the same material but recrystallized at 1600°C for 1 hour to achieve removal of dislocations and remove the texture (DF_RX); the recrystallized material subjected to plastic deformation up the ultimate tensile strength to induce high dislocation density (DF_RX_20%); and single crystal tungsten (SC).

The microstructure of the non-exposed materials is characterized in Section 3.1. EBSD analysis confirmed that the DF_RX grade has big grains (majority of grains are 50-150 μm), while the IGP has elongated grains with fine sub-grains, which is due to residual plastic deformation induced by the fabrication process. Dislocation density was found

to be of the same order, but the ratio of the initial dislocation density to the grain size is higher in the IGP material. The single crystal sample was proved not to have any structural defects. Micro-hardness tests reconfirmed that the lowest hardness occurred in the single crystal, while the highest was in the IGP grade. This difference reflects the amount of microstructural defects, such as dislocations and grain boundaries, which impact the resulting hardness [83].

The mechanisms of plastic deformation are studied in Section 3.2. The baseline and recrystallized tungsten grades were deformed at 300°C and 600°C up to the ultimate tensile strength and TEM studies were made in the necking region. Visible light microscopy was applied to characterize the morphology of the grains, and this revealed that the grains become elongated (in accordance with the applied load) but their size did not significantly change. Thus, no grain growth occurred as a result of the plastic deformation.

TEM observed microstructures after plastic deformation were characterized and compared between these two grades in terms of dislocation density, heterogeneity, observation of pile-ups and tangles specifically near high angle grain boundaries. The evolution of dislocation density as a function of deformation strain is presented in Fig. 4.1. The observed evolution of dislocation density was compared with the predictions of the previously developed thermo-mechanical model for the plastic deformation of polycrystalline tungsten. Good agreement was found to exist, not requiring any modification of the original parameter set.

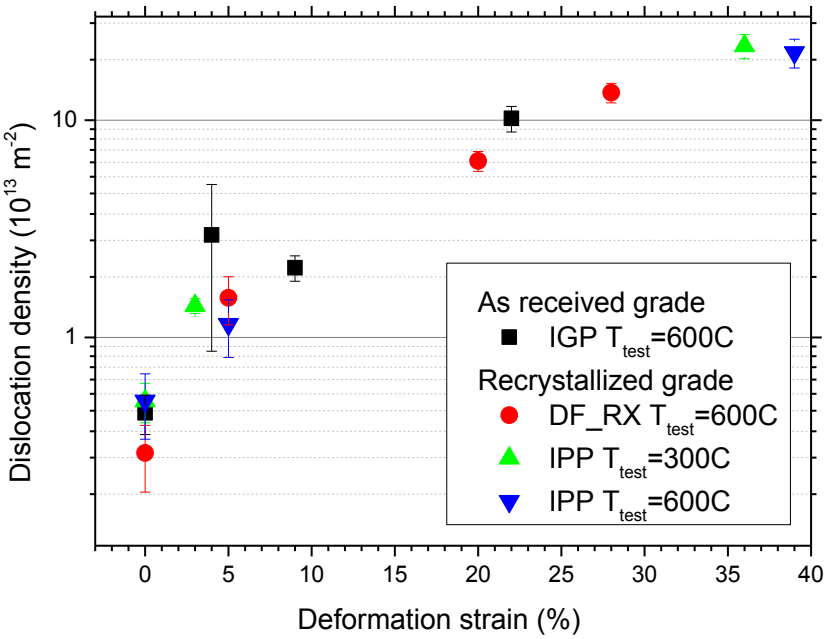

Fig. 4.1. Dislocation density as measured by TEM in as-received and recrystallized commercial tungsten grades. The test temperature is specified in the figure.

The features of the deformation induced microstructure observed in the recrystallized sample, leads to the conclusion that the initial contribution to plastic deformation comes from the multiplication of dislocations inside large grains. This is followed by the formation of dislocation pile-ups in front of high angle grain boundaries, and finally by transformation of these pile-ups into cells, resulting in grain refinement. Such a sequence of plastic deformation mechanisms ensures significant capacity for the work hardening of the recrystallized material, and therefore such material exhibits large uniform elongation but low yield stress.

In the stress-relieved IGP grade, the capacity for strain hardening is very small, because of the high ratio of initial dislocation density to the grain size. Due to the small grain size of this material, the major contribution to flow stress is due to the Hall-Petch mechanism. The yield stress of the IGP (470 MPa) is about four times higher than that of the recrystallized material (102 MPa). Because of this high yield stress, the UTS (500 MPa) is reached shortly after the yield point and diffuse necking emerges at very small strain. However, post-necking deformation continues up to about 22% with the localized neck emerging at around 20%. TEM measurements performed in the regions of diffuse and localized neck revealed that dislocation density exhibits a steady increase with the accumulated strain, see Fig. 4.1. We saw that contrary to the recrystallized sample, dislocation density increase was a result of the formation of bands of low-angle grain boundaries in the region of 4-9% strain. At larger strains, deformation occurred by emission of dislocations from the grain boundary interfaces. This results in the formation of dislocation tangles spreading from the grain boundary towards dislocation free grains. This expansion of dislocation tangles basically controlled the plastic deformation and accommodation of these elongated grains to the applied load. This is likely to be the principal difference in the mechanisms controlling plastic deformation of both recrystallized and as-fabricated tungsten materials.

As a next step, TEM investigation was carried out on the plasma exposed samples. The exposure was carried in the temperature range of 470-620 K and the total fluence was $5{\cdot}10^{25}$ D/m^2. The microstructure was studied in the surface layer, in several sub-surface regions down to about 20 μm from the exposed surface and deep in the bulk (to confirm that the plasma exposure did not change the bulk microstructure of the samples). In all cases it was confirmed that the bulk microstructure of samples remained equivalent to the initial one.

The first investigated material was IGP grade tungsten, this study is presented in Section 3.3.1. A striking observation was the high density of dislocations seen at the exposed surface. Dislocation density increased by nearly one order of magnitude on average, and locally the density could reach 10^{15} m^{-2}. If one compares this

microstructural state with the results obtained for the plastically deformed materials, a similar increase in the dislocation density is seen at plastic strain levels in the range of 5-10%. In addition to dislocation lines and tangles, a pattern of elongated sub-grains was also clearly visible, which means that the grain structure was not affected by the plasma exposure. The interface of sub-grains, which showed sharp contrast in the reference sample, became broadened after the plasma exposure (see Fig. 3.3.2 (b), in Section 3.3.1). These microstructural changes were attributed to the load induced by thermal stresses eventually resulting in plastic deformation. As a matter of fact, the broadening of grain boundaries has also been observed after plastic deformation, as soon as the plastic strain exceeded 5%. On the basis of these observations, it is possible to speculate that the material exposed to high flux plasma at Pilot PSI experienced plastic deformation even though the surface temperature was below DBTT. Quite similar surface microstructure was observed in the recrystallized DF_RX grade, pre-deformed DF_RX and even single crystal samples. The signature of this intensive plastic deformation was observed in all the tested materials, and representative TEM images are presented in Fig. 4.2. Although some of those images have been already presented in Section 3,3, we collect here the surface images of the four different materials for convenience of a reader.

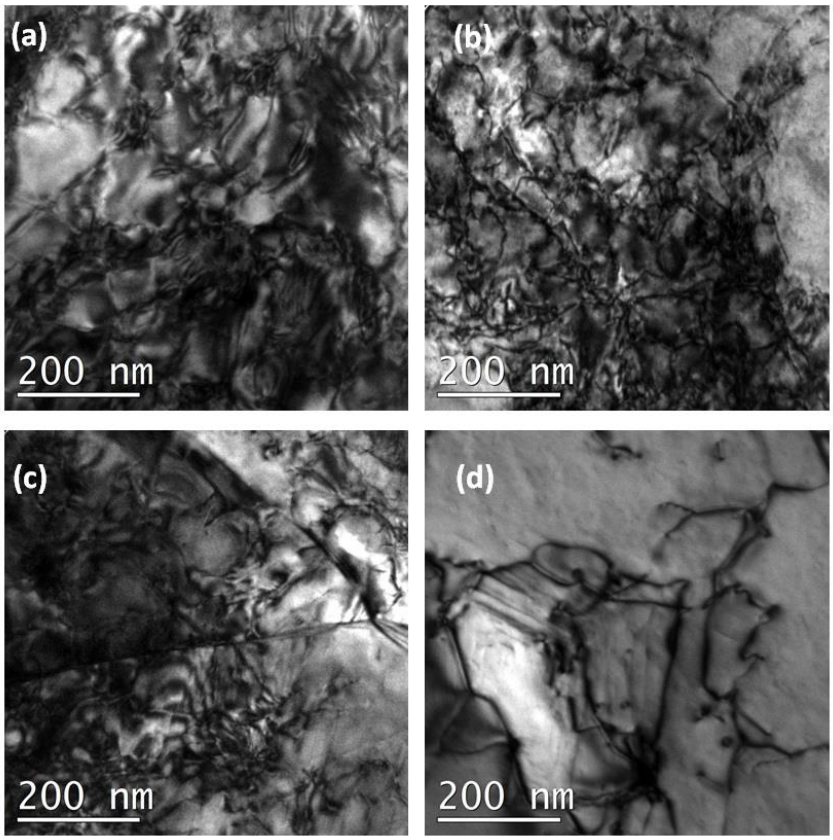

Fig. 4.2. TEM images of the surface layer of the plasma exposed tungsten samples, namely: (a) IGP; (b) DF_RX; (c) DF_RX_20%; (d) single crystal.

According to the TEM observations discussed in Section 3.3.1-3.3.4, plasma exposure induced dislocations are arranged in networks and tangles. Dislocations attain a cellular structure having both types of dislocations segments with the Burgers vector of a_0<100> and $a_0/2$<111> type. This microstructure is very close to that observed when high temperature tensile tests were performed, see Section 3.2.

Plastic deformation applied to tungsten below DBTT (in the temperature range 200-600°C) has been studied by several authors [55, 56]. They found that at a low temperature (in compression load) dislocations are mostly arranged in the regular dipoles, which is not the case of our observations. Given that we did not observe long dislocation dipoles, we conclude that the internal stress state under the plasma exposure in the sub-surface region differs from the one achieved in compression experiments performed at a similar temperature range. Apparently, the internal stress was much higher in our experimental conditions, which led to intensive dislocation curving and tangling.

High levels of internal stress can be achieved either by low temperature deformation, or by high strain rate deformation. Referring to the investigated samples, fast heating of the surface by high-flux plasma is one possible mechanism inducing strong thermal gradients and consequent local high speed deformation. The effect of deformation strain rate in tungsten has been studied by Chiem and Lee [56]. They point out that high strain rate deformation often leads to the formation of twins. In this work, we did not observe twins not in single crystals neither in the polycrystalline tungsten grades. Indeed, the plasma exposures were performed well above the room temperature, while the study of Chiem and Lee was carried out at room temperature under quasi-static and high strain rate loading.

Under quasi-static conditions, dislocation configurations consist of some short dislocation segments, as is the case of our reference and 20% deformed polycrystalline samples, separated by relatively large areas of low dislocation density. In the work of Chiem [56] and in the present study, contrast analysis revealed that these dislocations are of screw type with Burgers vectors parallel to the primary slip directions of <111> family.

Upon high strain rate deformation, the dislocation distribution showed a high degree of dislocation interaction and the resultant tangles appear to line up along the primary slip plane, in which dislocations lie parallel to the <111> and <110> family of directions for g=(-211). Our micrographs also identified dislocation lines with such orientations and the analysis of the Burgers vector identified these dislocation segments to be of $a_0/2$<111> and a_0<100> type. The latter types of dislocations appear mainly in the networks and tangles as short junctions connecting long screw $a_0/2$<111> segments.

As reported in [56], further increase of strain rate results in the formation of elementary cell structures. At this stage of deformation, dislocation tangles are well developed. Similar cell structures were also observed in the surface layer of plasma exposed samples.

Therefore the dislocation patterns observed in the surface layer and shallow sub-surface region accord with the microstructures induced by high strain deformation in [56]. This confirms our assumption about high stress state and high-speed plastic deformation driving the establishment of plasma exposure induced dislocation microstructures. Estimation of the temperature gradient across the sample depth, by solving the heat equation for the steady-state regime (i.e. constant surface temperature) results in values of ~2.5 mK/μm for 600 K exposure temperature in PILOT-PSI and an even lower gradient for the other two exposure conditions studied here. Variations of temperature across the surface of the sample can also invoke mechanical stresses. However, for this experiment, the temperature profile is known be essentially flat, thanks to the high thermal conductivity of tungsten. Typically, the variation of temperature is defined by the size of the plasma beam and it does not exceed 10-20 K for the area of about 20 mm^2, while our samples had an area of 10 mm^2. Hence, we expect that the major source of the thermal stresses comes from the gas pressure and temperature escalation/descent at the beginning and end of the exposure period.

Inspection of the dislocation microstructure at a depth of 3-10 μm, revealed regularly dislocation loops. The density and size of the loop depended on the grade of tungsten, and the general trend was the cleaner the material – the larger the loops.

Dislocation loops with "coffee bean" and "dot-like" contrasts were regularly observed. Highly typical examples of such loops are presented in Fig. 4.3.

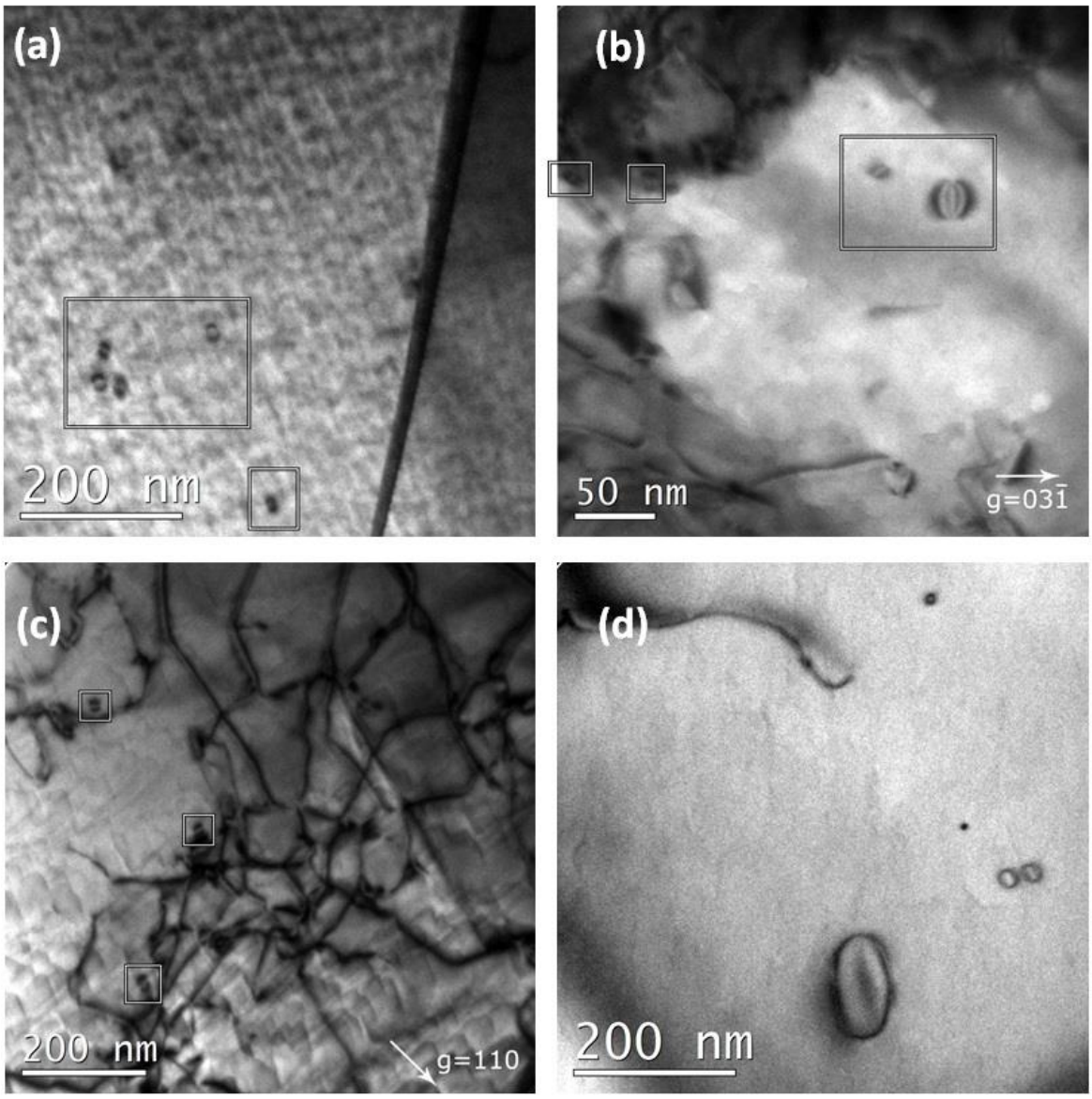

Fig. 4.3. TEM images demonstrating the presence of dislocation loops in (a) IGP; (b) DF_RX; (c) DF_RX_20%; (d) single crystal after the plasma exposure.

These loops were interstitial in nature with Burgers vector of both types: $a_0/2\langle 111\rangle$ and $a_0\langle 100\rangle$. Such loops were identified only in the plasma exposed samples. The formation of interstitial dislocation loops, which were not observed in reference samples or after heavy plastic deformation at 600°C, is clearly a result of plasma exposure. Although loops have been observed at a depth of 3-10 μm, their presence in the surface layer cannot be excluded, as observation of individual dislocation loops could potentially be obscured by the dense dislocation patterns.

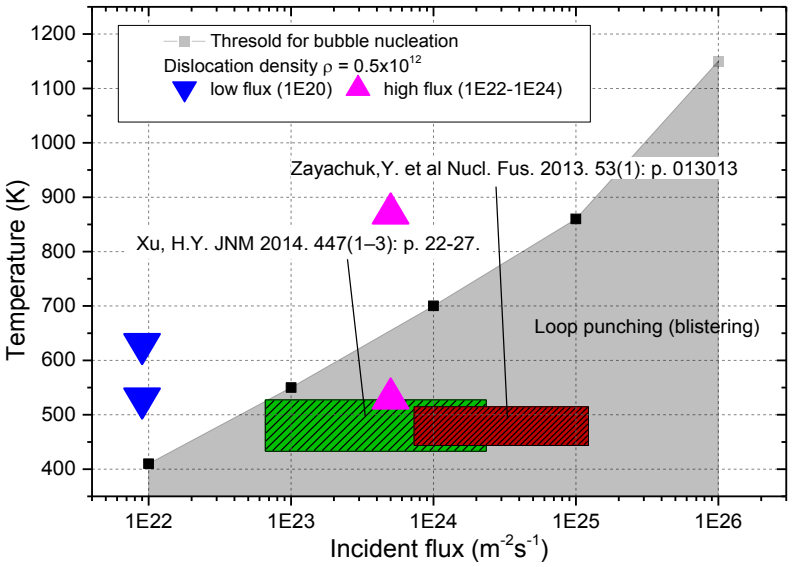

Fig. 4.4. Comparison of the experimental conditions reporting the observation of the blisters from [86] with prediction of the model from [31] , which predict the conditions for the nucleation of stable deuterium bubbles and their growth by loop-punching.

The formation of the interstitial dislocation loops is believed to be the result of the loop-punching mechanism [75] operating while bubbles and cavities grow under continuous plasma exposure. Recently in [76], computational analysis based on the model of the bubble nucleation driven by the trapping on dislocation network (i.e. statistically stored dislocations and low angle grain boundaries) was performed to determine plasma exposure conditions (i.e. temperature and flux) that favor the nucleation of deuterium bubbles. The growth of the bubbles should be accompanied with the punching of the dislocation loops. The result of this assessment is presented in Fig. 4.4. The rather narrow range where dislocation loops are observed in the present work (i.e. within ~10 μm) can be explained by the reduction of the deuterium flux (in the sub-surface region), needed to induce sufficiently high pressure to promote loop emission, which ceases due to trapping in the sub-surface region. Strong shallow-depth trapping of deuterium under high flux exposures is regularly reported, based on the NRA measurements (see e.g. [49, 77-81]), which is an argument in favour of the above proposed scenario. However, in addition to the edge loops, some shear loops may also form due to the fast intensive plastic deformation.

4.2 Conclusions.

On the basis of the test results, observations, and discussions presented above, we have reached the following conclusions:

(a) The microstructure was studied in detail by the means of TEM in the samples deformed at temperatures of 300°C and 600°C up to the ultimate tensile strength in as-produced and recrystallized ITER specification tungsten grades. In the mentioned above conditions, several stages of this plastic deformation are clearly deduced on the basis of the observed microstructural evolution. The measured dislocation density evolution demonstrates a deviation from the classical Mecking-Kocks law. This is attributed to the grain refinement, and at large strain rates to the formation of cellular structures as the nuclei of new low angle grain boundary interfaces. This information is important since it contributes to the development of constitutive laws for the effects of mechanical deformation of commercial tungsten grades.

(b) Comparison of plastic deformation evolution at 600°C in as-produced and recrystallized ITER specification tungsten grades points to the fact that significant deviation in the mechanisms mediating the deformation is present after recrystallization. In recrystallized tungsten deformation is controlled by dislocation multiplication and pile-up formation next to the high angle grain boundaries, which eventually causes crack initiation and its extension. In the case of as-produced tungsten with elongated grains and texture, the main deformation mechanism is apparently the dislocation-grain boundary interaction and grain boundary slip. The ability of grain interfaces to slip plays a major role in the ductility of as-produced tungsten. In contrast with this, the ductility of recrystallized tungsten is determined by the absorption/dissolution of dislocation pile-ups formed next to high-angle grain boundaries. This conclusion implies that control over the structure of grain interfaces and any possible modification of the grain interfaces which improves its coherency would also improve the plasticity of the material, and presumably would decrease the ductile to brittle transition temperature.

(c) Systematic TEM analysis of the surface and sub-surface regions of the samples with different initial microstructure exposed to high flux plasma, mimicking ITER divertor exposure conditions, revealed the occurrence of plastic deformation. This is heavily and strongly localized plastic deformation, which occurred irrespective of the initial microstructure, even in single crystal samples. However, the particular increase of the dislocation density and other regularly observed features depend on the initial microstructure. The average values of the dislocation density probed at different depths after the plasma exposure are summarized in Fig. 4.5 for all the studied materials. The TEM-inspected microstructure of the plasma exposed material recovers to the one observed in bulk at depths of about 12-20 μm.

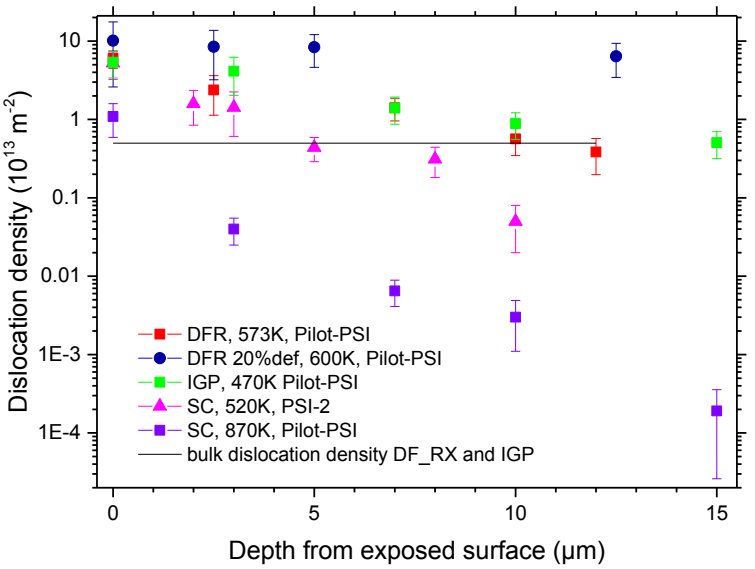

Fig. 4.5. Dislocation density as a function of depth for all the samples studied.

(d) Heavy plastic deformation observed in the sub-surface region can have strong impact on the sub-surface retention of deuterium, also the resulting internal stress could provoke crack initiation. Our TEM results confirm the presence of three depth regions, shown schematically in Fig.4.6. Following the notation of Tanabe [77], these are: the top surface (i.e. implantation range); the sub-surface region containing a strong gradient of deuterium concentration; and the bulk region where the penetration of deuterium is controlled by diffusion and trapping at natural defects.

Region I (implantation depth, several nm) is completely covered with dislocations, the localized density of which could be as high as 10^{15} m^{-2} in IGP tungsten grade. This value corresponds to an extremely strong plastic deformation (of about 10-20% as evaluated on the basis of dislocation density). The sub-surface region (i.e. region II) contains a lower dislocation density but still clearly exceeds the density of statistically stored dislocations in IGP tungsten. The gradient of dislocation density is about 1 m^{-2}μm^{-1} and 10 m^{-2}μm^{-1}, for the IGP and SC samples, respectively. This naturally implies a very strong gradient of this plastic deformation, which practically is confined within ~10 μm of the sub-surface.

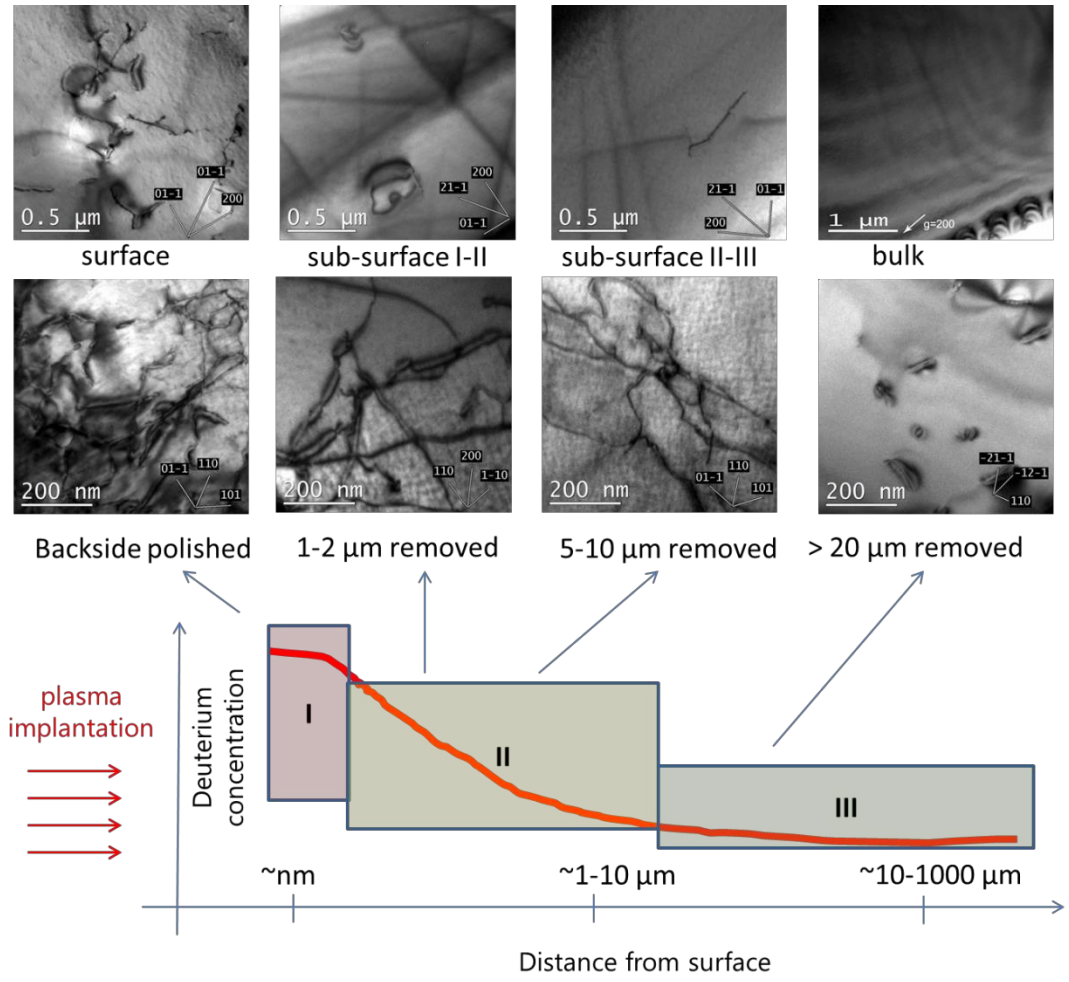

Fig. 4.6. TEM micrographs on the upper part show the evolution of the microstructure in SC tungsten (top row) and IGP tungsten (middle row) as a function of depth after exposure in PILOT PSI (470 K to 5×10^{25} D/m^2). The schematic in the lower bar shows the steady-state profile of deuterium diffusing in a field of traps (i.e. dislocations) as assessed in [85].

In order to reconcile our various experimental observations and give a coherent description of the effects of high-flux plasma on our sample materials we suggest that the sequence of events taking place is as follows:

(1) At the onset of exposure, the thermal gradient created generates mechanical stresses exceeding the elastic limit, thus initiating plastic deformation. In addition to thermal stress, there is evidence that the addition of hydrogen interstitials stimulates plastic deformation, as was revealed by the considerable reduction of pop-in stress under nano-indentation of pre-implanted tungsten [87]. Hence, the synergy between thermal stress and high concentrations of deuterium may reduce the limit for the onset of plastic deformation.

(2) The nucleation of deuterium clusters (of sub-nanometer size) occurs due to the trapping at dislocation lines and junctions, following the results of numerical simulations and its integrated analysis using available experimental data [85]. Note that a sustainable growth of deuterium clusters occurs only if the density of traps and upcoming deuterium flux is sufficiently high, as analyzed in [88] which was based on atomic-scale data.

(3) Once the stable deuterium cluster is nucleated (i.e. stable against temperature-assisted dissolution), it keeps on growing by emission of self-interstitial defects (i.e. releasing the vacancies necessary to accommodate upcoming deuterium atoms). As soon as the size of deuterium cluster/bubble reaches a certain critical value, growth occurs by the emission of dislocation loops (as was discussed in [76]) or by sliding of the sub-grains, if the deuterium cluster has transformed into "flake" occupying the grain boundary interface (as was observed e.g. in [78]).

(4) the growth of bubbles or flakes results in plastic deformation (see for instance FEM analysis of stress-strain near blisters in tungsten [48]), which is physically expressed by the emission of dislocation lines and loops. In turn, this results in the growth of overall dislocation density which we observed by TEM. This latter phenomenon eventually results in further increase of trapping and nucleation sites for new deuterium clusters.

Consequently, trapping of deuterium in dislocation networks and further production of local plastic deformation are two mutually-related processes occurring simultaneously under high flux deuterium plasma exposure.

4.3 Outlook.

In conclusion, we feel able to suggest a number of directions for further research which would essentially complete the already established results and help to clarify/validate some of the assumptions and observations made here, from which we have drawn the conclusions presented above.

1. First of all, it is necessary to perform a similar study using low flux deuterium plasma exposure. For that purpose, the PlaQ setup delivering a flux of 10^{19}-10^{20} $m^{-2}s^{-1}$ would be perfectly suited. Currently, we assume that a synergy of plastic deformation and high concentration of deuterium (resulting from the high flux load) in the sub-surface region results in damage that can be observed by TEM, and by subsequent profiling of both deuterium depth deposition and nano-indentation hardness profile. In the current work, it was shown that the sample exposed at PSI-2, at 520 K and deuterium flux of 10^{22} $m^{-2}s^{-1}$, still demonstrate strong sub-surface plastic deformation. Should the deuterium flux be reduced further, this plastic deformation process might be

suppressed. Hence, repeating such an experiment at PlaQ at 450-600 K in single crystal and heavily deformed samples is important in order to reconcile the flux effects.

2. A second requirement is to clarify the impact of varying exposure temperatures. In this study, the plasma exposures were performed below 600°C to ensure that the plastically-induced microstructure would remain stable under the plasma exposure. In fact, most of the exposures were performed in a range of the ductile-to-brittle transition temperature of tungsten, where the dislocation mobility is rather low unless the internal stress is very high. Above a certain temperature, the dynamic recovery and annihilation of the dislocations is expected thus simultaneously removing the plasma-induced damage. Establishment of the threshold temperature for this recovery process is of high importance to confirm both the conclusions made here and our interpretation of the observed phenomena. As a guideline, it is proposed that investigation should be carried out of samples exposed to high flux deuterium plasma at 600°C and 800°C, a range where tungsten is known to be fully ductile.

3. The third requirement is to understand the impact of fluence. It is normal to expect that the microstructure should achieve a certain steady-state. Hence, performing high fluence (non-interruptive) exposure would clarify whether current observations are close to the steady-state condition, or if they differ strongly from it. One possible way of addressing this point is to use the Magnum PSI facility.

4. Besides studying exposure parameters, it is important to perform TEM and complementary analysis as described in our study to clarify the impact of Helium seeding. Helium seeding is known to have a strong impact on deuterium trapping. Given that this thesis discusses possible interrelation between plasma induced damage and deuterium retention, it would be of great interest to examine the microstructure of the same sample exposed to pure Helium and to mixed Helium-Deuterium plasma.

5. Finally, we would like to draw attention to a possible problem/artifact of the sequential exposures performed at Pilot-PSI device to achieve considerable fluences, as studied here. Earlier, it has been noted that the samples pre-exposed and annealed after TDS (up to about 1300 K) demonstrated somewhat different deuterium uptake when compared with non-exposed reference samples. This was attributed to the non-complete recovery of the voids which stored deuterium after the exposure [79]. To clarify this point, it is necessary to perform equivalent fluence exposures using interruptive and non-interruptive shots. Clarification of this question is very important for complete understanding and interpretation of the results obtained on plasma accelerators operating in pulse mode, like e.g. PILOT-PSI.

References.

1. *World energy supply and demand: The forecast with highest credibility by the US DOE/EIA.* Energy Exploration & Exploitation, 1997. **15**(3): p. 255-260.
2. B. Gilland, *World-Population, Economic-Growth, and Energy Demand, 1990-2100 - a Review of Projections.* Population and Development Review, 1995. **21**(3): p. 507-&.
3. M. Grenon, *Forecasting World-Energy Demand.* Power Engineering, 1977. **81**(6): p. 46-47.
4. E. Guk, N. Kalkan, *The importance of nuclear energy for the expansion of world's energy demand.* Advances in Energy Research, 2015. **3**(2): p. 71-80.
5. M. Silvestri, *World-Energy Demand, Environment, Role of Nuclear-Energy.* Aei Automazione Energia Informazione, 1993. **80**(3): p. 294-298.
6. D. Maisonnier, I. Cook, S. Pierre, et al., *DEMO and fusion power plant conceptual studies in Europe.* Fusion Engineering and Design, 2006. **81**(8-14): p. 1123-1130.
7. P. Helander, C. D. Beidler, T. M. Bird, et al., *Stellarator and tokamak plasmas: a comparison.* Plasma Physics and Controlled Fusion, 2012. **54**(12).
8. F. Romanelli and JET EFDA Contributors, *Overview of the JET results with the ITER-like wall.* Nuclear Fusion, 2013. **53**(10).
9. R.C. Wolf, A. Ali, A. Alonso, *Major results from the first plasma campaign of the Wendelstein 7-X stellarator.* Nuclear Fusion, 2017. **57**(10).
10. H. Bolt, V. Barabash, G. Federici, et al., *Plasma facing and high heat flux materials - needs for ITER and beyond.* Journal of Nuclear Materials, 2002. **307**: p. 43-52.
11. S. Matsuda, K. Tobita, *Evolution of the ITER program and prospect for the next-step fusion DEMO reactors: status of the fusion energy R&D as ultimate source of energy.* Journal of NUCLEAR SCIENCE and TECHNOLOGY, 2013. **50**(4): p. 321-345.
12. F. Romanelli, I. Abel, V. Afanesyev, et al., *Overview of the JET results with the ITER-like wall.* Nuclear Fusion, 2013. **53**(10).
13. C. Bachmann, G. Aiello, R. Albanese, et al., *Initial DEMO tokamak design configuration studies.* Fusion Engineering and Design, 2015. **98-99**: p. 1423-1426.
14. D. Maisonnier, *Plant models for DEMO.* Burning Plasma Diagnostics, 2008. **988**: p. 52-59.
15. S. J. Zinkle, J. T. Busby, *Structural materials for fission & fusion energy.* Materials today, 2009. **12**(11): p. 12-19.
16. N. Baluc, M. Q. Tran, *Chapter 13: Materials for ITER and fusion power reactors.* IAEA Publications, 2011. **50th IAEA Conference anniversary book**.
17. T. Hirai, S. Panayotis, V. Barabash, et al., *Use of tungsten material for the ITER divertor.* Nuclear Materials and Energy, 2016. **000**: p. 1-7.
18. G S Was, *Fundamentals of Radiation Materials Science*2007, New York: Springer.
19. D. Stork, P. Agostini, J. L. Boutard, et al., *Developing structural, high-heat flux and plasma facing materials for a near-term DEMO fusion power plant: The EU assessment.* Journal of Nuclear Materials, 2014. **455**(1-3): p. 277-291.
20. DJ Bacon, F Gao, YN Osetsky, *The primary damage state in fcc, bcc and hcp metals as seen in molecular dynamics simulations.* Journal of Nuclear Materials, 2000. **276**: p. 1-12.
21. R Stoller, GR Odette, BD Wirth, *Primary damage formation in bcc iron.* Journal of Nuclear Materials, 1997. **251**: p. 46-60.
22. DS Gelles, *Void swelling in binary Fe-Cr alloys at 200 dpa.* Journal of Nuclear Materials, 1995. **225**: p. 163-174.
23. Y Miwa, E Wakai, K Shiba, et al., *Swellinlg of F82H irradiated at 673 K up to 51 dpa in HFIR.* Journal of Nuclear Materials, 2000. **283-287**: p. 334-338.
24. G. Federici, W. Biel, M. R. Gilbert, et al., *European DEMO design strategy and consequences for materials.* Nuclear Fusion, 2017. **57**(9).

25. MW Guinan, JH Kinney, *Molecular dynamic calculations of energetic displacement cascades.* Journal of Nuclear Materials, 1981. **103-104**: p. 1319-1324.
26. JO Schiffgens, RD Bourquin, *Computer simulations of low energy displacement cascades in a face centered cubic lattice.* Journal of Nuclear Materials, 1978. **69-70**: p. 790-796.
27. A. E. Sand, K. Nordlund, S. L. Dudarev, *Radiation damage production in massive cascades initiated by fusion neutrons in tungsten.* Journal of Nuclear Materials, 2014. **455**(1-3): p. 207-211.
28. W. Setyawan, G. Nandipati, K. J. Roche, et al., *Displacement cascades and defects annealing in tungsten, Part I: Defect database from molecular dynamics simulations.* Journal of Nuclear Materials, 2015. **462**: p. 329-337.
29. DJ Bacon, YN Osetsky, R Stoller, et al., *MD description of damage production in displacement cascades in copper and α-iron.* Journal of Nuclear Materials, 2003. **323**: p. 152-162.
30. AV Barashev, SI Golubov, *Unlimited damage accumulation in metallic materials under cascade-damage conditions.* Materials science and technology division, 2008.
31. T. Tanno, M. Fukuda, S. Nogami, et al., *Microstructure Development in Neutron Irradiated Tungsten Alloys.* Materials Transactions, 2011. **52**(7): p. 1447-1451.
32. A. Hasegawa, T. Tanno, S. Nogami, et al., *Property change mechanism in tungsten under neutron irradiation in various reactors.* Journal of Nuclear Materials, 2011. **417**(1-3): p. 491-494.
33. A. Hasegawa, M. Fukuda, S. Nogami, et al., *Neutron irradiation effects on tungsten materials.* Fusion Engineering and Design, 2014. **89**(7-8): p. 1568-1572.
34. M. Fukuda, A. Hasegawa, S. Nogami, et al., *Microstructure development of dispersion-strengthened tungsten due to neutron irradiation.* Journal of Nuclear Materials, 2014. **449**(1-3): p. 213-218.
35. W. Van Renterghem, I Uytdenhouwen, Th. Loewenhoff, et al., *TEM analysis of recrystallized double forged tungsten after exposure in JUDITH 1 and JUDITH 2.* Nuclear Materials and Energy 2016. **accepted for publication**.
36. X. X. Hu, T. Koyanagi, M. Fukuda, et al., *Irradiation hardening of pure tungsten exposed to neutron irradiation.* Journal of Nuclear Materials, 2016. **480**: p. 235-243.
37. J. Matolich, H. Nahm, J. Moteff, *Swelling in neutron irradiated tungsten and tungsten-25 rhenium.* Scripta Metallurgica, 1974. **8**: p. 837-842.
38. N. Castin, A. Bakaev, G. Bonny, et al., *On the onset of void swelling in pure tungsten under neutron irradiation: An object kinetic Monte Carlo approach.* Journal of Nuclear Materials, 2017. **493**: p. 280-293.
39. M. Fukuda, K. Yabuuchi, S. Nogami, et al., *Microstructural development of tungsten and tungsten-rhenium alloys due to neutron irradiation in HFIR.* Journal of Nuclear Materials, 2014. **455**(1-3): p. 460-463.
40. D. Nguyen-Manh, M. Muzyk, K.J. Kurzydlowski, et al., *First-principles modelling of tungsten-based alloys for fusion power plant applications.* Key Engineering Materials, 2011. **465**: p. 15-20.
41. A. Hasegawa, M. Fukuda, K. Yabuuchi, et al., *Neutron irradiation effects on the microstructural development of tungsten and tungsten alloys.* Journal of Nuclear Materials, 2016. **471**: p. 175-183.
42. I. V. Gorynin, V. A. Ignatov, V. V. Rybin, et al., *Effects of Neutron-Irradiation on Properties of Refractory-Metals.* Journal of Nuclear Materials, 1992. **191**: p. 421-425.
43. G. Pintsuk, *Tungsten as plasma facing material.* Comprehensive Nuclear Materials, 2012. **4**: p. 551-581.
44. V. K. Alimov, B. Tyburska-Puschel, Y. Hatano, et al., *The effect of displacement damage on deuterium retention in ITER-grade tungsten exposed to low-energy, high-flux pure and helium-seeded deuterium plasmas.* Journal of Nuclear Materials, 2012. **420**(1-3): p. 370-373.

45. W. M. Shu, A. Kawasuso, Y. Miwa, et al., *Microstructure dependence of deuterium retention and blistering in the near-surface region of tungsten exposed to high flux deuterium plasmas of 38 eV at 315K.* Physica Scripta, 2007. **T128**: p. 96-99.
46. S. Lindig, M. Balden, V. K. Alimov, et al., *Sub-surface structures of ITER-grade W (Japan) and re-crystallized W after ITER-similar low-energy and high-flux D plasma loadings.* Physica Scripta, 2011. **T145**.
47. W. Xiao, W.T. Geng, *Role of grain boundary and dislocation loop in H blistering in W: A density functional theory assessment.* Journal of Nuclear Materials, 2012. **430**: p. 132-136.
48. M. Y. Li, J. H. You, *Mechanics of tungsten blistering II: Analytical treatment and fracture mechanical assessment.* Journal of Nuclear Materials, 2015. **465**: p. 702-709.
49. Y. Zayachuk, A. Manhard, M. H. J. 't Hoen, et al., *The effect of ion flux on plasma-induced modification and deuterium retention in tungsten and tungsten-tantalum alloys.* Journal of Nuclear Materials, 2015. **464**: p. 69-72.
50. V. K. Alimov, J. Roth, M. Mayer, *Depth distribution of deuterium in single- and polycrystalline tungsten up to depths of several micrometers.* Journal of Nuclear Materials, 2005. **337**(1-3): p. 619-623.
51. O.V. Ogorodnikova, J. Roth, M. Mayer, *Ion-driven deuterium retention in tungsten.* Journal of Applied Physics, 2008. **103**: p. 034902.
52. O.V. Ogorodnikova, J. Roth, M. Mayer, *Pre-implantation and pre-annealing effects on deuterium retention in tungsten.* Journal of Nuclear Materials, 2008. **373**: p. 254-258.
53. A. Manhard, K. Schmid, M. Balden, et al., *Influence of the microstructure on the deuterium retention in tungsten.* Journal of Nuclear Materials, 2011. **415**(1): p. S632-S635.
54. E. Lassner, W.-D. Schubert, *Tungsten. Properties, Chemistry, Technology of the Element, Alloys, and Chemical Compounds*1999, Vienna.
55. J. Stephens, *Dislocation Structures in Single-Crystal Tungsten and Tungsten Alloys.* Metallurgical Transactions, 1970. **1**: p. 1293.
56. C. Y. Chiem, W. S. Lee, *The Influence of Dynamic Shear Loading on Plastic-Deformation and Microstructure of Tungsten Single-Crystals.* Materials Science and Engineering a-Structural Materials Properties Microstructure and Processing, 1994. **187**(1): p. 43-50.
57. T. Tabata, H. Mori, H. Fujita, *In-situ deformation of tungsten single crystals with [100] tensile axis in an ultra-high voltage electron microscope.* Journal of the Physical Society of Japan, 1976. **40**: p. 1103.
58. J. W. Wang, Z. Zeng, C. R. Weinberger, et al., *In situ atomic-scale observation of twinning-dominated deformation in nanoscale body-centred cubic tungsten.* Nature Materials, 2015. **14**(6): p. 594-600.
59. J Fembock, R Stickler, A Vinckier, *The effect of strain rate and heating rate on the tensile behavior of W and W-ThO2 between room temperature and 1400C.* Proc. 11th Plansee seminar, 1985. **1**: p. 361 (Reutte, Tirol).
60. D Hull, D J Bacon, *Introduction to dislocations*2001, Oxford: Butterworth-Heinemann.
61. A. Pineau, A. A. Benzerga, T. Pardoen, *Failure of metals I: Brittle and ductile fracture.* Acta Materialia, 2016. **107**: p. 424-483.
62. D. Shindo, T. Oikawa, *Analytical Electron Microscopy for Materials Science*2002, Tokyo: Springer-Verlag.
63. David B. Williams, C. Barry Carter, *Transmission Electron Microscopy: A Textbook for Materials Science*2009: Springer.
64. T. W. Butler, *On the determination of dislocation densities*1969, Annapolis.
65. Peter J. Goodhew, John Humphreys, Richard Beanland, *Electron Microscopy and Analysis.* 2000: CRC Press.
66. Adam J. Schwartz, Mukul Kumar, Brent L. Adams, et al., *Electron Backscatter Diffraction in Materials Science.* 2013: Springer Science & Business Media.
67. M. Mayer, SimNRA User Guide, Report IPP 9/113, Max-Planck-Institut für Plasmaphysik, 1997. **Garching, Germany,**.

68. K. Schmid, U. von Toussaint, Nuclear Instruments & Methods in Physics Research B, 2012. **281**: p. 64-71.
69. W. Oliver, G. Pharr, Journal of Materials Research, 2004. **19**: p. 3-20.
70. H. Mecking, U. F. Kocks, *Kinetics of Flow and Strain-Hardening.* Acta Metallurgica, 1981. **29**(11): p. 1865-1875.
71. I. J. Beyerlein, C. N. Tome, *A dislocation-based constitutive law for pure Zr including temperature effects.* International Journal of Plasticity, 2008. **24**(5): p. 867-895.
72. D. Terentyev, X. Z. Xiao, A. Dubinko, et al., *Dislocation-mediated strain hardening in tungsten: Thermo-mechanical plasticity theory and experimental validation.* Journal of the Mechanics and Physics of Solids, 2015. **85**: p. 1-15.
73. L. Buzi, *Influence of the Particle Flux on Surface Modifications of Tungsten.* PhD thesis, 2015. **ISBN 978-90-8578-843-0**: p. Ghent University.
74. L. Buzi, G. De Temmerman, B. Unterberg, et al., *Influence of tungsten microstructure and ion flux on deuterium plasma-induced surface modifications and deuterium retention.* Journal of Nuclear Materials, 2015. **463**: p. 320-324.
75. J.B. Condon, T. Schober, *Hydrogen bubbles in metals.* Journal of Nuclear Materials, 1993. **207**: p. 1-24.
76. P. Grigorev, D. Terentyev, V. Dubinko, et al., *Nucleation and growth of hydrogen bubbles on dislocations in tungsten under high flux low energy plasma exposure.* Nuclear Instruments & Methods in Physics Research Section B-Beam Interactions with Materials and Atoms, 2015. **352**: p. 96-99.
77. T. Tanabe, *Review of hydrogen retention in tungsten.* Physica Scripta, 2014. **T159**: p. 014044.
78. Y. Zayachuk, A. Manhard, M. H. J. t'Hoen, et al., *Depth profiling of the modification induced by high-flux deuterium plasma in tungsten and tungsten-tantalum alloys.* Nuclear Fusion, 2014. **54**(12): p. 123013.
79. Y. Zayachuk, M. H. J. 't Hoen, P. A. Z. van Emmichoven, et al., *Surface modification of tungsten and tungsten-tantalum alloys exposed to high-flux deuterium plasma and its impact on deuterium retention.* Nuclear Fusion, 2013. **53**(1): p. 013013.
80. M.H.J. 't Hoen, B. Tyburska-Pûschel, K. Ertl, et al., *Saturation of deuterium retention in self-damaged tungsten exposed to high-flux plasmas.* Nuclear Fusion, 2012. **52**: p. 023008.
81. K. Schmid, V. Rieger, A. Manhard, *Comparison of hydrogen retention in W and W/Ta alloys.* Journal of Nuclear Materials, 2012. **426**: p. 247-253.
82. M. Mayer, E. Gauthier, K. Sugiyama, et al., *Quantitative depth profiling of deuterium up to very large depths.* Nuclear Instruments & Methods in Physics Research Section B-Beam Interactions with Materials and Atoms, 2009. **267**(3): p. 506-512.
83. D. E. J. Armstrong, P. D. Edmondson, S. G. Roberts, *Effects of sequential tungsten and helium ion implantation on nano-indentation hardness of tungsten.* Applied Physics Letters, 2013. **102**(25).
84. Z.X. Zhang, D.S. Chen, W.T. Han, et al., *Irradiation hardening in pure tungsten beforeand after recrystallization.* Fusion Engineering and Design, 2015. **98-99**: p. 2103-2107.
85. V. Dubinko, P Grigorev, A. Bakaev, et al., *Dislocation mechanism of deuterium retention in tungsten under plasma implantation.* Journal of Physics: Condensed Matter, 2014. **26**: p. 395001.
86. Luxherta Buzi, Greg De Temmerman, Bernhard Unterberg, et al., *Influence of particle flux density and temperature on surface modifications of tungsten and deuterium retention.* Journal of Nuclear Materials, 2014. **455**(1–3): p. 316-319.
87. W. Z. Yao, P. Wang, A. Manhard, et al., *Effect of hydrogen on the slip resistance of tungsten single crystals.* Materials Science and Engineering a-Structural Materials Properties Microstructure and Processing, 2013. **559**: p. 467-473.
88. P. Grigorev, L. Buzi, A. Bakaeva, et al., *Numerical analysis of TDS spectra under high and low flux plasma exposure conditions* Phys. Scripta, 2016. **T167**: p. 014039.